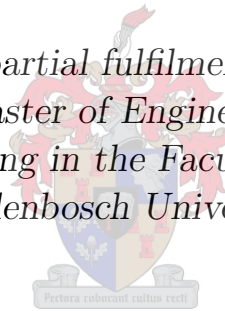


# Wideband Axially Symmetric Power Combiners Based on Short Step Filters

by

Hein Xavier Swart

*Thesis presented in partial fulfilment of the requirements  
for the degree of Master of Engineering in Electric and  
Electronic Engineering in the Faculty of Engineering at  
Stellenbosch University*



Department of Electric and Electronic Engineering,  
University of Stellenbosch,  
Private Bag X1, Matieland 7602, South Africa.

Supervisor: Prof D.I.L. De Villiers

March 2021

# Declaration

By submitting this thesis electronically, I declare that the entirety of the work contained therein is my own, original work, that I am the sole author thereof (save to the extent explicitly otherwise stated), that reproduction and publication thereof by Stellenbosch University will not infringe any third party rights and that I have not previously in its entirety or in part submitted it for obtaining any qualification.

Date: .....

Copyright © 2021 Stellenbosch University  
All rights reserved.

# Abstract

This thesis presents a technique for the design of compact  $N$ -way coaxial line power combiners. By incorporating short-step-stub Chebyshev impedance transformers into the design, a noteworthy reduction in the physical size, compared to existing axially symmetric combiners, is achieved. This feature is especially advantageous at lower microwave frequencies for which combining structures are typically large.

An 8-way coaxial combiner at  $L$ -band, with a 10th order short-step-stub Chebyshev impedance transformer is designed and simulated. The simulation results show a  $-12$  dB return loss bandwidth of 112%. The total size of the structure is  $0.22\lambda$  at the lowest pass-band frequency. Due to the optimisation framework used, very few full wave calculations are required which makes the design simple and relatively fast to execute.

Network analysis techniques are investigated and the different circuit parameter descriptions for lossless circuits are presented. This forms the foundation for the realisability conditions of short-step filters in terms of circuit parameters. A detailed examination on the theory of network synthesis is done. Short-step impedance transformers are analysed and synthesized and accompanied by complete design examples, demonstrating the procedure for extracting element values from the synthesised transfer functions. The short-step impedance transformers are designed and synthesised with specified operating bandwidths and transmission line lengths well suited for the purposes of waveguide power combiners at lower microwave frequencies.

A general configuration for coaxial combiner designs and geometrical parameter descriptions are presented. Special considerations for combiners with short-step-stub impedance transformers are discussed and the methods for implementing different parts of the design is analysed. A back-short is included in the synthesis that allows a short-step transformer to be incorporated into coaxial combiners. A method for realising shunt stub lines within the combiner configuration is demonstrated. A space-mapping optimisation framework is used to extract mathematical models describing the relationship between physical parameters and circuit element values for optimising the design.

# Opsomming

Hierdie verslag lewer 'n ontwerptegniek vir kompakte,  $N$ -rigting, koaksialelyn drywings kombineerders. Met ingeboude kort-stap-stomplyn Chebyshev impedansie transformators is die ontwerp se fisiese grootte noemenswaardig kleiner as bestaande soortgelyke kombineerders. Hierdie eienskap is veral voordelig by laer mikrogolf frekwensies, wat tipies groot kombineerings strukture vereis.

Die ontwerp en simulatie resultate van 'n 8-rigting koaksiale kombineerder by  $L$ -band, met 'n 10de orde Chebyshev impedansie transformeerder word voorgelê. Die simulatie resultaat vertoon 'n  $-12$  dB weerkaatskoeffisiënt bandwydte van 112%. Die totale lengte van die kombineerder is  $0.22\lambda$  by die laagste frekwensie van die deurlaat band. Met die optimerings raamwerk wat gebruik is, word baie min volgolf berekeninge benodig wat die ontwerp eenvoudig en relatief vinnig maak om uit te voer.

Kort-stap impedansie transformeerders word gesintetiseer om spesifieke bandwydtes en transmissielyn lengtes te vertoon. Die teorie van netwerk sintese word sorgvuldig ondersoek. Die tegnieke vir netwerk analiese met verskillende parametriesse stroombaan beskrywings word voor gelê. Die realiseerbaarheidsvereistes word weergegee in terme van die stroombaan beskrywings wat belangrik is in die ontwerp van kort-stap transformeerders. Die ontwerpproses vir kort-stap transformeerders word deeglik ondersoek waarna 'n paar verskillende voorbeelde gesintetiseer word tydens 'n volledige ontwerpvoorbeeld wat ook die stroombaanelement waardes onttrek.

Die algemene konfigurasie vir 'n koaksiale kombineerder met die geometriese beskrywing daarvan word gegee. Aanvangs vereistes vir die ontwerp word bespreek en die metodes waar volgens verskillende dele van die ontwerp geïmplementeer word, word geanaliseer. Die sintese word aangepas om 'n kortgesluite transmissielyn in te sluit en stomplyn word gerealiseer met geëtste stroombane op diëlektriese skywe wat versoenbaar is met die kombineerder se konfigurasie. Modelle wat die wiskundige verhouding beskryf tussen fisiese veranderlikes en stroombaanelemente word onttrek met 'n optimeeringsraamwerk wat ook gebruik word vir die optimering van die volledige ontwerp.

# Acknowledgements

I wish to express my sincere gratitude to the following individuals:

- Prof. Dirk De Villiers my supervisor, for his guidance and support, and for the opportunity to work on this project.
- Dr. Ryno Beyers, for the valuable insights and advice he provided.
- Prof. Pieter W. van der Walt, for the time spent helping me understand his work that forms the basis of this project.
- My brother Wayne, for the time and effort spent proof reading this document.
- My wife Hanlie, for all her love and support, without which I would be far from complete.

# Contents

Declaration	i
Abstract	ii
Opsomming	iii
Acknowledgements	iv
Contents	v
List of Figures	vi
List of Tables	x
<b>1 Introduction</b>	<b>1</b>
1.1 Background on Power Combiners . . . . .	2
1.2 About the Thesis . . . . .	4
1.3 Layout of the Thesis . . . . .	4
<b>2 Synthesis</b>	<b>5</b>
2.1 Analysis . . . . .	6
2.2 Realizability Conditions . . . . .	13
2.3 The Short-Step-Stub Chebyshev Impedance Transformer . . . . .	24
2.4 Conclusion . . . . .	38
<b>3 Compact N-Way Coaxial Waveguide Combiners</b>	<b>39</b>
3.1 General Parameters of a Coaxial Combiner . . . . .	40
3.2 Design Considerations with Waveguide Implementations . . . . .	43
3.3 Coaxial Combiner with an Integrated Short-Step Impedance Transformer . . . . .	51
3.4 Design Example . . . . .	64
3.5 Higher Order Example Designs . . . . .	85
<b>4 Conclusion</b>	<b>94</b>
<b>Bibliography</b>	<b>96</b>

# List of Figures

2.1	Circuit diagram of an arbitrary ladder network. . . . .	6
2.2	Diagram of nodes and branches from the circuit enclosed within the rectangle in Fig. 2.1 . . . . .	7
2.3	The different configurations used to find the ABCD Parameters for a two-port network. a) A voltage source at port one with port two open circuit. b) A voltage source at port one with a short circuit at port two. c) A current source at port one with an open circuit at port two. d) A current source at port one with port two short-circuited. . . . .	10
2.4	Doubly terminated two-port network illustrating the parameter for defining S-parameters. . . . .	11
2.5	Equivalent circuits for $Z(s) = \frac{8s+2s^3}{1+s^2}$ using Cauey I, II and Foster I, II realizations	19
2.6	Zero shifting by partial removal of a pole at infinity for an $LC$ immittance function. Only the positive half of the imaginary axis is shown. As $k$ increases, the zeros of the pole being removed, shifts. When the the pole is removed completely, the zero shifts to infinity. . . . .	20
2.7	$Z_{LC}$ with a resonant branch at $s \pm j3$ . . . . .	21
2.8	Loss poles are obtained through (a) a series antiresonance branch or (b) a shunt resonance branch. . . . .	22
2.9	Equivalent circuit realizations of a resonance branch at $s^2 = -9$ (a) Realization of a resonant branch at $s \pm j3$ using a Brune section. (b) $Z_{LC}$ equivalent circuit realization with a Brune section identical to an ideal transformer. . . . .	23
2.10	Typical transformer layouts for a 4-th order short-step and a order 2 quarter-wave transformer demonstrating the significant reduction in transmission line length for the short-step transformer of order $2N$ compared to a classical quarter-wave transformer of order $N$ . . . . .	25
2.11	Transmission zeros of $H(p)H(-p)$ . The Transmission zeros for $H(p)$ are located in the LHP. . . . .	32
2.12	Kuroda identity displaying equivalent circuits of a unit element with a parallel, open-circuit stub and a unit element with a series, short-circuited stub. . . . .	33
2.13	$ S_{11} $ Response of the short-step stub Chebyshev impedance transformer. . . . .	35
2.14	Microwave Office coaxial line implementation of the short step transformer with $\frac{\lambda}{12}$ lines. . . . .	35
2.15	Passband performance comparison between N-th order quarter-wave, Chebyshev impedance transformer vs $2N$ -th order short-step Chebyshev transformers. . . . .	37
3.1	Simplified transmission line model of a reactive N-way combiner. . . . .	40
3.2	Coaxial line geometry. . . . .	40
3.3	2D cross-section of an 8-way coaxial combiner with its parameters. . . . .	41

3.4	<i>xy</i> -Plane cross-section of the 8 periheral ports, 2 - N+1, arranged symmetrically around the axis of the central port of an 8-way combiner. . . . .	41
3.5	A basic congiguration of the short-step transformer circuit with a back-short. The circuit is simulated in AWR MWO with coaxial transmission line elements. The element extractions are performed using the dual circuit parameters. . . . .	44
3.6	N-th order Chebyshev short-step impedance transformer comparison between analytical synthesis without a back-short and numerically approximated synthesis that include a back-short. . . . .	45
3.7	Normalized cut-off frequency of the dominant $TE_{11}$ waveguide mode for a coaxial line. . . . .	47
3.8	Configuration of shunt stub-line implementation within a coaxial waveguide using microstrip lines etched on a PCB substrate. . . . .	52
3.9	X-plane bisection views of the a dielectric disc at a step discontinuity in the oversized coaxial inner conductor. a) Displays the face of the disc with the negative etched line sections (spokes), where b) shows the opposite face of the disc with the positive spokes. The spokes overlap in the radial direction to form a quasi-TEM transmission line. . . . .	53
3.10	Coaxial line parameters when flattened out into a micro strip line configuration. . . . .	53
3.11	Disc placement at the step-discontinuity within a combiner and the circuit model representation thereof. . . . .	55
3.12	Dielectric disc configuration with overlapping ring conductors used to accommodate the peripheral port connections as well as providing the shunt line from the synthesised filter. . . . .	56
3.13	A three-dimensional view of the a dielectric disc at the peripheral input ports. a) Displays the face of the disc with the negative etched annular ring, where b) shows the opposite face of the disc with the positive etched ring, making contact with the oversized coaxial inner conductor and also the centre conductors of the peripheral input ports. The positive and negative rings overlap in the radial direction. This serves to approximate the synthesised shunt element, whilst also reducing the inductance of the input port central conductors. . . . .	57
3.14	Circuit model representation of section D-C of Fig. 3.3. . . . .	57
3.15	Tapered line section B-A of Fig. 3.3. . . . .	59
3.16	3D view of a central port taper implementation. . . . .	59
3.17	Flow diagram of a space-mapping optimisation routine. . . . .	62
3.18	The synthesised circuit of the 6-th order short-step stub filter. The circuit element numbering is demonstrated and show the addition of element $Z_0$ for practical construction. a) Displays the circuit with open circuit shunt stub lines as synthesised and b) shows the same circuit with the shunt elements replaced with equivalent $LC$ branches. This is useful for approximating an etched disc implementation of the shunt stub lines. . . . .	67
3.19	The process for approximating equivalent $LC$ branches for the different stub-lines is shown. The circuit from Fig. 3.18a is separated into individual circuit for each stub-line with its adjacent transmission line sections, demonstrated in a). Each stub-line is approximated as an $LC$ branch as in b). The complexed valued response of the stub-line and approximate $LC$ branch is shown in c) before fine tuning and in d) after fine tuning the $LC$ values. . . . .	68
3.20	$S_{11}$ response of the synthesised filter circuit from Fig. 3.18a. . . . .	69
3.21	Dielectric disc 1, with its adjacent coaxial line sections $Z_0 = 50\ \Omega$ and $Z_2 = 83\ \Omega$ . The disc is used to approximate $Z_1$ as seen in Fig. 3.19a and 3.19b. . . . .	71



3.22	The alignment step for a single $x$ and $y$ parameter value combination. a) Display the imaginary and real parts of the $S_{11}$ responses for the coarse and fine model before alignment. b) The vector difference between the response in a). The $L_1$ norm = 42.1664 and the $L_2$ norm = 4.4526, which is the combined normalised error. In c) the responses are barely distinguishable from each other after alignment. In d) it should be noted that the scale of the vector difference between the model response has been reduced significantly. After alignment the improved error values are $L_1$ norm = 0.012893, and the final error using norm $L_2 = 0.0014903$ demonstrates the accuracy of the alignment process. . . . .	73
3.23	A surface fit used to demonstrate how a mathematical function may be used to extract a model for relating peripheral disc parameters to circuit element values. Impedance of a stub-line in this case. . . . .	74
3.24	Dielectric disc 3 with $Z_6$ , the back-short joining to its left and $Z_4$ to its right and SMA connectors on its periphery. The disc at the peripheral has a different configuration to the other discs implemented. Because of this it is often advantages to use an alternative coarse model that is better suited to mathematical curve fitting. . . . .	75
3.25	The combiner structure form by cascading the individual sections. . . . .	76
3.26	A demonstration of a tapered line transition between a coaxial line section and a N-type connector. The figure is not drawn to scale, for the purpose of demonstration. . . . .	77
3.27	The same combiner structure of Fig. 3.25 with a tapered line section to fit an N-type connector. The structure is simulated in CST and optimised using space-mapping. . . . .	78
3.28	The $S_{11}$ complex valued responses and vector differences for the complete combiner structure fine model (black) and the coarse model (red). Plots a) and b) are plotted before alignment. Plots c) and d) are plotted after alignment.	79
3.29	The $S_{11}$ responses from the different models in the space mapping optimisation routine. The optimised response in this example was found with two iterations.	81
3.30	The $S_{11}$ responses from the different models in the space mapping optimisation routine. . . . .	81
3.31	The optimised $S_{11}$ response of the circuit from the design example, with the disc and transmission line parameters offset with manufacturing tolerances. a) The effect of CNC machining tolerances. b) The effect of PCB etching process tolerances. . . . .	84
3.32	The $S_{11}$ response of a) a 6th order filter, b) a 8th order filter, c) a 10th order filter and d) a 12th order filter. . . . .	86
3.33	The different model responses at the a) 1st iteration and b) final iteration of the space-mapping optimisation. The optimised responses are for the 8th order combiner. . . . .	89
3.34	The $S_{11}$ response of the synthesised 8th order filter compared with the optimised response of the compact 8-way combiner incorporating the filter. The optimised fine model response displays $S_{11} \leq -20$ dB over a bandwidth of 76%.	90
3.35	The different model responses at the a) 1st iteration and b) final iteration of the space-mapping optimisation. The optimised responses are for the 10th order combiner. . . . .	91

- 3.36 The  $S_{11}$  response of the synthesised 10th order filter compared with the optimised response of the compact 8-way combiner incorporating the filter. The optimised fine model response displays a  $S_{11} \leq -17.5$  dB over an approximate bandwidth of 104%. The figure also shows the circuit response has a bandwidth of 112% for  $S_{11} \leq -12$  dB. . . . . 92

# List of Tables

2.1	Passband performance comparison of quarter-wave vs. short-step Chebyshev transformers. . . . .	36
3.1	Passband performance comparison of short-step synthesised filters, and filter synthesis with a numerical approximation for the inclusion of a back-short with a given transformer ratio. . . . .	46
3.2	A summary of the disc parameters and the elements values affected with changes in the given parameters. . . . .	54
3.3	The normalised and $50\ \Omega$ scaled element values extracted during the synthesis procedure of a 6-th order short-step stub Chebyshev Filter with an impedance transformer ratio of 8. . . . .	65
3.4	The $LC$ values approximation of each stub-line as numbered in Fig. 3.18b. The units of measure for capacitance is pF and nH for inductance. . . . .	69
3.5	The inner radii dimensions for coaxial line sections with the corresponding characteristic impedances. . . . .	70
3.6	The extracted polynomials approximating the relationship between the physical parameters of the fine model etched dielectric discs and the equivalent $LC$ element values of the circuit from Fig. 3.18b. . . . .	76
3.7	Calculated parameter values for the tapered line of Fig. 3.26. The dimensions are in millimetres and degrees where appropriate. . . . .	79
3.8	Parameters to be optimised simultaneously. The lower bound, starting value, upper bound and optimised value for each parameter is given. The range of values demonstrate the complexity of the optimisation problem at hand. . . .	80
3.9	Synthesised results for different orders of short-step filters. The element values shown are scaled to a $50\ \Omega$ central port impedance. . . . .	85
3.10	Calculated radii of the coaxial line segments for the different combiners with impedances from Table 3.9. . . . .	87
3.11	Lengths of the coaxial line segments and tapered line and also the total combiner length of the different combiners, after optimisation. . . . .	87
3.12	The optimised physical parameters of the dielectric discs with etched lines. . .	87
3.13	The extracted polynomials approximating the relationship between the physical parameters of the fine model etched dielectric discs and the element values of the 8th order filter. . . . .	88
3.14	The extracted polynomials approximating the relationship between the physical parameters of the fine model etched dielectric discs and the element values of the 10th order filter. . . . .	88
3.15	Comparison between the 10th Order simulated compact combiner and the combiner from [15]. . . . .	93

# Chapter 1

## Introduction

Axially symmetric power combiners generally allow for a large number of devices to be combined with lower losses compared to other power combiner types with the same number of input ports. Non-resonant axially symmetric combiners typically have the added advantage of being able to support transverse electromagnetic (TEM) modes, and can therefore offer high performance return losses at the output port over wide bandwidths when the input ports are excited symmetrically. For these types of combiners the output port is generally referred to as the central port and the input ports as peripheral ports. The design of such combiners is mostly focussed on obtaining a well-matched impedance transition between the peripheral ports, the oversized coaxial structure and the output port [1].

The short-step stub Chebyshev impedance transformer, discussed in this thesis, is effectively a bandpass filter and therefore will also be referred to as a short-step filter. In [2] it is shown how such an impedance transformer is capable of reducing the physical size of a circuit whilst maintaining comparable circuit performance. The main goal of this thesis is to incorporate a short-step filter into the design of a coaxial power combiner in order to reduce its size without compromising on performance.

## 1.1 Background on Power Combiners

### 1.1.1 Solid State Power Amplifiers and the use of Power Combiners

Microwave power combiners/dividers are frequently used in microwave systems such as communication and RADAR applications which require high power levels. These high power levels can be achieved in microwave and radio frequency (RF) systems by combining the outputs of a number of amplifiers with otherwise limited power capacity. Power combiners are used to overcome limitations of individual amplifiers by combining a system of multiple solid state power amplifiers (SSPA) in unison and they are vital in the competition between solid state power amplifiers and their counterparts; travelling wave tube amplifiers (TWTAs). Significant advances have been made in microwave power generation since the first SSPAs were combined to give a few watts of power. Single-package amplifiers with Gallium Nitride (GaN) high mobility electron transistors (HEMT) have been demonstrated to generate more than 80 W in the X-band [3] and more than 30 W in the Ku-band [4] with continuous wave (CW) operation. Literature has also reported GaN HEMT amplifiers with pulsed power outputs within the X-band with peak values exceeding 100 W [5, 6]. With small scale SSPA packages that contain numerous GaN HEMTs in combination, it is possible to realize very high power densities when appropriate combining techniques are used as seen in [7] where 2 kW was achieved under CW operation in the X-band. With the advancements in modern day technology SSPAs are becoming more competitive in their ability to compete with TWTAs and various other sources of microwave power.

Power combiners play an essential role in the performance of SSPA systems. The type and implementation of a combiner affect the efficiency and physical size of the system which includes the power generating capabilities because of the limitations imposed on the number of amplifiers that can be combined. The ability of a SSPA to maintain some functionality under adverse conditions, such as the failure of individual amplifiers, gives it the desirable robustness known as graceful degradation. This means that the SSPA will still generate usable output power even when individual amplifiers within the system fail. This is a sought after feature, especially in systems combining large numbers of amplifiers, as it reduces the probability of cataclysmic system failures. Graceful degradation is normally attributed to the power combiner and the isolation it offers between amplifiers.

Smaller area devices have significantly higher power-added-efficiency (PAE) than larger area devices [8]. Numerous SSPAs can be combined in small packages sized at about 20 mm<sup>2</sup>, which allow for high power densities as seen in [3–7], but is only effective for a limited number of devices [9]. On the other hand, power combiners are implemented with larger structures which help to increase even higher power densities and improved reliability. Power handling is not the only consideration when designing power combiners and where physical dimensions are of importance as with satellites for example, size becomes an issue, especially at lower microwave frequencies as the dimensions of combining structures is a function of wavelength. In general there are two forms of power combining methods. These are 2-way combiners, which utilise corporate or chained networks to combine more than two devices in a tree or series configuration respectively, or  $N$ -way combiners which allow  $N$  devices to be combined in a single step. Each method of implementation has its advantages and disadvantages. Corporate and chain networks have

the advantages of well established design procedures and are implemented using various transmission line mediums which make it well suited for a variety of cases with the added bonus of having well matched and isolated input ports.

The disadvantages of these types of combiners are however, that they become inefficient and physically large when combining a large number of devices [9, 10]. With higher numbers of combining ports ( $N > 8$ ) the benefits of  $N$ -way axially symmetric combiners compared to corporate- and chain networks are quite significant in terms of the physical size reductions and amplitude and phase balance due to the symmetrical structures, which in turn leads to increased combining efficiency. The overall loss of corporate tree combiners scales with  $N$  where the loss of  $N$ -way symmetrical combiners scale with the value  $\log(N)$ .

### 1.1.2 Axially Symmetric Power Combiners

In general an axially symmetric power combiner is constructed with the input ports equally spaced and symmetrically around the axis of an output port. Two of the more common configurations that have been used is with the input ports facing either in a direction parallel to the axis of the output port or in a direction perpendicular to the axis of the output port. Different symmetrical transmission line types, such as radial, conical or coaxial transmission lines allow for the above configurations to be implemented and serve as the conductor between the input and output ports.

Radial line power combiners with designs based on electromagnetic field analysis and full-wave simulations have been implemented successfully [11, 12], but a major drawback in these designs is the fact that the fundamental TEM mode supported by the radial transmission line has a characteristic impedance that varies with radial distance. This means that the radial line has a complex input impedance when the line length is finite, which complicates the design and decreases performance. Conical and coaxial transmission lines also support the fundamental TEM mode, but unlike radial transmission lines they also have constant characteristic line impedance with radial distance. Typically conical lines outperforms coaxial transmission lines in terms of size, because coaxial lines have longer electrical path lengths when impedance matching tapered sections are required to accommodate input ports to coaxial line sections. With the  $\frac{\lambda}{16}$  short-step design from chapter 2, the goal is to significantly reduce the length requirements of the coaxial lines, thereby decreasing the size advantage that conical lines have over coaxial lines.

Some advantages of coaxial combiners are that they support TEM mode propagation which provide constant characteristic impedance with radial distance as already mentioned. Due to coaxial lines having real impedances as opposed to complex port impedance, simple transmission line theory applies which simplifies design procedures compared with conical and radial line designs.

Literature provides some notable coaxial power combiner designs which include a 4-way combiner with a reflection coefficient of better than  $-15$  dB and a bandwidth of 70% at a centre frequency of 11.5 GHz [13], a 16-way combiner with a reflection coefficient of better than  $-20$  dB with a bandwidth 20% at a centre frequency of 1.3 GHz [14], and an 8-way combiner with a reflection coefficient of better than  $-12$  dB over a bandwidth of 115% at a centre frequency of 1.2 GHz [15].

This thesis will focus on the design of a coaxial waveguide power combiner that implements a short-step Chebyshev impedance transformer in order to make the design as small as possible whilst retaining a comparable reflection coefficient and bandwidth. An eight-way combiner at a centre frequency of 1.2 GHz is designed with different orders of short-step filters implemented within the coaxial structure.

## 1.2 About the Thesis

A short-step-stub Chebyshev impedance transformer is synthesized and incorporated within the design of a coaxial microwave power combiner that allows a significant reduction in size with comparable performance to existing broadband waveguide power combiners. Three combiners are designed, achieving reflection coefficients of less than  $-21$  dB,  $-20$  dB and  $-17.5$  dB across, 58%, 76% and 104% bandwidths respectively. A coaxial combiner with an integrated 10th order short-step filter is demonstrated to be in excellent comparison to designs from literature, and displays simulated results showing 112% bandwidth, from 527 MHz to 1872 MHz, when measured at a return loss of less than  $-12$  dB. The total length of the combiner is  $0.22\lambda$  at the lowest frequency of operation compared to the design from literature which has a total length equal to  $0.75\lambda$  at the same frequency.

## 1.3 Layout of the Thesis

Chapter 2 provide a necessary discussion on the topic of network synthesis. As a prerequisite the fundamentals of network analysis are presented. Different sets of parameters for describing circuits are used for determining realisability conditions for terminated, two-port, passive reactive network. The theory is used to analyse the design and performance of a short-step impedance transformer which is concluded with a design example.

Chapter 3 starts with a review on the general coaxial combiner geometry and a typical configuration of the structure. Next some initial design factors that need consideration are investigated. Some complications with incorporating the synthesised circuits of Chapter 2 are highlighted and resolved with examples. The combiner layout is divided into individual section that simplify the discussion to clearly illustrate how each part of the combiner is designed, followed by a perusal of a space-mapping framework, used to optimise the design. The design considerations together with the section on the design of the individual parts of the combiner are tied together in a comprehensive design example. The chapter concludes with a summary of results for combiners with different short-step Chebyshev impedance transformers. A combiner design is compared to a combiner with similar performance from literature, from which the reduction in size is put into perspective.

The final chapter presents the conclusions to the results achieved in Chapter 2 and 3 of this thesis. Some recommendations are made on possible improvements and expansions to the presented designs.

# Chapter 2

## Synthesis

Synthesis of electronic circuits is a scientific and mathematically based design approach [16]. The intrinsic nature of the method is to obtain the circuit elements and component values of a circuit from a mathematical function designed to have a specified circuit response. This is contrary to classical network analysis, which applies various electric circuit theorems to calculate the response of a network.

The power combiners pertaining to the scope of this thesis will be limited to the category of passive, reactive circuits. As the main purpose of these power combiners is to match multiple input ports to the central combining output port and visa versa as to accomplish maximum energy transfer. Ideally the network should be lossless, with the total energy entering the circuit equal to the total energy leaving the circuit. It follows that an appropriate point of departure on this topic is the law of conservation of energy which states that energy cannot be created or destroyed — it can only be converted from one form to another [17]. In the study of electromagnetism this is referred to by Poynting's theorem [18]. In passive circuits this law states that energy leaving the circuit cannot exceed the energy supplied to the circuit and therefore must satisfy (2.1), where subscript  $i$  denotes the port number [16]. The nett energy,  $E(t)$  supplied to the circuit, i.e. the difference in energy entering the circuit and the energy leaving the circuit defined as

$$E(t) = \int_{-\infty}^t \sum_{i=1}^N [v_i(\tau)i_i(\tau)]d\tau \geq 0, \quad (2.1)$$

where  $N$  is the number of ports and  $v_i(\tau)$  and  $i_i(\tau)$  are the port voltage and current functions of time  $\tau$  and  $d\tau$  is the time differential in the integral. Stated differently, the combiner to be considered should ideally be a pure impedance transformer, with zero resistive elements and only reactive  $LC$  immittances<sup>1</sup> so that  $E(t) = 0$  or as close to zero as possible in order to accomplish maximum energy transfer. This chapter is dedicated to the design, approximation and realization i.e. the synthesis of such circuits. In order to achieve this goal it is necessary to provide the fundamental theory needed to understand the synthesis process. Classic circuit analysis techniques form the foundation of the theory and is discussed in section 2.1. The following section investigates the mathematical conditions required for a circuit to be practically realisable. Section 2.3 builds on the theory of the previous sections in a discussion on the importance of the short-step-stub Chebyshev impedance transformer. Section 2.4 presents the chapter conclusion

---

<sup>1</sup>The generic name *immittance* will be used to refer to either impedances or admittances



## 2.1 Analysis

A necessary prerequisite to circuit synthesis is an overview of analysis techniques and different sets of circuit parameter descriptions. These parameters may be measured at the ports of a circuit, and without knowledge of the circuitry between the ports, much information can be deduced about its workings. The first set of circuit parameters to look at are the impedance  $z$  and admittance  $y$  parameters. These allow for calculating port voltages or currents. The second parameter set of interest is the transmission, also known as chain or ABCD parameters. These are used in determining the performance of input and output voltages and currents of a transmission network and are convenient to use when cascading different networks. The last parameter set is the scattering parameters. S-parameters are used as a base to describe general network behaviour. During circuit synthesis a desired circuit response may be described in terms of S-parameters, which can then be converted into  $y$ ,  $z$  or transmission parameters. These parameters are then used for element extraction and converted into component values to realize a circuit. The discussion will be limited to linear, passive circuits.

Starting with the well-known Kirchoff laws which state that the sum of all voltages within a closed loop is equal to zero, known as Kirchoff's voltage law (KVL), and the sum of all currents flowing into a node in a circuit is equal to zero, known as Kirchoff's current law (KCL) a circuit analysis on Fig. 2.1 serves to illustrate, by means of an example, an organised approach to circuit analysis.

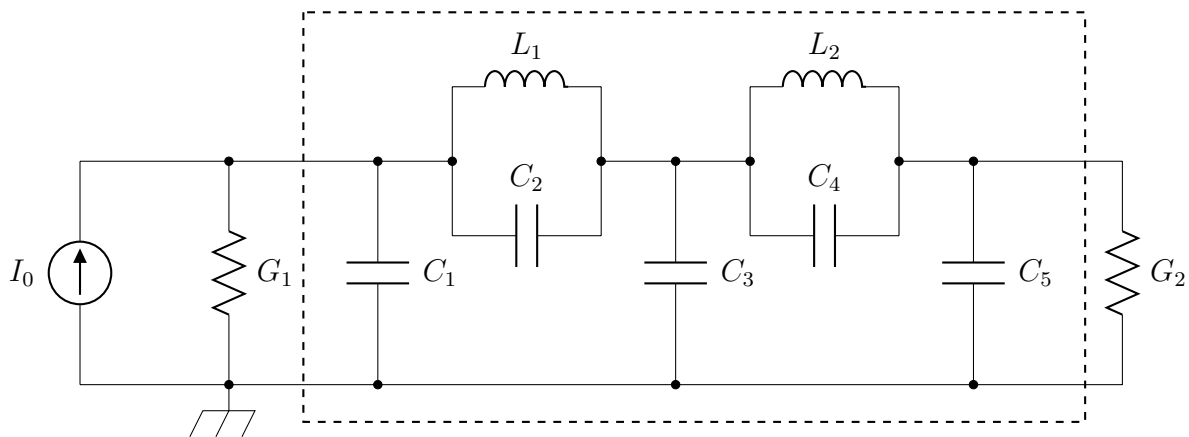


Figure 2.1: Circuit diagram of an arbitrary ladder network. The circuit inside the dashed rectangle serves to illustrate a node voltage analysis.

Fig. 2.2 is a node and branch representation of the circuit enclosed in the dashed rectangle in Fig. 2.1. The nodes are numbered 1 to 3, the circled numbers designate the branch numbers. The arrows indicate the direction of current flow within the branches. By popular convention a current branch leaving a node is positive and currents entering a node have a negative designation.

The arrows indicate the direction of the current flow relative to the nodes, and the circled numbers reference the voltage branches in the circuit. With this notation a nodal analysis

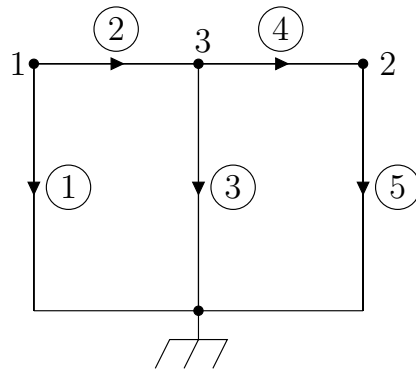


Figure 2.2: Diagram of nodes and branches enclosed within the dashed rectangle in Fig 2.1.

using the KCL, for each node yields

$$\begin{aligned} i_1 + i_2 &= 0 \\ -i_4 + i_5 &= 0 \\ -i_2 + i_3 + i_4 &= 0. \end{aligned} \quad (2.2)$$

This can be written in matrix form and will be called the incidence matrix  $A$ , where the rows represent the sum of the node currents and the columns are representative of the voltages on the branches

$$A = \begin{bmatrix} 1 & 1 & 0 & 0 & 0 \\ 0 & 0 & 0 & -1 & 1 \\ 0 & -1 & 1 & 1 & 0 \end{bmatrix}, \quad (2.3)$$

where,

$$a_{ij} = \begin{bmatrix} +1 & \text{if the branch } j \text{ leaves node } i \\ -1 & \text{if the branch } j \text{ enters node } i \\ 0 & \text{if the branch } j \text{ is not connected to node } i \end{bmatrix}. \quad (2.4)$$

When  $A$  is multiplied with the branch currents it produces the sum of all currents flowing out of each node

$$Ai_j = i_i = i_{\text{sum}} = 0. \quad (2.5)$$

Similarly when  $A^T$ , where  $T$  indicates the transpose of the matrix, is multiplied by the node voltages it results in the sum of the branch voltages

$$A^T v_i = v_j. \quad (2.6)$$

where  $v_i, v_j$  denotes the node- and branch voltage vectors respectively.

Equations (2.5) and (2.6) are the general matrix forms of the KCL and KVL respectively. Note that these results were obtained without any consideration of the circuit components. Also, as these results involved only additions and subtractions, they hold true for all linear operations, including Laplace transformations and for phasors, on  $i_j, v_j$  and  $v_i$ .

Let  $N$  be the number of branches within the circuit, and let  $j$  be the branch number. The power in each branch can now be summed to give

$$\sum_{j=1}^N [v_j i_j] = v_j^T i_j = A^T (v_i)^T i_j = v_i^T (A i_j) = 0, \quad (2.7)$$

which has the same argument of the integral of (2.1) and stated in words this equation is the conservation of power in the circuit.

### 2.1.1 The $z$ and $y$ parameters

Until now circuit components have not been taken into account. By returning focus to the lossless,  $LC$  circuit enclosed within the dashed rectangle in Fig. 2.1 the branch admittance matrix can be found.

The source and load conductances are ignored and a branch admittance matrix in Laplace form is written as

$$Y_j = \begin{bmatrix} Y_1 & 0 & 0 & 0 & 0 \\ 0 & Y_2 & 0 & 0 & 0 \\ 0 & 0 & Y_3 & 0 & 0 \\ 0 & 0 & 0 & Y_4 & 0 \\ 0 & 0 & 0 & 0 & Y_5 \end{bmatrix} = \begin{bmatrix} sC_1 & 0 & 0 & 0 & 0 \\ 0 & \frac{1}{sL_1} + sC_2 & 0 & 0 & 0 \\ 0 & 0 & sC_3 & 0 & 0 \\ 0 & 0 & 0 & \frac{1}{sL_2} + sC_4 & 0 \\ 0 & 0 & 0 & 0 & sC_5 \end{bmatrix}. \quad (2.8)$$

The branch currents and voltages related to the circuit components are given by

$$i_j = Y_j v_j = Y_j A^T v_i, \quad (2.9)$$

$$i_i = AY_j i_j = AY_j A^T v_i = Y_i v_i, \quad (2.10)$$

$$Y_i = AY_j A^T. \quad (2.11)$$

For the circuit in Fig 2.1, taking the components into consideration, the nodal admittance matrix is then given by

$$Y_i = \begin{bmatrix} \frac{(C_1+C_2)L_1 s^2+1}{L_1 s} & 0 & \frac{-(1+C_2 L_1 s^2)}{L_1 s} \\ 0 & \frac{(C_4+C_5)L_2 s^2+1}{L_2 s} & \frac{-(1+C_4 L_2 s^2)}{L_2 s} \\ \frac{-(1+C_2 L_1 s^2)}{L_1 s} & \frac{-(1+C_4 L_2 s^2)}{L_2 s} & \frac{(C_2+C_3+C_4)(L_1 L_2) s^2+L_1+L_2}{L_1 L_2 s} \end{bmatrix}. \quad (2.12)$$

The admittance matrix is well suited here as it is conveniently used with the incidence matrix  $A$  which stems from a nodal analysis. In principle a similar procedure may be followed to calculate the impedance matrix  $Z_n$  or the inverse of the admittance matrix can be calculated to give  $Z_n$ . Here the polynomial factors have been omitted, but (2.14) conveys the form of the elements, which is of concern in this discussion.

$$Y_n^{-1} = Z_n \quad (2.13)$$

$$Z_n = \begin{bmatrix} \frac{s^4(\cdot)+s^2(\cdot)+1}{\Delta} & \dots & \frac{s^4(\cdot)+s^2(\cdot)+1}{\Delta} \\ \vdots & \frac{s^4(\cdot)+s^2(\cdot)+1}{\Delta} & \vdots \\ \dots & \dots & \frac{s^4(\cdot)+s^2(\cdot)+1}{\Delta} \end{bmatrix} \quad (2.14)$$

The symbol  $\Delta$  represents the determinant of  $Y_n$  and is given by

$$\begin{aligned} \Delta = & s^5 L_{12} [C_{12}(C_{4+5}) + C_3(C_{1+2})(C_{4+5}) + C_{45}(C_{1+2})] \\ & + s^3 [L_1(C_{12} + (C_{1+2})(C_{3+5})) + L_2(C_{45} + (C_{4+5})(C_{1+3}))] \\ & + s(C_{1+3+5}). \end{aligned} \quad (2.15)$$

Here  $C_{12}$  is a short hand notation for  $C_1 C_2$  and  $L_{1+2}$  is shorthand for  $L_1 + L_2$ .

Note that for simple circuits in general it is easier to calculate  $Y_n$  than  $Z_n$  if the first and last branches are connected in parallel across the ports. For circuits with the first and last branches in series with the ports it is easier to calculate  $Z_n$  rather than  $Y_n$ . The  $Z_i$  matrix contains the open circuit parameters which can be measured e.g.

$$z_{12} = \left. \frac{V_1}{I_2} \right|_{I_1=I_3\dots I_N=0}, \quad (2.16)$$

and the  $Y_i$  matrix contains the short circuit parameters,

$$y_{21} = \left. \frac{I_2}{V_1} \right|_{V_1=V_3\dots V_N=0}. \quad (2.17)$$

Since node 3 is internal, there is no voltage or current signal applied to it. To find the  $z$ -parameters for the two-port  $LC$  circuit of figure 2.1 column and row 3 of  $Z_n$  is eliminated, which leaves

$$Z_{2p} = \begin{bmatrix} \frac{s^4 L_{12}(C_{45} + (C_{4+5})(C_{2+3})) + s^2 [L_1(C_{2+3+5}) + L_2(C_{4+5})] + 1}{\Delta} & \frac{s^4 L_{12} C_{24} + s^2 [L_1 C_2 + L_2 C_4] + 1}{\Delta} \\ \frac{s^4 L_{12} C_{24} + s^2 [L_1 C_2 + L_2 C_4] + 1}{\Delta} & \frac{s^4 L_{12}(C_{12} + (C_{1+2})(C_{3+4})) + s^2 [L_1(C_{1+2}) + L_2(C_{3+4+5})] + 1}{\Delta} \end{bmatrix}. \quad (2.18)$$

These results give a complete description of the port voltages and currents. At this point it may be prudent to point out several characteristics of  $Y_n$  and  $Z_n$  that are important to synthesis:

- The  $z$  and  $y$  parameters of  $LC$  circuits are rational functions with even numerators and odd denominators, or odd numerators with even denominators.
- The  $y$  and  $z$  parameters of  $LC$  circuits are odd,  $y_{i,i}(s) = -y_{i,i}(-s)$  and  $z_{i,i}(s) = -z_{i,i}(-s)$  [16].
- The  $Y_n$ ,  $Z_n$ ,  $Z_{2p}$  and  $Y_{2p} = Z_{2p}^{-1}$  matrices are symmetrical,  $Z_n = Z_n^T$  and  $z_{13} = z_{31}$  etc, which is a characteristic of all passive, reciprocal circuits [16].
- The poles and zeros of immittance functions all lie on the imaginary axis of the complex plane. This means that with  $s = j\omega$  the  $z_{ii}$  and  $y_{ii}$  port parameters are purely imaginary values with zero real part, indicating that these immittances are lossless, and pure reactive immittances  $jX$ .

## 2.1.2 The ABCD Transmission Parameters

So far the  $Z_n$  and  $Y_n$  matrices are used to characterize the two-port of Fig 2.1 but another set of important parameters are that of the cascade parameters, also known as the chain parameters or transmission parameters and they are extremely useful in circuit synthesis. Transmission parameters are usually denoted as

$$T = \begin{bmatrix} A & B \\ C & D \end{bmatrix}. \quad (2.19)$$

Fig 2.3 displays the four circuit configurations used to calculate the transmission parameters. The sub-figure numbering corresponds with the individual transmission parameters. Parameter  $A$  is found from the configuration shown in Fig. 2.3a, a voltage source is placed at port one with port two open circuit. Fig. 2.3b shows the configuration used to find parameter  $B$ , with a voltage applied to port one with port two shorted. From (2.20) it can be seen that the parameters are inverse transfer functions,

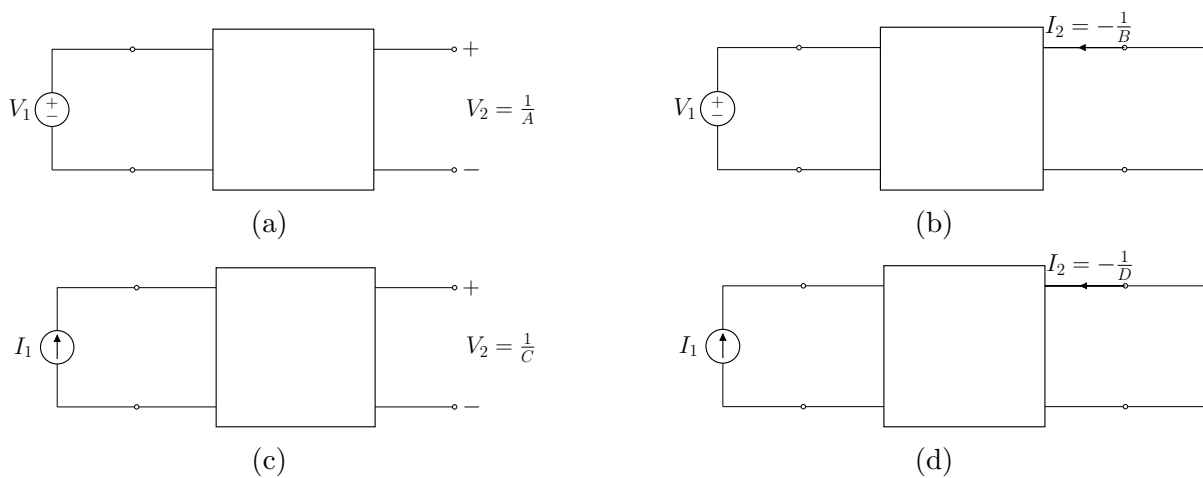


Figure 2.3: The different configurations used to find the ABCD Parameters for a two-port network. a) A voltage source at port one with port two open circuit. b) A voltage source at port one with a short circuit at port two. c) A current source at port one with an open circuit at port two. d) A current source at port one with port two short-circuited.

$$A = \frac{1}{\left. \frac{V_2}{V_1} \right|_{I_2=0}}, \quad B = \frac{1}{\left. \frac{-I_2}{V_1} \right|_{V_2=0}}, \quad C = \frac{1}{\left. \frac{V_2}{I_1} \right|_{I_2=0}}, \quad D = \frac{1}{\left. \frac{-I_2}{I_1} \right|_{V_2=0}}, \quad (2.20)$$

where the voltage ratio is given by parameter  $\frac{1}{A}$  from Fig. 2.3a

$$A_v = \frac{V_2}{V_1}, \quad (2.21)$$

the transfer admittance is given by  $\frac{1}{B}$  from Fig. 2.3b

$$Y_T = \frac{I_2}{V_1}, \quad (2.22)$$

the transfer impedance is given by  $\frac{1}{C}$  from Fig. 2.3c

$$Z_T = \frac{V_2}{I_1}, \quad (2.23)$$

and the current ratio is given by  $\frac{1}{D}$  from Fig. 2.3d. From the above equations it follows that

$$\begin{bmatrix} V_1 \\ I_1 \end{bmatrix} = \begin{bmatrix} A & B \\ C & D \end{bmatrix} \begin{bmatrix} V_2 \\ -I_2 \end{bmatrix} = T \begin{bmatrix} V_2 \\ -I_2 \end{bmatrix}. \quad (2.24)$$

The transmission parameters have some interesting properties to note:

- The transmission matrix for cascaded circuits with conformal port dimensions can easily be found by multiplying the transmission matrices of the individual circuits.
- The determinant  $\Delta T = AD - BC = 1$  for reciprocal circuits. This is a particularly interesting characteristic of which the importance will become clear in section 2.3
- For a reciprocal circuit, when the ports are reversed, A and D simply interchange.

### 2.1.3 Scattering Parameters

Up to this point the discussion has been limited to a passive, lumped element two-port, reciprocal circuit. However the  $Z$  and  $Y$  matrices do not exist for all elements and circuits. Well-known examples include two-ports consisting of a single shunt or series element, three-port junctions and the ideal transformer [16]. S-parameters on the other hand holds true for any  $N$ -port passive circuits and like the  $Z$  and  $Y$  parameters give a complete description of the network as seen at its  $N$  ports. It does not give any more information on a circuit's characteristics than the  $Z$  and  $Y$  matrices, it is the same information, only presented in a different way. Impedance and admittance parameters relate total voltage and currents at the network ports, where S-parameters relate the voltage waves incident on the ports to those reflected from the ports [18]. The  $Z$  and  $Y$  matrices, and by implication the  $ABCD$ -parameters, can in fact be converted into S-parameters [18].

Due to S-parameters being directly related to power flows, it is well suited for synthesis of terminated two-ports because the starting point for such synthesis is the power transfer function.

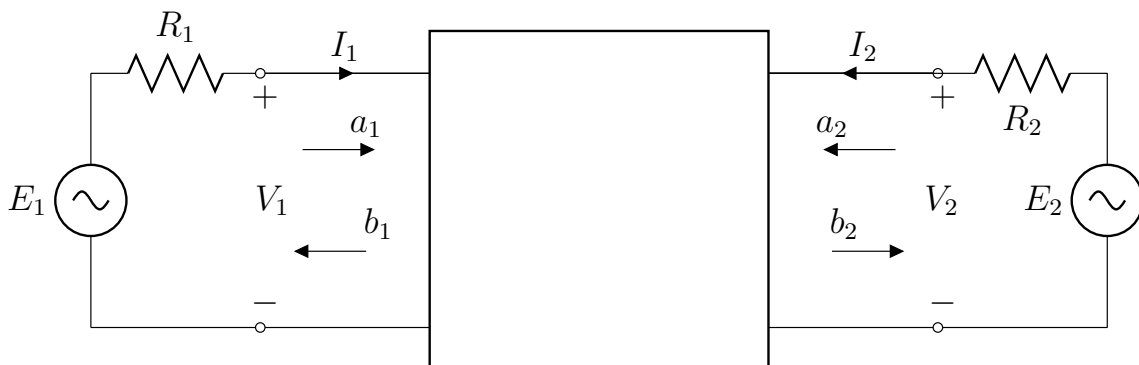


Figure 2.4: Doubly terminated two-port network illustrating the parameter for defining S-parameters.

The resistively terminated two-port from Fig. 2.4 illustrates the definition of incident and reflected variables and the circuit is characterised by a scattering matrix given as

$$\begin{bmatrix} b_1 \\ b_2 \end{bmatrix} = \begin{bmatrix} S_{11} & S_{12} \\ S_{21} & S_{22} \end{bmatrix} \begin{bmatrix} a_1 \\ a_2 \end{bmatrix}, \quad (2.25)$$

where the scattering elements are:

$$S_{11} = \left. \frac{b_1}{a_1} \right|_{a_2=0}, \quad S_{12} = \left. \frac{b_1}{a_2} \right|_{a_1=0}, \quad S_{21} = \left. \frac{b_2}{a_1} \right|_{a_2=0}, \quad S_{22} = \left. \frac{b_2}{a_2} \right|_{a_1=0}. \quad (2.26)$$

Let  $V_i^+(s) = \frac{E_i(s)}{2\sqrt{R_i}}$  be the incidence voltage, and let  $I_i^+(s) = \frac{E_i(s)}{2R_i} = \frac{V_i^+(s)}{R_i}$  be the incidence current and  $i$  denotes the port number. Then the incidence wave amplitude is given by

$$a_i \triangleq \frac{V_i^+}{\sqrt{R_i}} = \sqrt{R_i} I_i^+ = \frac{E_i}{2\sqrt{R_i}}. \quad (2.27)$$

Similarly let  $V_i^-(s) = V_i - V_i^+ = \frac{E_i Z_{load}}{Z_{load} + R_i} - \frac{E_i}{2}$  be the reflected voltage and  $I_i^- = I_i^+ - I_i = \frac{V_i^-}{R_i}$  be the reflected current, where  $R_{load}$  assumes the load impedance when the opposing generator is replaced with some load. The reflected wave amplitude is then given by

$$b_i \triangleq \frac{V_i^-}{\sqrt{R_i}} = \sqrt{R_i} I_i^- = \frac{E_i}{2R_i} \frac{Z_{load} - R_i}{Z_{load} + R_i}. \quad (2.28)$$

The S-parameters are then directly calculated and given by the following equations and common measurement terms

$$S_{11} = \left. \frac{b_1}{a_1} \right|_{a_2=0} = \left. \frac{2\sqrt{R_1} V_1 - R_1 I_1}{2\sqrt{R_1} V_1 + R_1 I_1} \right|_{E_2=0} = \frac{Z_1 - R_1}{Z_1 + R_1}, \quad (2.29)$$

$S_{11}$  is known as the forward reflection coefficient (input match).

$$S_{21} = \left. \frac{b_2}{a_1} \right|_{a_2=0} = \left. \sqrt{\frac{R_1}{R_2}} \frac{V_2 - R_2 I_2}{V_1 - R_1 I_1} \right|_{E_2=0} = \left. \sqrt{\frac{R_1}{R_2}} \frac{2V_2}{E_1} \right|_{E_2=0}, \quad (2.30)$$

$S_{21}$  is the forward transmission coefficient gain or loss. With sinusoidal conditions with the root mean squared (RMS) phasors, the quantity is given by

$$\left| S_{21} \right|^2 = \left. \frac{4R_1 |V_2|^2}{R_2 |E_1|^2} \right|_{E_2=0} = \frac{P_{load}}{P_{source}}. \quad (2.31)$$

This is the well-known transducer power gain equation for two-port networks and is of great importance in network synthesis. It is a measure of how much of the energy supplied to a circuit's input will be available to a load at a circuit's output port for a given frequency. For reciprocal circuits  $S_{21} = S_{12}$ . It is the ratio of the power available to the load to the power available from the source. The extension of these results to general N-port network are easily done.

For the lossless two-port in Fig. 2.1 the scattering matrix takes on the form

$$S = \begin{bmatrix} \frac{s^5(\cdot) + s^3(\cdot) + s(\cdot)}{s^5(\cdot) + s^4(\cdot) + s^3(\cdot) + s^2(\cdot) + s(\cdot) + 1} & \frac{s^4(\cdot) + s^2(\cdot) + 1}{s^5(\cdot) + s^4(\cdot) + s^3(\cdot) + s^2(\cdot) + s(\cdot) + 1} \\ \frac{s^4(\cdot) + s^2(\cdot) + 1}{s^5(\cdot) + s^4(\cdot) + s^3(\cdot) + s^2(\cdot) + s(\cdot) + 1} & \frac{s^5(\cdot) + s^3(\cdot) + s(\cdot)}{s^5(\cdot) + s^4(\cdot) + s^3(\cdot) + s^2(\cdot) + s(\cdot) + 1} \end{bmatrix}. \quad (2.32)$$

Unlike the  $z$  and  $y$  parameters, the numerator of the S-parameters contain all powers of  $s$  without any missing terms. In the following sections it may be seen that where the poles and zeros for the  $z$  and  $y$  parameters all lie on the imaginary axis of the  $s$ -plane, the poles and zeros for the S-parameters all lie inside the left-half of the  $s$ -plane.

### 2.1.4 Summary

This section has given a brief overview of analysis techniques with different parameter descriptions and how they are obtained. A doubly terminated, lossless, reciprocal two-port network served as the example that illustrated how S-parameters provides the clearest view of a circuit's performance, where  $z$ ,  $y$  and  $ABCD$  parameters relate directly to circuit elements. The properties of each set of parameter descriptions, provide usefulness in different steps in circuit synthesis. The circuit response may be specified in S-parameters, which may then be converted to other parameter description best suited to extract element values.

## 2.2 Realizability Conditions

Before commencement of a circuit design it is necessary to answer the question: What is physically realizable using only resistive  $R$ , inductive  $L$ , capacitive  $C$  and mutually inductive  $M$  elements? It helps to know what is possible, and the implicit maximum performance constraints set the benchmark against which the performance of a physical circuit may be evaluated. This section starts by examining the mathematical conditions required for an arbitrary impedance function to be realisable. Then the required S-parameters conditions are presented and linked with the conditions of impedance function. As the focus is on purely reactive circuits, the remainder of the section presents the canonical and non-canonical implementations of  $LC$  immitances often accompanied by numerical examples. Numerical examples are used instead of variables, as the equations become tedious when written with general variables.

Although a detailed discussion on realizability conditions and the derivation thereof is beyond the scope of this discussion, it is important to present a brief overview of the fundamentals on which these conditions are established, for it will be of reference during the synthesis example.

An appropriate starting point for this section is the transfer function of one-port networks. The impedance function of a one-port network is given by the ratio of the input voltage phasor to input current phasor

$$Z(s) = \frac{V(s)}{I(s)}, \quad (2.1)$$

where  $s$  is the complex frequency variable  $s = j\omega$ .

In general, a passive, lossless one-port network's transfer impedance can be expressed as a ratio of an input voltage phasor to an input current phasor which is given as a ratio of polynomials in  $s$  [16]

$$Z(s) = \frac{N(s)}{D(s)} = \frac{k_n s^n + k_{n-1} s^{n-1} + \dots + k_1 s^1 + n_0}{l_m s^m + l_{m-1} s^{m-1} + \dots + l_1 s^1 + l_0}. \quad (2.33)$$



In 1931 Otto Brune proved that  $Z(s)$  may be realized using only *RLCM* elements (where all  $R$ ,  $L$ ,  $C$  and  $M$  are positive) if and only if  $Z(s)$  is a positive real rational function in  $s$  [19, 20].  $Z(s)$  is considered to be a positive, real function if the following conditions hold:

- $Z(s)$  is a real rational function of  $s$ , where all  $c_i$ ,  $d_i$  are real, and therefore  $Z(s)$  is real if  $s$  is real.
- $Z$  is positive, real for all real  $\omega$

$$\Re(Z(j\omega)) \geq 0 \quad \forall \omega \in \mathbb{R}. \quad (2.34)$$

- All poles of  $Z(s)$  are in the closed LHP of the  $s$ -plane. All poles must be simple, with real residues. Since  $s = 0$  and  $s \rightarrow \infty$  lie on the  $j\omega$ -axis, this holds also for poles at the origin and at infinity.

### 2.2.1 Realizability Conditions for S-parameters

Now consider again the circuit of Fig. 2.4 along with its scattering parameters. If (2.1) holds for the passive circuit, then the total power supplied, is equal to the sum of the reflected power, the power delivered and the power dissipated within the circuit. Using the RMS values under continuous excitation, with  $s = j\omega$ , the power absorbed by the circuit is given by

$$P_{diss} = \Re(V_1 I_1^* + V_2 I_2^*) = \frac{1}{2}(V_1 I_1^* + V_2 I_2^* + V_1^* I_1 + V_2^* I_2). \quad (2.35)$$

Substituting the port voltages  $V_i = V_i^+ + V_i^-$ , and port currents  $I_i = I_i^+ - I_i^-$  with the incidence and reflected wave amplitudes from (2.27) and (2.28), the power dissipated within the circuit can be written as

$$\begin{aligned} P_{diss} &= \frac{1}{2} \left( \frac{\sqrt{R_1}}{\sqrt{R_1}} (a_1 + b_1)(a_1^* + b_1^*) + (a_1^* + b_1^*)(a_1 - b_1) \right. \\ &\quad \left. + (a_2 + b_2)(a_2^* - b_2^*) + (a_2^* + b_2^*)(a_2 - b_2) \right) \\ &= a_1 a_1^* + a_2 a_2^* - b_1 b_1^* - b_2 b_2^* \end{aligned} \quad (2.36)$$

$$= \begin{bmatrix} a_1^* & a_2^* \end{bmatrix} \begin{bmatrix} a_1 \\ a_2 \end{bmatrix} - \begin{bmatrix} b_1^* & b_2^* \end{bmatrix} \begin{bmatrix} b_1 \\ b_2 \end{bmatrix}$$

$$= a^{*\top} a - a^{*\top} S^{*\top} S \cdot a \quad \text{by substitution of (2.25)}$$

$$= a^{*\top} (I - S^{*\top} S) a,$$

where  $I$  is the identity matrix and  $I - S^{*\top} S$  is the dissipation matrix of the two-port, and in terms of scattering parameters it is written as

$$I - S^{*\top} S = \begin{bmatrix} 1 - |S_{11}|^2 - |S_{21}|^2 & S_{11}^* S_{12} + S_{21}^* S_{22} \\ S_{11} S_{12}^* + S_{21} S_{22}^* & 1 - |S_{22}|^2 - |S_{12}|^2 \end{bmatrix}. \quad (2.37)$$

For passive circuits (2.1) requires  $P_{diss} \geq 0$ , and for a lossless circuit  $P_{diss} = 0$  because no power is dissipated within the circuit. In this case, for a non-zero  $a$ , it must be that

$$I = S^{*\top} S. \quad (2.38)$$

Equation (2.38) is the general requirement for  $S$  to be a unitary matrix [18]. For  $P_{diss} \geq 0$  to hold,  $S$  is required to be a positive semi-definite matrix so that for non-negative  $a$ ,  $P$  will be positive and real. Stated formally,

$$S \text{ positive semi-definite} \iff a^\top S a \geq 0 \quad \forall a \in \mathbb{R}. \quad (2.39)$$

From (2.38) it is seen that for a lossless, passive network with non-zero incidence waves, it is required that the elements on the diagonal and the determinant of  $S^{*\top} S$  must be zero. In summary, a passive, lossless circuit is realizable under the following conditions related to the scattering matrix

$$1 - S_{11}^* S_{11} - S_{21}^* S_{21} = 0 \quad (2.40)$$

$$1 - S_{22}^* S_{22} - S_{12}^* S_{12} = 0 \quad (2.41)$$

$$S_{11}^* S_{12} + S_{21}^* S_{22} = 0 \quad (2.42)$$

$$S_{11} S_{12}^* - S_{21} S_{22}^* = 0. \quad (2.43)$$

If the circuit in Fig. 2.4 is open-circuited, essentially rendering it as a passive lossless one-port, then (2.1) requires that

$$S_{11}^* S_{11} = 1. \quad (2.44)$$

$S_{11}$  is the ratio of the reflected wave amplitude to the incident wave amplitude and therefore may reasonably be expressed as a rational function, that is, as the ratio of polynomials

$$S_{11} = \frac{F(s)}{E(s)}. \quad (2.45)$$

Consider the polynomial

$$E(s) = a_0 s^n + a_1 s^{n-1} + \dots + a_n, \quad a_1, \dots, a_n \in \mathbb{R}, a_0 > 0, \quad (2.46)$$

and let  $n$  be the degree of  $E(s)$  and define  $l = \frac{n}{2}$ . The polynomial  $E(s)$  can always be represented as

$$E(s) = E_e(s^2) + s E_o(s^2), \quad (2.47)$$

where, for  $n = 2l$ ,

$$\begin{aligned} E_e(u) &= a_0 u^l + a_2 u^{l-1} + \dots + a_n, \\ E_o(u) &= a_1 u^{l-1} + a_3 u^{l-2} + \dots + a_{n-1}, \end{aligned} \quad (2.48)$$

and for  $n = 2l + 1$ ,

$$\begin{aligned} E_e(u) &= a_1 u^l + a_3 u^{l-1} + \dots + a_n, \\ E_o(u) &= a_0 u^l + a_2 u^{l-1} + \dots + a_{n-1}. \end{aligned} \quad (2.49)$$

The polynomials  $E_e(s^2)$  and  $E_o(s^2)$  satisfy the following equalities:

$$\begin{aligned} E_e(s^2) &= \frac{E(s) + E(-s)}{2}, \\ E_o(s^2) &= \frac{E(s) - E(-s)}{2s}. \end{aligned} \quad (2.50)$$

The convenience of the equalities above become apparent when (2.45) is substituted into (2.44) so that

$$\begin{aligned} S_{11}^* S_{11} &= \frac{F(s)F(-s)}{E(s)E(-s)} = 1 \\ \Rightarrow F(s)F(-s) &= \pm E(s) \pm E(-s) \\ \Rightarrow S_{11}^* S_{11} &= \frac{\pm E(s) \pm E(-s)}{E(s)E(-s)} = 1. \end{aligned} \quad (2.51)$$

Returning to the discussion leading up to (2.33),  $Z(s)$  is found in terms of  $S_{11}$  from (2.29)

$$\begin{aligned} Z(s) &= R_1 \frac{1 + S_{11}}{1 - S_{11}} \\ &= R_1 \frac{E(s) + E(-s)}{E(s) - E(-s)} \\ &= R_1 \frac{E_e(s) + E_o(s) \pm (E_e(s) - E_o(s))}{E_e(s) + E_o(s) \mp (E_e(s) - E_o(s))} \\ &= R_1 \frac{E_e(s)}{E_o(s)} \text{ or } R_1 \frac{E_o(s)}{E_e(s)}. \end{aligned} \quad (2.52)$$

This concludes the connection between Brune's realizability conditions and the S-parameters of an arbitrary passive two-port network. It is easily shown for any passive N-port. Another important property of the polynomial  $E(s)$  stems from the ratio  $\frac{E_o(s)}{E_e(s)}$  in (2.52) and is called the associated function  $\Phi$  of the polynomial  $E(s)$ ,

$$\Phi = \frac{E_o(s)}{E_e(s)}. \quad (2.53)$$

From (2.50) and (2.53) the following relations are derived:

$$\begin{aligned} s\Phi(s^2) &= \frac{E(s) - E(-s)}{E(s) + E(-s)} = \frac{1 - \frac{E(-s)}{E(s)}}{1 + \frac{E(-s)}{E(s)}}, \\ \frac{E(-s)}{E(s)} &= \frac{1 - s\Phi(s^2)}{1 + s\Phi(s^2)} \end{aligned} \quad (2.54)$$

The associated function  $\Phi$  is an  $R$ -function. An  $R$ -function is a function mapping the upper half-plane of the complex plane to the lower half-plane. These functions have real, simple, and interlacing zeros and poles [21]. For Brune's realizability conditions to hold,  $E(s)$  must be a stable polynomial, also known as Hurwitz polynomials. Some important properties to note about Hurwitz polynomials are that

- Hurwitz polynomials have all its zeros in the open LHP of the complex plane.
- The coefficients of a Hurwitz polynomial are all positive (Stodola theorem).
- $E(s)$  is a Hurwitz polynomial, if and only if, its associated function  $\Phi = \frac{E_o(s)}{E_e(s)}$  is a  $R$ -function with exactly  $l$  poles, all of which are negative, and the limit  $\lim_{s \rightarrow \pm\infty} \Phi(s)$  is positive whenever  $n = 2l + 1$ . Where,  $n$  is the degree of  $E(s)$  and  $l = \frac{n}{2}$  [21].

- The polynomial  $E$  of degree  $n \geq 1$  defined in (2.46) is Hurwitz stable if and only if its associated function  $\Phi$  has the following Stieltjes continued fraction expansion given in (2.55)

$$\Phi(s) = c_0 + \frac{1}{c_1 s + \frac{1}{c_2 + \frac{1}{c_3 s + \frac{1}{\ddots + \frac{1}{c_{2l-1} s + \frac{1}{c_{2l}}}}}}}, \quad \text{with } c_i > 0, \quad i = 1, \dots, 2l, \quad (2.55)$$

where  $c_0 = 0$  if  $n$  is even,  $c_0 > 0$  if  $n$  is odd, and  $l = \frac{n}{2}$  [21].

If  $E(s)$  is a Hurwitz polynomial then all the realizability conditions are satisfied.

## 2.2.2 Canonical Realizations of LC Immitances

Well known approaches to finding a circuit realization of a  $LC$  immittance include the Cauer I, Cauer II, Foster I, and Foster II canonical forms. The Cauer and Foster forms are called canonical implementations of  $Z_{LC}$ , because they realize immittance functions using the minimum possible number of components. The minimum number of elements required to realize an immittance function is  $n$ , the degree of the polynomial  $Z_{LC}$ . Cauer forms use a continued fraction expansion of  $Z_{LC}$ . Cauer I repeatedly extract poles from infinity, where Cauer II extract poles from the origin. A finite pole pair extraction is also possible by doing a partial fraction expansion of an impedance function to realize the Foster I form. Doing the same but using an admittance function instead realizes the Foster II form.

The canonical forms are best illustrated by way of example. Using a simple Hurwitz polynomial, the canonical forms results in four different circuit realizations. Let  $E(s)$  be the Hurwitz polynomial,

$$\begin{aligned} E(s) &= 1 + 8s + s^2 + 2s^3, \\ E_e(s) &= 1 + s^2, \\ E_o(s) &= 8s + 2s^3. \end{aligned} \quad (2.56)$$

Let  $Z(s)$  be the impedance function,

$$Z(s) = \frac{E_o(s)}{E_e(s)} = \frac{8s + 2s^3}{1 + s^2}. \quad (2.57)$$

### Cauer I

Synthesis with Cauer I repeatedly extract poles at  $s \rightarrow \infty$  from immittance functions. The Cauer I realization is shown in Fig. 2.5a and its form is found by doing a continued fraction expansion of the function similar to that of (2.55). Cauer I realization consists of

a ladder circuit of shunt capacitors and series inductors which is most useful in low-pass filters.

$$Z(s) = 2s + \frac{1}{\frac{s}{6} + \frac{1}{6s}} \quad (2.58)$$

### Cauer II

Cauer II synthesis requires the repeated extraction of poles at  $s \rightarrow 0$  from the immittance function. The Cauer II realization is shown in Fig. 2.5b. It consists of a ladder network of shunt inductors and series capacitors and has best suited for high-pass filters.

$$Z(s) = \frac{1}{\frac{1}{8s} + \frac{1}{\frac{3}{32^s} + \frac{1}{\frac{8}{3^s}}}}$$

### Foster I

Fig. 2.5c shows the Foster I realization. The Foster I form is the partial fraction expansion of the impedance function  $Z(s)$ . The first form realizations are synthesised from parallel  $LC$  resonators connected in series, and is associated with band-pass filters.

$$Z(s) = 2s + \frac{1}{\frac{s}{6} + \frac{1}{6s}} \quad (2.59)$$

### Foster II

The Foster II realization is displayed in Fig. 2.5d. The Foster II form is found by partial fraction expansion of the admittance function  $Y(s)$ . The circuit is formed with series  $LC$  resonant circuits connected in parallel.

$$\begin{aligned} Y(s) &= \frac{1 + s^2}{8s + 2s^3} \\ &= \frac{1}{8s} + \frac{1}{\frac{8}{3^s} + \frac{1}{\frac{32^s}{3}}} \end{aligned} \quad (2.60)$$

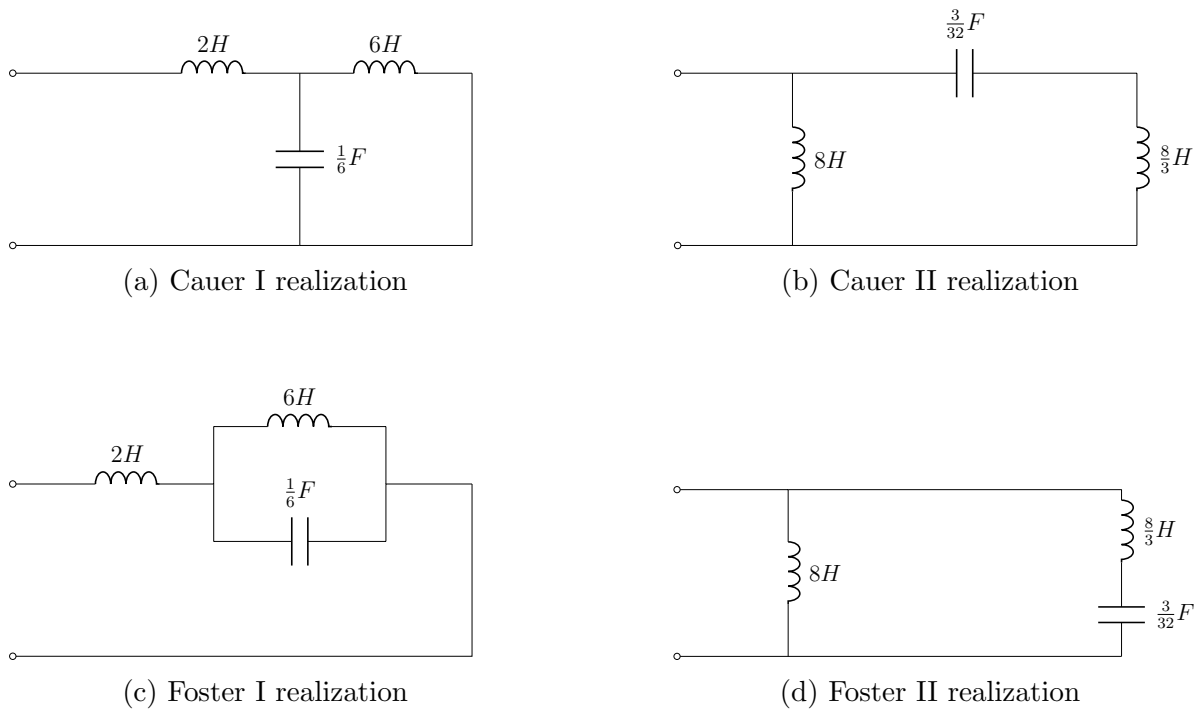


Figure 2.5: Equivalent circuits for  $Z(s) = \frac{8s+2s^3}{1+s^2}$  using Cauer I, II and Foster I, II realizations

### 2.2.3 Non-Canonical Realizations of LC Immitances

The canonical realizations provide poles and zeros at  $s = \infty$  and  $s = 0$ . Network synthesis sometimes require specific features such as a branch that contains a circuit resonant at a given frequency. The implementation of such features usually requires more than the minimum number of  $LC$  elements. By partially removing a pole, the zeros of the transfer function is shifted in the direction of the pole being removed. The pair of zeros closest to the pole move the most.

An example may serve to demonstrate partial pole removal and zero shifting of an arbitrary Hurwitz polynomial. Let

$$\begin{aligned}
 E(s) &= (s+1)^4 \\
 &= s^4 + 4s^3 + 6s^2 + 4s + 1 \\
 E_e(s) &= s^4 + 6s^2 + 1 \\
 E_o(s) &= 4s^3 + 4s = 4s(s^2 + 1)
 \end{aligned} \tag{2.61}$$

so a realizable impedance function is given by

$$Z_{LC} = \frac{E_e}{E_o} = \frac{s^4 + 6s^2 + 1}{4s^3 + 4s} \tag{2.62}$$

which has a pole at  $s \rightarrow \infty$  and a residue of  $\frac{1}{4}$ . The pole at infinity is partially removed by extracting a series inductor from the function

$$\begin{aligned} Z_2 &= \frac{s^4 + 6s^2 + 1}{4s^3 + 4s} - ks, k < k_\infty = \frac{1}{4} \\ &= \frac{(1 - 4k)s^4 + (6 - 4k)s^2 + 1}{4s^3 - 4s}. \end{aligned} \quad (2.63)$$

Fig. 2.6 displays how the zeros, in this case only the zeros of the positive half of the imaginary plane, are shifted as the pole at infinity is partially removed bit by bit.

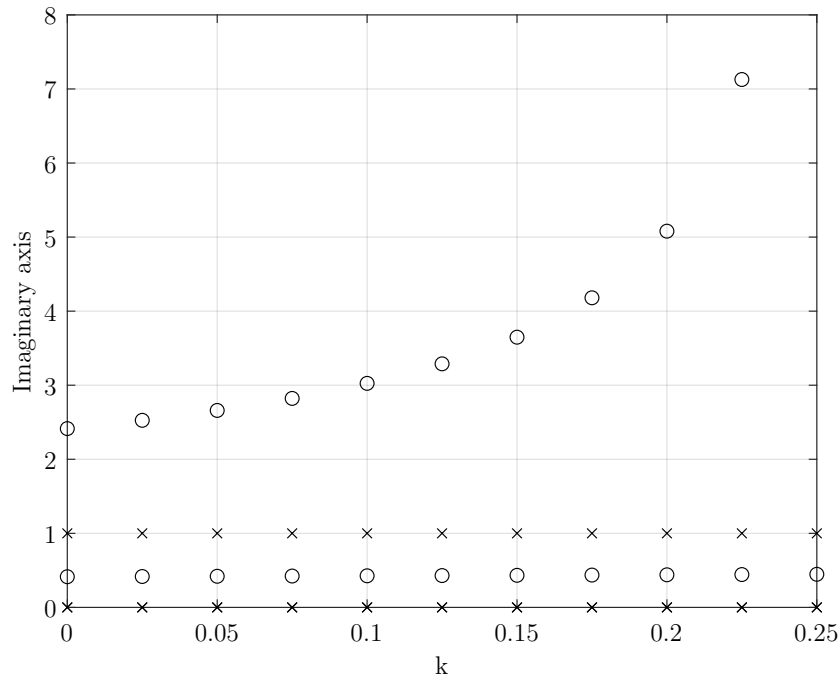


Figure 2.6: Zero shifting by partial removal of a pole at infinity for an  $LC$  immittance function. Only the positive half of the imaginary axis is shown. As  $k$  increases, the zeros of the pole being removed, shifts. When the the pole is removed completely, the zero shifts to infinity.

A resonance branch may be realized at  $s = \pm j3$  by partially removing the pole at infinity. Solve for  $k$  from (2.63):

$$\begin{aligned} (1 - 4k)s^4 + (6 - 4k)s^2 + 1|_{s^2=-9} &= 0 \\ 288k &= 28 \\ k &= \frac{7}{72}. \end{aligned} \quad (2.64)$$

Now extract an inductor  $L_1 = \frac{7}{72} \approx 0.09722$  from  $Z_{LC}$  to leave

$$Z_2 = \frac{11s^4 + 101s^2 + 18}{72s^3 + 72s}. \quad (2.65)$$

The reciprocal  $Y_2 = \frac{1}{Z_2}$  has a pair of poles at  $s = \pm j3$  and a residue given by

$$k = \lim_{s \rightarrow -j3} Y_2 \frac{s^2 + 9}{s} = \frac{576}{97}. \quad (2.66)$$

Removing the pole to find  $Y_3$  by subtracting the admittance

$$Y_b = \frac{\frac{576}{97}s}{s^2 + 9} \quad (2.67)$$

from  $Y_2$

$$Y_3 = Y_2 - \frac{\frac{576}{97}s}{s^2 + 9} = \frac{648s}{1067s^2 + 194} \quad (2.68)$$

$$Z_3 = \frac{1067s^2 + 194}{648s}.$$

$Z_3$  has a pole at infinity with residue  $\frac{1067}{648}$  that can be removed by extracting an inductor  $L_3$  to find  $Z_4$

$$Z_4 = Z_3 - \frac{1067}{648}s = \frac{97}{324s} \quad (2.69)$$

$$Y_4 = \frac{324s}{97} \approx 3.34021s = sC_4.$$

$Y_4$  has pole as  $s \rightarrow \infty$ . The branch impedance  $Z_b$  is

$$Z_b = \frac{1}{Y_b} = \frac{97}{576}s + \frac{97}{64s}$$

$$\approx 0.1684s + \frac{1}{0.65979s} \quad (2.70)$$

$$= sL_b + \frac{1}{sC_b}$$

Fig. 2.7 shows the implementation of  $Z_{LC}$  with a resonant branch at  $s = \pm j3$ .

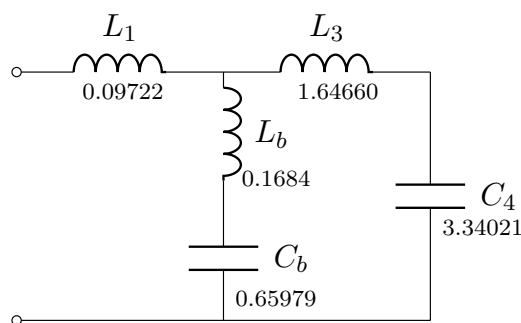


Figure 2.7:  $Z_{LC}$  with a resonant branch at  $s \pm j3$ .

In general, the loss poles are obtained through a resonance in a shunt branch or through antiresonance in a series branch [16]. Fig. 2.9 shows the realization of the resonant branch implementations.



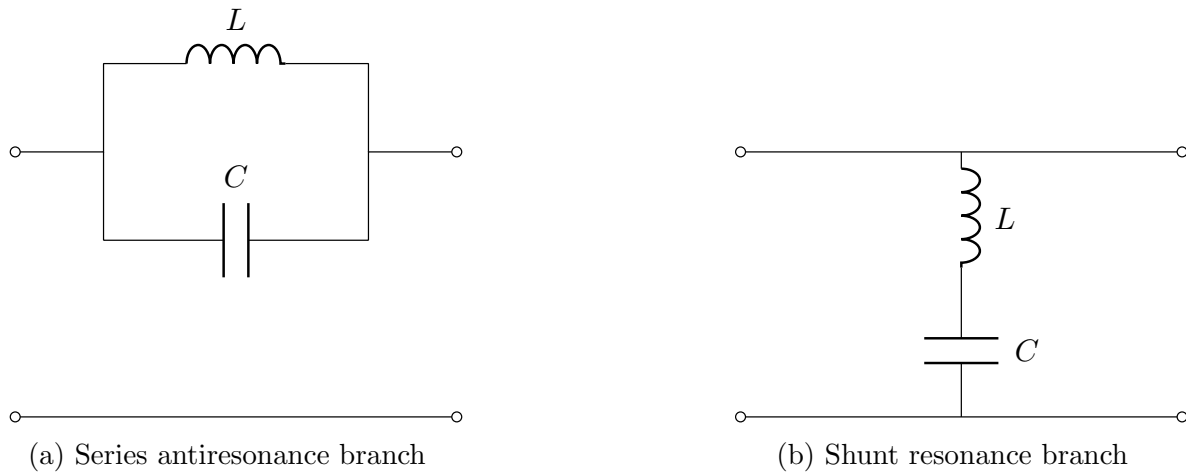


Figure 2.8: Loss poles are obtained through (a) a series antiresonance branch or (b) a shunt resonance branch.

Partial pole removal is summarised as follows:

- The partial removal of a pole shifts the zeros toward the pole being removed.
- A zero cannot be shifted beyond an adjacent pole.
- The complete removal of a pole at infinity shifts the adjacent zero to infinity, the complete removal of a pole at the origin shifts the adjacent zero to the origin, and the complete removal of a pair of complex conjugate poles shifts two adjacent zeros toward the positions of the removed poles.
- The partial or complete removal of a pole at the origin does not affect a zero at infinity, nor does the partial or complete removal of a pole at infinity affect a zero at the origin.
- There are limits on the amount a given partial pole removal can shift a given zero. However, by using several steps of zero shifting, some zero can be moved to a desired location on the  $j\omega$ -axis.

### Brune Section

The implementation of a resonant branch as above forms the foundation for Brune section realizations. Brune sections are important in the design of practical doubly terminated ladder networks and impedance transformers. By repetition of the previous example, realizing  $Z_L C$  with a branch resonant at a prescribed frequency by completely removing the pole at  $s \rightarrow \infty$  with the extraction of a series inductor leaves

$$\begin{aligned}
 Z_{LC} &= \frac{s}{4} + \frac{5s^2 + 1}{4s^3 + 4s} \\
 &= sL_1 + Z_2 \\
 Z_2 &= \frac{5s^2 + 1}{4s^3 + 4s}
 \end{aligned} \tag{2.71}$$

that has a zero at infinity. Restoring a part of the pole that was removed, by removing a negative inductance  $-L_1$  to shift the zeros to  $s = \pm j3$

$$Z_3 = Z_2 - s(-L_1) \quad (2.72)$$

and solving for  $L_1$  by shifting zeros to  $s = \pm j3$  from

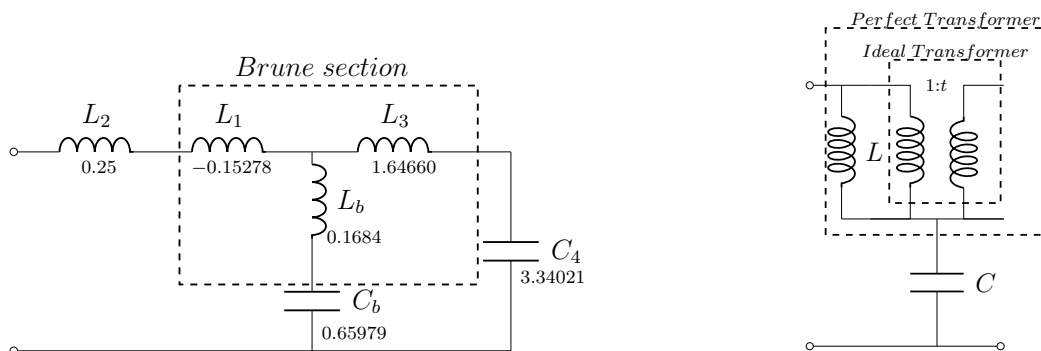
$$\frac{5s^2 + 1}{4s^3 + 4s} + sL_1|_{s=\pm j3} = 0 \quad (2.73)$$

$$L_1 = \frac{11}{72}.$$

This leaves

$$Z_2 = \frac{11s^4 + 101s^2 + 18}{72s^3 + 72s}. \quad (2.74)$$

which is exactly the same as  $Z_2$  in (2.65) from the previous example. The synthesis is completed identically to find circuit shown in Fig 2.9a. An equivalent circuit is given in Fig 2.9b showing how Brune sections may be synthesized to give various equivalent circuit realizations by shifting zeros from infinity or away from zero with pole extractions with series or parallel elements given identical circuit parameters.



(a)  $Z_{LC}$  realization of a resonant branch at  $s \pm j3$  using a Brune section.

(b)  $Z_{LC}$  equivalent circuit realization with a Brune section.

Figure 2.9: Equivalent circuit realizations of a resonance branch at  $s^2 = -9$  (a) Realization of a resonant branch at  $s \pm j3$  using a Brune section. (b)  $Z_{LC}$  equivalent circuit realization with a Brune section identical to an ideal transformer.

## 2.2.4 Summary

This section presented the pure mathematical criteria required to realize doubly terminated, passive  $LC$  networks. Practical realization in canonical Cauer I, II, Foster I, II forms were given as a method to realize circuits with a minimum number of elements and non-canonical Brune sections realization by means of partial pole extraction and zero shifting were discussed as a method for realization series and shunt resonance branches and ideal transformer circuits. The methods presented are well known network synthesis techniques, that are of fundamental importance in the design of filter and transformer networks. The concepts discussed in this section will be applied in following section, which forms the foundation the compact design.

## 2.3 The Short-Step-Stub Chebyshev Impedance Transformer

This section forms the foundation of the compact power combiner design presented in this thesis and is based on a paper by Van Der Walt [2]. Power combiners are essentially impedance transformer networks that match the impedance from a central port (usually  $50 \Omega$ ) to multiple peripheral ports. The number of peripheral ports are denoted by  $N$  and the corresponding combiner is classified as an  $N$ -way combiner. The well-known quarter-wave impedance transformer provides a convenient way of matching between resistive ports. These transformers have the benefit of easy implementation as all impedances lie within the range of the port resistances, but have the disadvantage of being relatively long, especially at lower microwave frequencies. For more compact designs in microwave integrated circuits, short-step transformers are sometimes used with lengths of  $\frac{1}{12}$  or  $\frac{1}{16}$  of a wavelength at the center frequency of the response. Short-step transformers are generally more difficult to implement than quarter-wave transformers due to the large step discontinuities resulting from the large ratio of impedances within the transformer. These restrictions on realizability and implementation are reduced by Levy [22] and even further by Van Der Walt [2] with techniques utilising shunt stub lines that greatly reduce the ratio of the largest to smallest impedance in the transformer. In his paper Van Der Walt outlines the procedure to synthesize a short-step-stub Chebyshev impedance transformer of order  $n$  with commensurate<sup>2</sup> transmission lines to match between ports with a given resistance ratio and specified bandwidth. Fig. 2.10 displays a  $\frac{\lambda}{16}$  line short-step stub transformer and a quarter wave transformer in a stripline layout for comparison. The short-step transformer resembles a ladder configuration. The theory and techniques presented in the previous section provide the means to dissect the synthesis procedure presented in [2] that will ultimately allow a condense design of a coaxial wave guide power combiner with a similar technique as that of the stripline configuration in Fig. 2.10.

---

<sup>2</sup>Transmission lines with identical length.



Short-Step Stub Transformer



Quarterwave Transformer

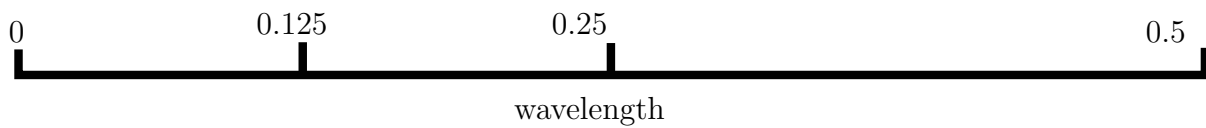


Figure 2.10: Typical transformer layouts for a 4-th order short-step and a order 2 quarter-wave transformer demonstrating the significant reduction in transmission line length for the short-step transformer of order  $2N$  compared to a classical quarter-wave transformer of order  $N$ .

All examples of circuit synthesis up to this point has only dealt with the necessity of the Hurwitz polynomial, but a method for designing a specified circuit response has been omitted. This section will introduce some transfer function approximation theory that is mostly concerned with that of lossless, doubly terminated two port filter circuits. The Chebyshev filter response is of particular interest, for which the reason will be explained later. The realisability conditions for a lossless, doubly terminated two port is given by (2.40) through (2.43). For a reciprocal two-port

$$S_{12} = S_{21} \quad (2.75)$$

and clearly  $S_{11}$ ,  $S_{12} = S_{21}$ , and  $S_{22}$  all have the same poles and therefore the same denominator. For continuity, from (2.45) the S-parameters may be written in rational form

$$S_{11} = \frac{F(s)}{E(s)}, \quad S_{21} = \frac{P(s)}{E(s)}. \quad (2.76)$$

From (2.40) it follows that

$$\frac{F(s)F(-s)}{E(s)E(-s)} + \frac{P(s)P(-s)}{E(s)E(-s)} = 1. \quad (2.77)$$

This equality is known as the Feldtkeller equation [16] and has a central role in the design of doubly terminated two-ports. For a form more convenient for numerical calculations (2.77) may be rewritten as

$$F(s)F(-s) + P(s)P(-s) = E(s)E(-s) \quad (2.78)$$

From the definition of (2.30) and (2.78)  $S_{21}S_{21}^*$  is written

$$\begin{aligned} S_{21}S_{21}^* &= \frac{P(s)P(-s)}{E(s)E(-s)} \\ &= \frac{P(s)P(-s)}{F(s)F(-s) + P(s)P(-s)} \\ &= \frac{1}{1 + \frac{F(s)F(-s)}{P(s)P(-s)}} \\ &= \frac{1}{1 + K(s)K(-s)} \end{aligned} \quad (2.79)$$

The function  $K$  is known as the characteristic function and is important in the construction of transfer functions for filters that realise a given magnitude response [16]. Since  $K(j\omega)K(-j\omega)$  is always positive it follows that

$$|S_{21}(j\omega)|^2 \leq 1 \quad (2.80)$$

which is constructed with a rational function with a magnitude larger than zero.  $|K|^2$  gives the ratio of the reflected and transmitted powers and is defined as

$$|K|^2 = \frac{|S_{11}|^2}{|S_{21}|^2} = \frac{F(s)E(s)}{E(s)P(s)} = \frac{F(s)}{P(s)}. \quad (2.81)$$

Let  $\rho = S_{11}$  be the reflection coefficient and  $|H|^2$

$$|H|^2 = \frac{1}{|S_{21}|^2} \quad (2.82)$$

$H(s)$  is therefore the transducer function and represents a ratio of input power to output power. With the definition of  $H(s)$  above, the characteristic function can be written in the form,

$$K(s) = S_{11}H(s) = \frac{F(s)E(s)}{E(s)P(s)} = \frac{F(s)}{P(s)}, \quad (2.83)$$

which is useful for extracting  $ABCD$  parameters. Realizability conditions for a doubly terminated, lossless, passive network may now be obtained in terms of  $H$  and  $E$ ,  $P$  and  $F$ . The conditions are summarised as follows [16]

- $H(s)$  may be written as  $H(s) = \frac{E(s)}{P(s)}$ , where  $E(s)$  and  $P(s)$  are polynomials with real coefficients.
- $E(s)$  is a strictly Hurwitz polynomial.
- $P(s)$  is a purely even or odd polynomial unless common factors of  $E(s)$  and  $P(s)$  cancel in  $H(s)$ .
- The modulus of  $H(s)$  satisfies  $|H(s)| \geq 1$  on the imaginary axis.
- The degree of  $E(s)$  is greater than or equal to that of  $P(s)$ .

Not only have all the realizability conditions been established for the S-parameters, but all the parameters of the two port network have now been identified. In particular the ABCD transmission parameters are now readily available which is especially convenient

for cascade synthesis. From (2.24) and the Feldtkeller equality in (2.77) it can be shown that [23]

$$H(s) = \frac{(AR_2 + DR_1) + (B + CR_1R_2)}{2\sqrt{R_1R_2}}. \quad (2.84)$$

The even and odd parts of  $H(s)$  are evidently

$$H_e(s) = \frac{AR_2 + DR_1}{2\sqrt{R_1R_2}} \quad (2.85)$$

$$H_o(s) = \frac{B + CR_1R_2}{2\sqrt{R_1R_2}}. \quad (2.86)$$

The same procedure is followed to show that

$$K(s) = \frac{(AR_2 - DR_1) + (B - CR_1R_2)}{2\sqrt{R_1R_2}} \quad (2.87)$$

with its even and odd parts given by

$$K_e(s) = \frac{AR_2 - DR_1}{2\sqrt{R_1R_2}} \quad (2.88)$$

$$K_o(s) = \frac{B - CR_1R_2}{2\sqrt{R_1R_2}}. \quad (2.89)$$

Equations (2.85), (2.86), (2.88) and (2.89) are solved to give

$$\begin{bmatrix} A & B \\ C & D \end{bmatrix} = \frac{1}{\sqrt{R_1R_2}} \begin{bmatrix} (H_e + K_e)R_2 & (H_o + K_o) \\ (H_o - K_o)R_1R_2 & (H_e - K_e)R_1 \end{bmatrix}. \quad (2.90)$$

It can be shown that by expanding the squared terms of (2.84) and (2.87) that

$$H(s)H(-s) - K(s)K(-s) = AD - BC = 1 \quad (2.91)$$

which was also shown in Section 2.1. This is the fundamental design equation.

### 2.3.1 The Chebyshev approximation for a short-step-stub transformer

The previous sections discussed the theory involved with realizable transducer functions. It is now possible to develop the transfer function for a short-step-stub Chebyshev impedance transformer. A perfect filter would have a zero reflection coefficient in the passband of the the design, with infinite attenuation in the stop band, and a linear phase response that minimize signal distortion in the passband. In practice this is not possible but a close approximation to the desired response may be obtained by the appropriate transformation of the transfer function. Some well-known filter responses include the binomial transformer, which has a maximally flat response in the passband. Contrary to the binomial transformer, the Chebyshev matching transformer is ideal for optimizing the bandwidth of a response at the cost of insertion loss performance in the passband. The compromise on the performance of the reflection coefficient in the passband leads to a substantially improved bandwidth in comparison to the binomial transformer. The Chebyshev transformer is designed by equating the insertion loss function  $S_{11}$ , to a Chebyshev polynomial, which has the optimum characteristics for this type of filter [18]. The

passband response is one of the important aspects of the short step filter, and another is the significant reduction in size relative to classical quarter wave transformers while offering comparable bandwidth.

The Chebyshev transfer function is derived by transforming a suitable  $s$ -plane response to the  $p$ -plane using Richard's transformation. This transformation is used to convert lumped elements to transmission line sections, such as open-circuited or short-circuited transmission line stubs at microwave frequencies [18]. The  $p$ -plane bandpass response is then transformed to the  $z$ -plane where a Chebyshev general parameter characteristic function is found. This function is then transformed back to the  $p$ -plane where the transfer function of the transformer is synthesized [2].

For a short-step impedance transformer the relative bandwidth for which  $S_{11} \leq S_{\max}$ , where  $S_{\max}$  is the maximum ripple of the reflection coefficient in the passband, is defined by

$$B = \frac{\omega_2 - \omega_1}{\omega_m}. \quad (2.92)$$

The frequencies  $\omega_1$  and  $\omega_2$  are the respective lower and upper boundaries of the passband and  $\omega_m$  is the center frequency of the response and is defined by

$$\omega_m = \frac{\omega_2 - \omega_1}{2}. \quad (2.93)$$

The transformer is designed with transmission lines with an electrical length equal to a quarter wavelength of the frequency  $\omega_0$ . The length of the commensurate transmission lines used in the transformer is determined by

$$t = \frac{\omega_0}{\omega_m} \quad (2.94)$$

where  $t$  is the ratio between the quarter wavelength frequency  $\omega_0$  and the response center frequency  $\omega_m$  and must satisfy  $t > (1+B/2)$ . The response is transformed to the Richard's domain by the transformation

$$p = u + jv = \tanh(sT) = \tanh\left(\frac{s\pi}{2\omega_0}\right). \quad (2.95)$$

Here  $p$  is the Richard's variable and  $s = \phi + j\omega$  is the Laplace variable.  $T$  is the delay time of the lines. In the  $p$ -plane the frequencies are given by

$$v_{1,2} = \tan\left[\left(1 \pm \frac{B}{2}\right) \frac{\pi}{2t}\right] \quad (2.96)$$

$$v_m = \tan\left(\frac{\pi}{2t}\right). \quad (2.97)$$

An even-order  $n$  impedance transformer with  $r$  open-circuit stubs and  $(n-r)$  unit elements should have  $r$  transmission zeros at  $p \rightarrow \infty$ , corresponding to the  $r$  open-circuit stubs and  $(n-r)$  transmission zeros at  $p^2 = 1$ , corresponding to the  $(n-r)$  unit elements. The characteristic function, with Chebyshev equiripple insertion loss in the passband and poles located at the frequencies of the transmission zeros, is found by transforming the  $p$ -plane response to the  $z$ -plane with the transformation [23] [24]

$$z^2 = \frac{p^2 + v_2^2}{p^2 + V_1^2}. \quad (2.98)$$

The Chebyshev general parameter function in the  $z$ -plane is [16] [24]

$$F(z)F(-z) = \frac{[P(z) + P(-z)]^2}{4P(z)P(-z)} \quad (2.99)$$

and the polynomial  $P(z)$  is given by

$$P(z) = (1+z)^r \left( \sqrt{\frac{1+v_2^2}{1+v_1^2}} + z \right)^{n-r}. \quad (2.100)$$

From (2.100) the transmission zeros at  $p \rightarrow \infty$  and  $p^2 = 1$  are clearly encapsulated in the two factors. The function  $F(z)F(-z)$  is transformed back to the  $p$ -plane to find the required transmission coefficient in a form suitable for synthesis

$$|S_{21}|^2 = \frac{1}{1 + k^2 F(z)F(-z)}. \quad (2.101)$$

The number of open-circuit stubs  $r = 0$ ,  $r = n/2$ , and  $r = n$  have simple closed-form solutions for poles and zeros of (2.101).

### 2.3.2 Matching performance of the short-step transformer

In his paper [2] Van Der Walt also provides the matching performance for a short-step transformer which shows excellent results in comparison to classical quarter wave transformers. Evaluating the characteristic function at  $s = 0$ , which corresponds to  $p = 0$  and consequently  $z = z_0 = \pm \frac{v_2}{v_1}$ , yields the maximum voltage standing-wave ratio. No impedance transformation takes place at this frequency which means that the reflection coefficient may be determined by the ratio of the terminating resistances of the transformer, which is a convenient property.

The importance of the Feldtkeller equation is again apparent when applying the identity of (2.77) for a lossless network:

$$\begin{aligned} |S_{11}|^2 + |S_{21}|^2 &= 1 \\ |S_{11}|^2 &= 1 - \frac{1}{1 + k^2 F(z)F(-z)} \\ &= \frac{kK_0}{\sqrt{1 + k^2 K_0^2}} = \left| \frac{R_2 - R_1}{R_2 + R_1} \right| \end{aligned} \quad (2.102)$$

where

$$K_0^2 = F(z_0)F(-z_0). \quad (2.103)$$

Given a relative bandwidth  $B$ , order  $n$  and resistance ratio  $R = \frac{R_2}{R_1}$ , (2.102) may be solved for  $k$  which leads to

$$k^2 = \frac{(R-1)^2}{4RK_0^2}. \quad (2.104)$$

The maximum passband ripple for the transformer response is

$$L_m = 10 \log_{10}(1 + k^2) \quad (2.105)$$



which in decibels (dB) is a reflection coefficient of

$$S_{11} = 10 \log_{10}(k^2) \text{ dB} \quad (2.106)$$

and the maximum passband voltage standing-wave ratio is given by

$$\text{VSWR} = (\sqrt{1+k^2} + k)^2. \quad (2.107)$$

The performance of the passband is determined by the value  $K_0$ , the constant term in  $|S_{21}|_{z=z_0}^2$ .

### 2.3.3 Synthesis and Element Extraction

Element values are extracted by using a procedure similar to those given in the previous sections, but is extended to distributed networks by utilising the Richard's transform and Kuroda's identities [18]. From the transducer function in (2.101) the transmission parameters, (ABCD) for the transformer is found by the parameter identification from (2.90) and (2.84) through (2.89). The inverse transmission parameter matrices for a general open-circuit shunt stub and a unit element respectively, are also determined and form the basic sections from which the transformer is assembled. Fig. 2.12 displays these sections in cascade. The ABCD matrix of a length  $l$  of a transmission line with characteristic impedance  $Z_1$  is given by

$$\begin{bmatrix} A & B \\ C & D \end{bmatrix} = \begin{bmatrix} \cos \beta l & jZ_1 \sin \beta l \\ \frac{j}{Z_1} \sin \beta l & \cos \beta l \end{bmatrix} = \frac{1}{\sqrt{1+p^2}} \begin{bmatrix} 1 & pZ_1 \\ \frac{p}{Z_1} & 1 \end{bmatrix} \quad (2.108)$$

where  $p = j \tan \beta l$ . The open-circuit stub of length  $l$  and characteristic impedance  $Z_2$  has a transmission matrix given by [18]

$$\begin{bmatrix} A & B \\ C & D \end{bmatrix} = \begin{bmatrix} 1 & 0 \\ \frac{p}{Z_2} & 1 \end{bmatrix}. \quad (2.109)$$

The inverse transmission matrices for a unit element and a shunt open-circuit stub is given by

$$\frac{1}{\sqrt{1+p^2}} \begin{bmatrix} 1 & pZ_1 \\ \frac{p}{Z_1} & 1 \end{bmatrix}^{-1} = \frac{1}{\sqrt{1+p^2}} \begin{bmatrix} 1 & -pZ_1 \\ \frac{-p}{Z_1} & 1 \end{bmatrix} \quad (2.110)$$

and

$$\begin{bmatrix} 1 & 0 \\ \frac{p}{Z_2} & 1 \end{bmatrix}^{-1} = \begin{bmatrix} 1 & 0 \\ \frac{-p}{Z_2} & 1 \end{bmatrix}, \quad (2.111)$$

where it will prove more useful to express (2.111) by its characteristic admittance

$$\begin{bmatrix} 1 & 0 \\ pY_2 & 1 \end{bmatrix}^{-1} = \begin{bmatrix} 1 & 0 \\ -pY_2 & 1 \end{bmatrix}. \quad (2.112)$$

The synthesis is done by examination of the poles of the transmission parameters of the transformer to establish what types of circuit sections may be extracted. A section is then extracted from left or right, by pre-multiplication or post-multiplication of the transformer's transmission matrix by the inverse matrix of the section to be extracted.

The characteristic impedance of the section extracted is calculated such that the resulting matrix has a reduced order due to either pole cancellation of the parameters or by cancellation of the coefficients of highest or lowest order term of the numerators. This procedure is followed repeatedly until the order of the transmission matrix is reduced to zero with only an ideal transformer remaining. The order of two parameters are reduced at each step in the synthesis procedure and numerical accuracy is verified by ensuring that the order of each parameter is reduced simultaneously [2]. Traditionally the topic of numerical accuracy has always had to accompany the synthesis of filters, as a high degree significant digits are required to accommodate for the sensitivity of frequency dependent circuits. Lind [25] investigates methods that provide the highest degree of accuracy with particular relevance to cascade synthesis. These methods are incorporated in the numerical calculations of all transformer designs throughout this thesis.

### 2.3.4 Design Example

To serve as an example, the design of a fourth-order short-step stub Chebyshev impedance transformer is presented using (2.92) through (2.107). It is constructed with commensurate  $\frac{\lambda}{12}$  lines ( $t = 3$ ), with a relative bandwidth of 20%, and a transformer ratio  $R = 5$ .

From (2.96) the lower- and upper-bound frequencies, in radians, are

$$\begin{aligned} v_1 &= 0.5095 \\ v_2 &= 0.6494. \end{aligned} \tag{2.113}$$

The construction of the transducer function then begins by a  $z$ -plane transformation with  $v_1$  and  $v_2$  and the  $z$ -plane transformation according to (2.98). The polynomial  $P$  is constructed with (2.100) by substitution of (2.98) and  $v_1$  and  $v_2$

$$\begin{aligned} P(z) &= (1+z)^2 \left( \sqrt{\frac{1+v_2^2}{1+v_1^2}} + z \right)^2 \\ &= \frac{z^4 + 4.1248z^3 + 6.3783z^2 + 4.3822z + 1.1287}{z^4 - 4.1248z^3 + 6.3783z^2 - 4.3822z + 1.1287} \end{aligned} \tag{2.114}$$

from which  $F(z)F(-z)$  is found by substituting  $P(z)$  into (2.99)

$$F(z)F(-z) = \frac{z^8 + 12.7566z^6 + 42.9403z^4 + 14.3984z^2 + 1.2739}{z^8 - 4.2574z^6 + 6.78877z^4 - 4.8053z^2 + 1.2739}. \tag{2.115}$$

The characteristic function is found by converting back to the  $p$ -plane and evaluating  $F(p)F(-p)$  which is further simplified by dividing through with the denominator's highest order coefficient

$$F(p)F(-p) = \frac{166244.95p^8 + 225725.34p^6 + 113840.88p^4 + 25267.82p^2 + 2083.16}{\sqrt{1-p^2}}. \tag{2.116}$$

The performance parameters  $K_0^2$  and  $k^2$  are found by evaluating  $F(p)F(-p)$  at  $p = 0$ . Here no impedance transformation takes place and (2.103) through (2.107) holds true and

gives

$$\begin{aligned} K_0^2 &= 2083.2 \\ k^2 &= 0.00038403 \\ L_m &= 0.0016675 \text{ dB} \\ \text{VSWR} &= 1.040 \end{aligned} \tag{2.117}$$

and the maximum value of the reflection coefficient in the passband is  $-34.1563 \text{ dB}$ . With the value of  $k^2$  known, the function for  $|S_{21}|^2$  from (2.102) may be constructed in a form suitable for synthesis as the transmission parameter can be found from the transmission zeros at  $p \rightarrow \infty$  and  $p^2 = 0$ . The transmission parameters of  $H(p)$  are found numerically by calculating its roots. The roots are shown in Fig. 2.11.

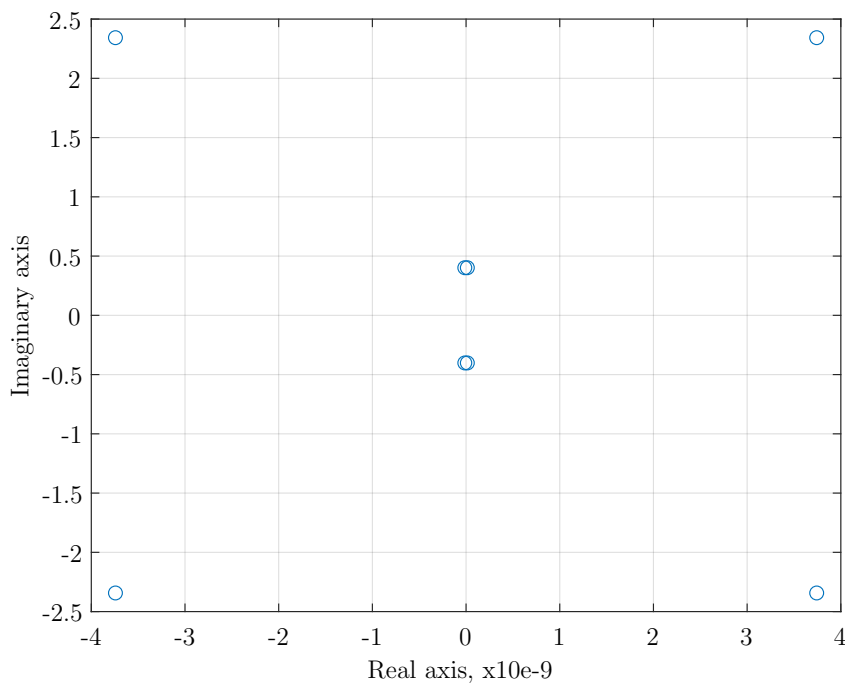


Figure 2.11: Transmission zeros of  $H(p)H(-p)$ . The Transmission zeros for  $H(p)$  are located in the LHP.

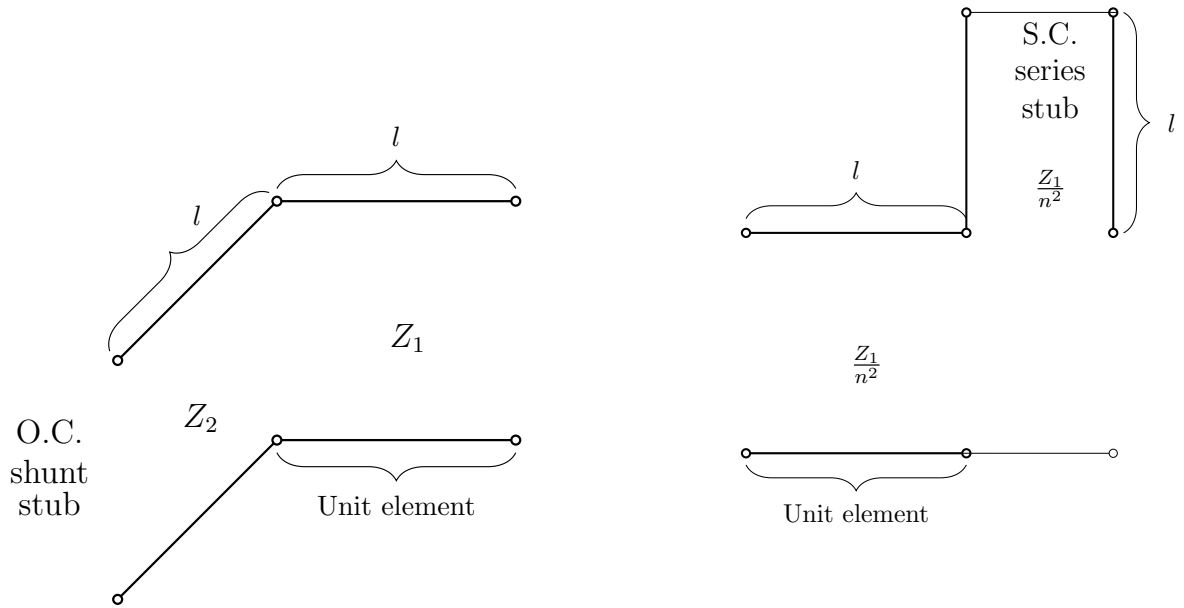
There are four transmission zeros in the LHP corresponding to  $H(p)$  and four in the RHP from  $H(-p)$ . Note the transmission zeros occur in conjugate pairs and lie symmetrically around the imaginary axis as well as the real axis. Two of the conjugate pairs lie close together around the zero vertical on real axis and are almost indistinguishable.

The transmission matrix is calculated from  $H(p)$  and  $K(p)$  with (2.90) and gives

$$\begin{bmatrix} A & B \\ C & D \end{bmatrix} = \frac{1}{1-p^2} \begin{bmatrix} 2.2361 + 15.117p^2 + 15.980p^4 & 4.2783p + 8.2586p^3 \\ 4.2783p + 8.2586p^3 & 0.4472 + 4.2680p^2 \end{bmatrix}. \tag{2.118}$$

The  $ABCD$  parameters have two common factors  $\sqrt{1-p^2}$  in their denominators that imply that unit elements can be extracted from any port. The parameter  $A$ , which was identified in Fig. 2.3a and in (2.20) as the inverse open-circuit voltage ratio of the impedance

transformer, has one more transmission zero than parameters  $B$  and  $C$  and two more than parameter  $D$  implying a parallel open-circuit shunt stub at port 2 and a series short-circuit stub at port 1 [2]. Fig. 2.12 displays one of the Kuroda identities [18] and this shows that a series short-circuit stub cascaded with a unit element is equivalent to a unit element cascaded with a shunt open-circuit stub. It is therefore possible to construct a network with the same topology as the short-step stub transformer from Fig. 2.10.



(a) Open-circuit shunt stub cascaded with a unit element.

(b) Short-circuit series stub cascaded with a unit element.

Figure 2.12: Kuroda identity displaying equivalent circuits of a unit element with a parallel, open-circuit stub and a unit element with a series, short-circuited stub.

A unit element is extracted from the left side of the impedance transformer by pre-multiplying the transmission matrix by the inverse  $ABCD$  matrix of a unit element given in (2.110). The result is of the form

$$(1 - p^2)^{-1} \begin{bmatrix} A' & B' \\ C' & D' \end{bmatrix} = (1 - p^2)^{-1} \begin{bmatrix} A - \frac{pB}{Z_1} & B - pZ_1A \\ C - \frac{pD}{Z_1} & D - pZ_1C \end{bmatrix}. \quad (2.119)$$

For a reduction in the order, the factor  $(1 - p^2)$  has to cancel a similar factor in the numerators of the parameters. In order to create transmission zeros at  $p^2 = 1$  in the numerators, the unit element that is extracted requires a characteristic impedance  $Z_1 = \frac{B(p^2=1)}{A(p^2=1)} = \frac{D(p^2=1)}{C(p^2=1)}$ . The extraction will only be possible if both conditions for  $Z_1$  hold. The extraction from  $A(1)$  yields an unit element with a characteristic impedance of  $Z_1 = 2.5688 \Omega$ . The resultant matrix is

$$\frac{1}{1 - p^2} \begin{bmatrix} 2.2361 + 5.9777p^2 & 3.0893p \\ 3.4373p + 6.0103p^3 & 0.4472 + 3.1061p^2 \end{bmatrix}. \quad (2.120)$$

From (2.120) an open-circuit shunt stub may be extracted from  $C$  which is the inverse open-circuit transfer impedance. It has two transmission zeros at infinity, while parameter

$B$ , which is the inverse short-circuit transfer admittance, has none. An extraction from the left side is done by pre-multiplying the transmission matrix from (2.120) with the inverse admittance matrix (2.112) of an open-circuit shunt stub with a characteristic admittance  $Y_2$ . The extraction leaves a matrix of the form

$$\begin{bmatrix} A' & B' \\ C' & D' \end{bmatrix} = \begin{bmatrix} A & B \\ C - pY_2A & D - pY_2B \end{bmatrix}. \quad (2.121)$$

A transmission zero at infinity is removed by cancellation of the highest order coefficients in  $C'$  and  $D'$ , thereby reducing the order of the matrix. Therefore

$$Y_2 = \lim_{p \rightarrow \infty} \left[ \frac{C}{pA} \right] = \lim_{p \rightarrow \infty} \left[ \frac{D}{pB} \right]. \quad (2.122)$$

A shunt stub with characteristic admittance  $Y_2 = 1.0055 \text{ S}$  is extracted and leaves

$$\frac{1}{\sqrt{1-p^2}} \begin{bmatrix} 2.2361 + 5.9777p^2 & 3.0893p \\ 1.18907p & 0.4472 \end{bmatrix}. \quad (2.123)$$

Another unit element with characteristic impedance  $Z_3 = 6.9077 \Omega$  is extracted from the left side following the same procedure as before and then another shunt stub with characteristic admittance  $Y_4 = 0.3870 \text{ S}$  is extracted from the left side in the same way as  $Y_2$  was extracted. The transmission matrix order is reduced until only an ideal transform remains given by

$$\begin{bmatrix} 2.2361 & 0 \\ 0 & 0.4472 \end{bmatrix}. \quad (2.124)$$

The transformer turns ratio is  $2.2361 : 1$  which transforms a normalized port impedance of  $1 \Omega$  to the specified  $5 \Omega$  port impedance. With the synthesis completed the normalized extracted element values can be scaled to match practical port impedances. Fig. 2.13 shows the response of the fourth-order short-step stub Chebyshev impedance transformer, scaled to match a  $50 \Omega$  port to a  $10 \Omega$  port with the lower edge of the passband frequency at  $0.9 \text{ GHz}$  and the upper edge at  $1.1 \text{ GHz}$  for a bandwidth of  $20\%$  around a center frequency  $f_c = 1 \text{ GHz}$ . The maximum value of the reflection coefficient in the passband is  $-34.16 \text{ dB}$ .

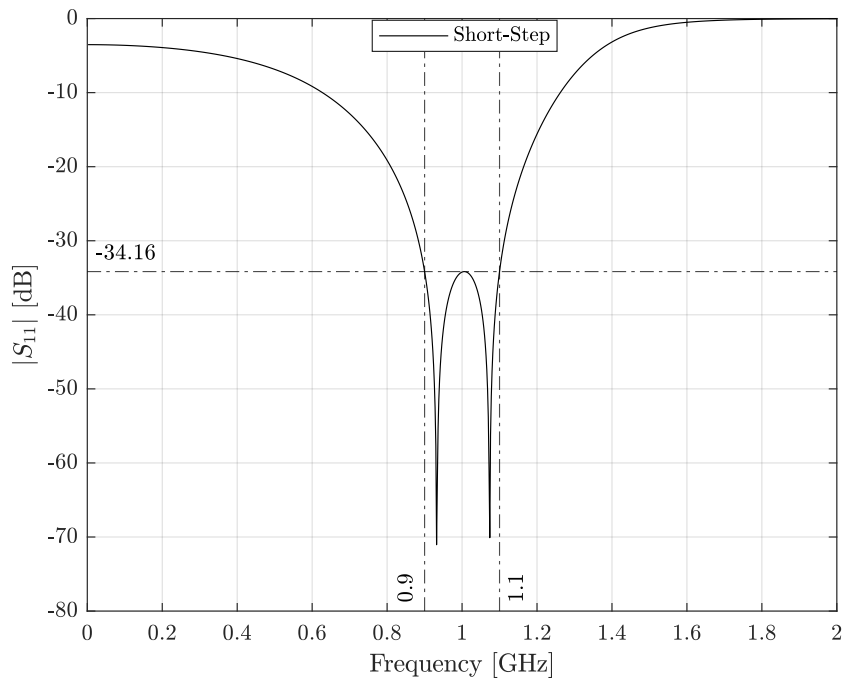


Figure 2.13:  $|S_{11}|$  Response of the short-step stub Chebyshev impedance transformer.

The circuit could easily be implemented using quasi-TEM striplines or microstriplines, however as the goal is to implement the design as a axially symmetric waveguide power combiner, Fig. 2.14 displays the implementation of the circuit in the design example using coaxial lines in AWR Microwave Office. The  $10\ \Omega$  port impedance is a representation of the combined parallel impedances, typically realized by five standard  $50\ \Omega$  ports, positioned symmetrically around the waveguide structure. These ports are referred to as the peripheral ports and their number, i.e. 5 is indicative of the transformer ratio.

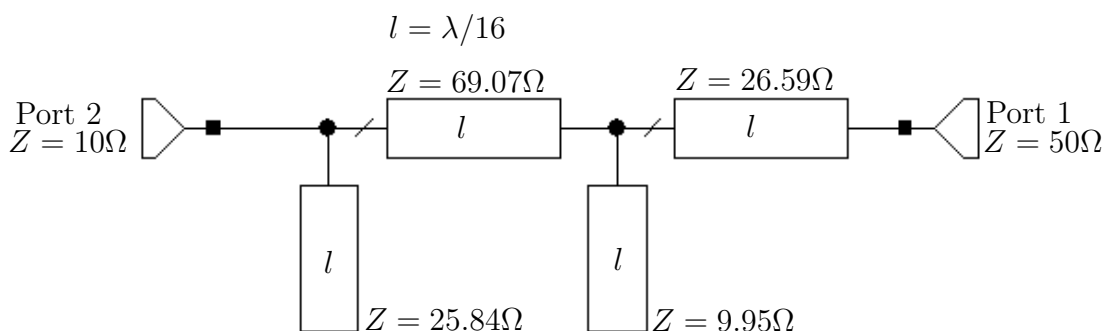


Figure 2.14: Microwave Office coaxial line implementation of the short step transformer with  $\frac{\lambda}{12}$  lines.

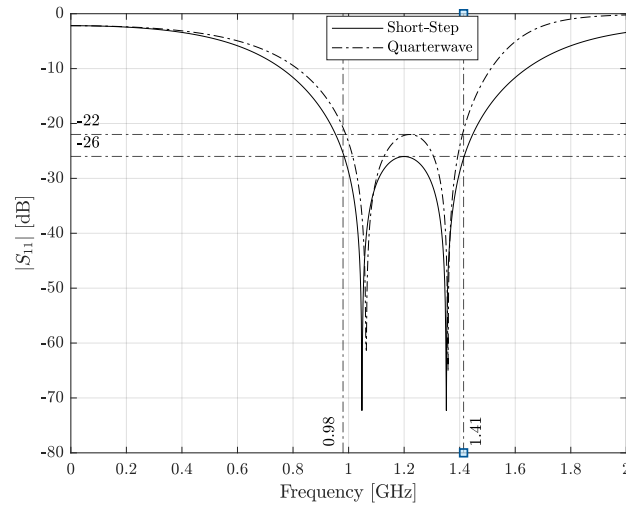
### 2.3.5 Passband Performance Comparison

Using the exact same design procedure as outlined above, a multitude of short-step transformer synthesis are possible within the constraints as given in the example above. Some

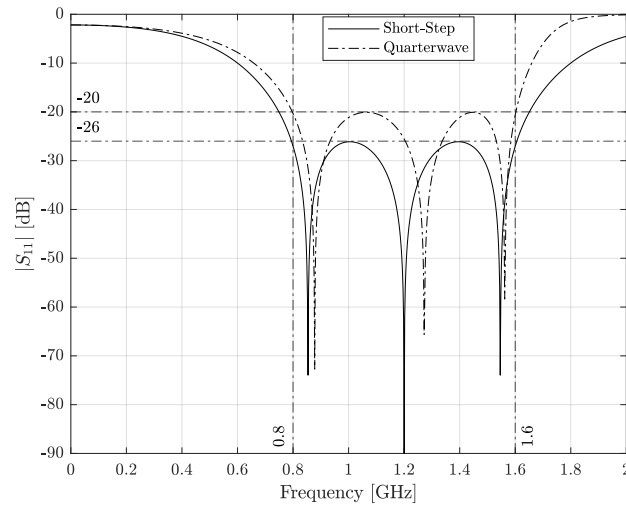
higher order design examples are shown, exhibiting significant improvement in the pass-band performance in terms of the bandwidth and reflection coefficients, at the cost of a larger circuit.

Type	order N	Bandwidth	$ S_{11} $ dB	Total length
Quarter-wave	2	0.35	-26	$0.5\lambda$
Short-step $\frac{\lambda}{16}$	4	0.35	-22	$0.125\lambda$
Quarter-wave	3	0.67	-26	$0.75\lambda$
Short-step $\frac{\lambda}{16}$	6	0.67	-20	$0.25\lambda$
Quarter-wave	4	0.35	-27	$\lambda$
Short-step $\frac{\lambda}{16}$	8	0.35	-19	$0.375\lambda$

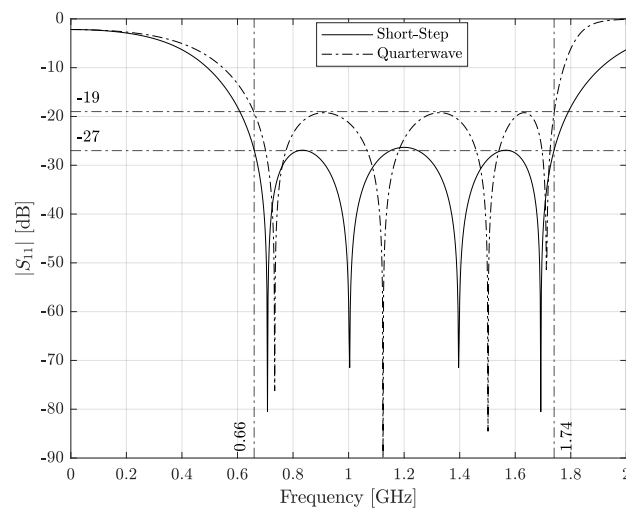
Table 2.1: Passband performance comparison of quarter-wave vs. short-step Chebyshev transformers.



(a) 2nd order quarter-wave- vs. 4th order short-step transformer.



(b) 3rd order quarter wave- vs. 6th order short-step transformer.



(c) 4th order quarter-wave- vs. 8th order short-step transformer.

Figure 2.15: Passband performance comparison between  $N$ -th order quarter-wave, Chebyshev impedance transformer vs  $2N$ -th order short-step Chebyshev transformers.



Table 2.1 and Fig. 2.15 show a comparison between the passband performance of a quarter-wave Chebyshev impedance matching transformer of order  $N$ , and a Chebyshev short-step impedance matching transformer of order  $2N$ . The trade-off between the compromise in passband ripple performance for comparable bandwidth and significant reduction in the overall size is clear for the short-step transformer. It is also noted that the short-step is required to be of an order double that of the quarter-wave implementation to become comparable, and as a rule, higher order implementation become more sensitive to deviations in element values [24], resulting in a higher complexity in realizing the circuit.

### 2.3.6 Summary

This section has provided a thorough discussion along with examples and performance comparisons for the synthesis of short-step stub Chebyshev impedance transformers. In comparison to a traditional quarter-wave Chebyshev matching transformer, the short-step transformer makes up for what it lacks in passband ripple by providing a solution that compares very well in terms of bandwidth, but offers significant reductions in overall physical dimensions. Short-step transformers of order  $2n$  have bandwidths equal to quarter-wave transformers of order  $n$  whilst being only a quarter of the length. The transformers also offer flexible design constraints that allow for a wide range of suitable circuits to be designed which may provide acceptable passband ripples at the cost of decreasing the bandwidth.

## 2.4 Conclusion

The necessary theory of analysis and realizability requirements that form the foundation for the synthesis procedures has been presented. The scope was limited to that of passive, lossless two-ports and its applicability to N-ports, such as coaxial power combining structures, were pointed out. The synthesis methodology enables the compact design of circuits, that if implemented within coaxial combiners can greatly reduce the overall physical dimensions of such structures, especially those operating at lower frequencies, where size considerations are extremely important. The chapter also provided examples in each section by which the conveying of the design procedure is solidified. Table 2.1 summarises the benefit of short-step transformer circuits over quarter-wave matching sections in terms of physical dimensions whilst displaying excellent bandwidth comparison. The design example adapted from [2] lays the foundation of the design of the coaxial combining structure in the following chapter.

In summary, the discussion points of focus for this chapter are:

1. The presentation of circuit analysis techniques that are prerequisites to circuit synthesis.
2. The realizability conditions and circuit types used for developing practical, realizable circuits using a minimum number of elements, and the transfer design for a required response.
3. The design procedures for a Chebyshev short-step stub impedance transformer realization that form the foundation for designing compact coaxial impedance transforming structures that offer the desired bandwidth, with acceptable passband reflection coefficients whilst significantly reducing overall circuit size.

## Chapter 3

# Compact N-Way Coaxial Waveguide Combiners

The short-step filter designs from Chapter 2 are highly susceptible to performance degradations when implemented as distributed circuits, partly due the fact that the poles and zeros of the transfer function rely on resonant structures of which the combination of  $L$  and  $C$  values are unique and because distributed circuits are sensitive to numerous factors that make wave mode propagation unsymmetrical. For this reason uniform TEM coaxial lines are ideally suited for the purpose of realizing the unit elements of a short-step transformer as they offer constant line impedance with radial distance. The symmetry of coaxial lines also have greater benefits than traditional T-junction and Wilkinson power combiners, which are resistive in nature, thus incurring undesired power losses and are bulky when extended to N-way combiners [18]. The advantages of aforementioned traditional power combiners are, that they are easier to match and isolate the input ports. The focus of this chapter is the design of lossless combiners, which rely on external circuitry and a large number of combining ports for adequate isolation.

This chapter discusses the methods for implementing a short-step stub Chebyshev impedance transformer as a coaxial combining structure, and it also addresses a particular practical difficulty that arises when trying to implement a short-step transformer as it was synthesized in Chapter 2. An approach for implementing the shunt elements are discussed and analysed and a few compact power combiners are synthesized and presented with design examples.

This chapter is mainly concerned with the design of a compact axially symmetric power combiner. It starts with a discussion on the design and application of waveguide power combiners, with a focus on axially symmetric structures. A general combining structure configuration and geometrical parameters are presented which is referenced throughout the chapter. A thorough discussion on design consideration with waveguide implementations covers most of the practical constraints in realising the synthesised short-step circuits from Chapter 2. The individual parts and the implementation of these are broken up into subsections and presented in a logical order that follows the design process. Towards the end of the chapter a detailed design example is given, following the same order as the sections before. The results of several designs are then presented and analysed before the concluding discussions.

### 3.1 General Parameters of a Coaxial Combiner

This section introduces some of the general parameters and terminology used with coaxial power combiners. When the circuit is reciprocal it is commonly referred to as a combiner or divider as the circuit functions as both. Fig 3.1 displays a simplified transmission line model of a  $N$ -way power combiner with transmission lines joined at a single point. Note that an  $N$ -way combiner has a total of  $N + 1$  ports. The central combining port is designated as port 1 and transmits the combined power of ports 2 to  $N + 1$  and therefore needs a connector capable of handling the high power. Ports 2 to  $N + 1$  are the  $N$  peripheral ports which are driven with equivalent phase and amplitude signals that is combined within the waveguide structure and transmitted at high power from the central port.

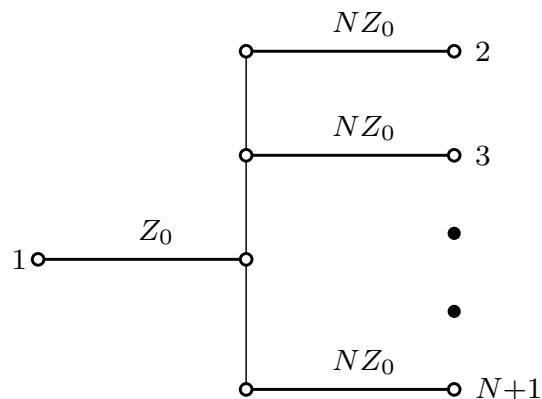


Figure 3.1: Simplified transmission line model of reactive  $N$ -way combiner. Adopted from [26].

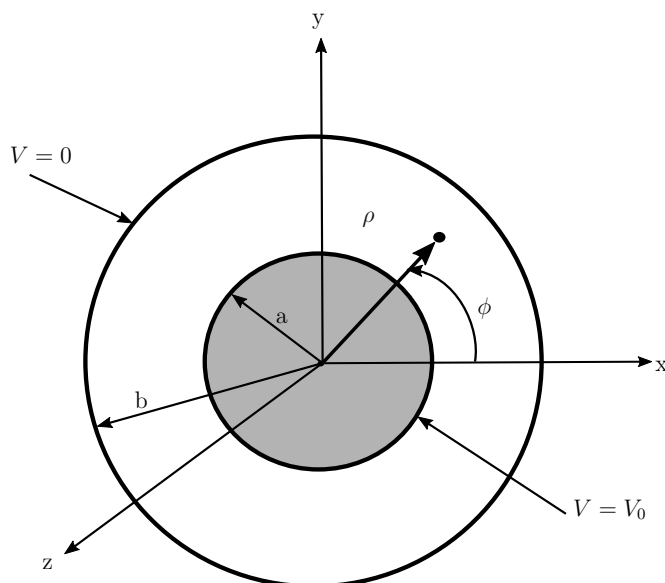


Figure 3.2: Coaxial line geometry.

The coaxial combiners used in the design within this chapter are cylindrical in shape with common spacial references depicted in Fig 3.2. It shows a cross-section of a coaxial line

with an inner conductor of radius  $a$ , an outer conductor radius  $b$  and an arbitrary point between the inner- and outer conductors at radius  $\rho$  at an angle  $\phi$  to the  $x$ -axis in the  $xy$  plane. The inner conductor is at a potential  $V_0$  where the outer conductor is usually the voltage reference point  $V = 0$ . The cylindrical structure extrudes into the positive  $z$ -direction from the central port and the entire structure is symmetrical around the  $z$ -axis.

A 2D view of a general 8-way coaxial combiner with its parameters is shown in Fig. 3.3.

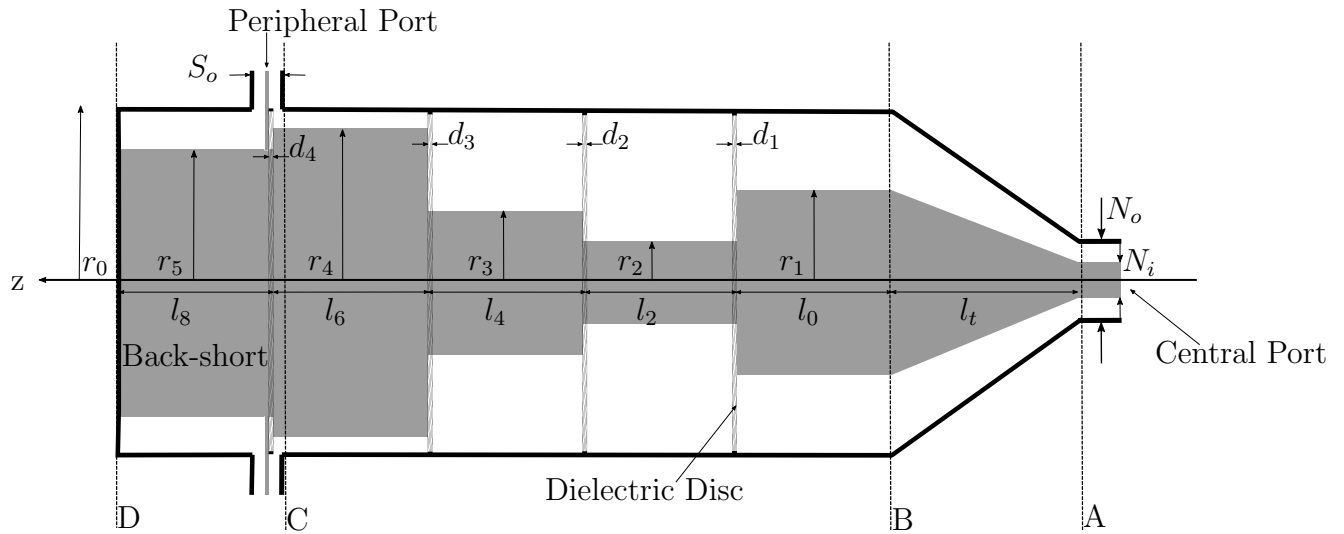


Figure 3.3: 2D cross-section of an 8-way coaxial combiner with its parameters.

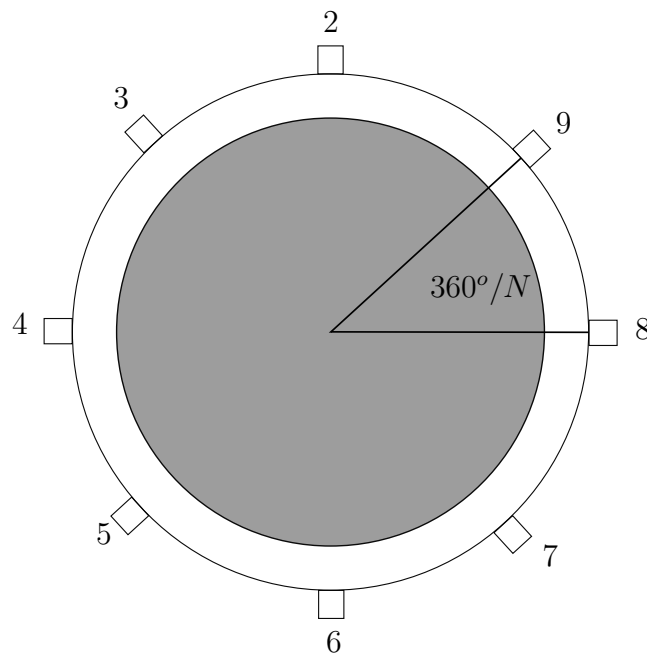


Figure 3.4:  $xy$ -Plane cross-section of the 8 peripheral ports, 2 -  $N+1$ , arranged symmetrically around the axis of the central port of an 8-way combiner.

To gain some insight into the operating theory of the combining structure it is divided into four different sections A-D by the vertical dashed lines. The coaxial peripheral ports on the oversized combining structure, section D-C, connects perpendicularly to the central coaxial waveguide which is short-circuited at a distance  $l_8$ , the back-short length, on one side of the input ports, while the other side is followed at a distance  $l_6$  from the peripheral ports by a stepped impedance coaxial line matching section C-B. A characteristic line impedance for the section of length  $l_8$  is initially approximated by including a transmission zero at  $p = 0$  in the previous synthesis, which provides an open circuit at the centre frequency when looking from the input port side to the short wall at D. The propagating mode in the central coaxial waveguide is required to be the dominant TEM mode as its axially symmetric electric field is essential for phase and amplitude balance between the individual peripheral ports. In order for the combiner to be at maximum efficiency, the ports have to be fed symmetrically to prevent the excitation of higher order modes that bring about undesired effects. The radii of the different sections are denoted by  $r_j$ , where  $j = 1, 2, \dots$ . The outer conductor radius  $r_0$  is chosen to provide sufficient circumference for accommodating the input port connectors, while also taking into account the power handling requirements and the cut-off frequency of higher order modes of propagation. The matching section comprises of two sections C-B and B-A. The C-B sections is an air-filled coaxial line with a fixed outer conductor radius with stepped impedances and etched-line dielectric discs used to implement the short-step Chebyshev impedance transformer. The transformer is responsible for matching the  $50\ \Omega$  central combining port at A to the  $50/N\ \Omega$  peripheral ports. Section B-A is a constant  $50\ \Omega$  coaxial waveguide with tapered inner- and outer conductor profile that transitions the oversized coaxial line to a standard  $50\ \Omega$  connector such as an N-type. The length  $l_t$  is the length of the tapered section along the  $z$ -axis. The dimensions  $d_i$ , where  $i = 1, 2, \dots$  are the thickness of dielectric discs used in the implementation of stub lines which is detailed in Section 3.3.1. Each design stage will reference a section denoted in Fig. 3.3.

## 3.2 Design Considerations with Waveguide Implementations

The compact short-step stub circuit designs from Chapter 2 are not as readily implemented in waveguide structures as with microstrip distributed circuit realizations. Axially symmetric waveguide combining structures typically require a back-short behind the peripheral ports of approximately a quarter wavelength shown as  $l_8$  in Fig 3.3. This is to transform the short circuit at the end of the line to an open circuit at the peripheral feeding ports. A transmission zero is introduced at the frequency where the back-short length becomes a half wavelength in pure TEM structures. Unfortunately the inclusion of a back-short complicates the synthesis procedure. This section introduces a numerical approach that forms part of the synthesis that allows for an accurate design of a short-step circuit that includes a back-short within coaxial waveguide structures.

Other difficulties in the design arise due to the reliance on symmetrical structure with TEM wave propagation. Higher order modes of propagation may occur within the waveguide structure that introduce unsymmetrical fields that bring about undesired behaviour in the system. Measures have to be taken in the initial consideration of the design parameters to allow for the physical dimensions needed to accommodate  $N$  ports, whilst taking into account the type of ports required for the peripheral ports and combining central port respectively and avoiding higher order modes of propagation. How well the ports are isolated from each other is another consideration and it partially depends on the number of ports and the spacing between them and will have an influence on the performance of the design. This is an important factor in the overall system design as graceful degradation allows the system to function even in the presence of individual failures.

Another important deliberation is the power capacity of the circuit. There is a trade-off to be made between the bandwidth and insertion loss of the structure versus its power handling capabilities. The power capacity is limited by voltage breakdown among other factors and larger structures have more power capacity, but as the size of the structure increases, so does the likelihood of higher order modes of propagation. This section discusses the above considerations and the relationships between them, in an attempt to mitigate any undesired results and compromises that they may incur.

### 3.2.1 Synthesis with a Back-Short Approximation

The back-short creates a direct current (DC) short circuit between the coaxial conductors, but at the operating frequency of the device it is an open circuit as the impedance looking from the peripheral ports into the back-short appears as an open-circuit to all waves within the passband. The waves entering and exiting the circuit then only travels between the central port and the peripheral ports. The back-short requires the synthesis of the circuit to include a transmission zero at  $p = 0$ . This introduces difficulties of its own as the equation from Section 2.3.2, with no impedance transformation takes place at  $p = 0$  when  $z = z_0 = \pm \frac{v_2}{v_1}$ , is no longer valid. Subsequently the primary design equation (2.102) no longer holds true and equations (2.103) through (2.107) are also forfeit. An exact synthesis is analytically still possible, by evaluating (2.102) at the center frequency of operation consequently with all subsequent design equations holding true, but the analytical process would be tedious and a numerical approximation may prove to be

cheaper in terms of computation time, without significant loss in accuracy. The synthesis from Section 2.3.1 is followed in the same way as before. The back-short is included in the synthesis by introducing a transmission zero at zero within the polynomial  $P(z)$  from (2.100).

$$P(z) = (1+z)^r \left( \sqrt{\frac{1+v_2^2}{1+v_1^2}} + z \right)^{n-r-1} \left( \pm \frac{v_2}{v_1} + z \right)^1 \quad (3.1)$$

The rest of the synthesis may be carried out exactly as in Section 2.3.1, but the desired impedance transformation will be lost. The transformer ratio is no longer equal to the impedance ratio  $R$  as before. Instead the transformer ratio is now a frequency dependent function and all element impedances have to be taken into account. Equation (2.104) may be used as an initial approximation and  $k^2$  is found by numerically adjusting the impedance ratio  $R$  such that the transformer ratio as given in (2.124) converge to the desired transformer ratio. The numerical approximation delivers satisfactory results which has excellent comparison to the analytical synthesis procedure. Fig. 3.5 displays the circuit configuration of a coaxial line implementation of a short-step transformer with a back-short. The element extractions are performed using the dual circuit. The difference is prominent when the circuit configuration from Fig. 2.14 is compared with that of Fig. 3.5. With the normal synthesis procedure as done in Section 2.3, the first element extracted from the left is a unit element, whereas with the dual circuit the first viable element extraction is a shunt open circuit. Element extraction from the dual circuit is a necessity that arises from the inclusion of a back-short.

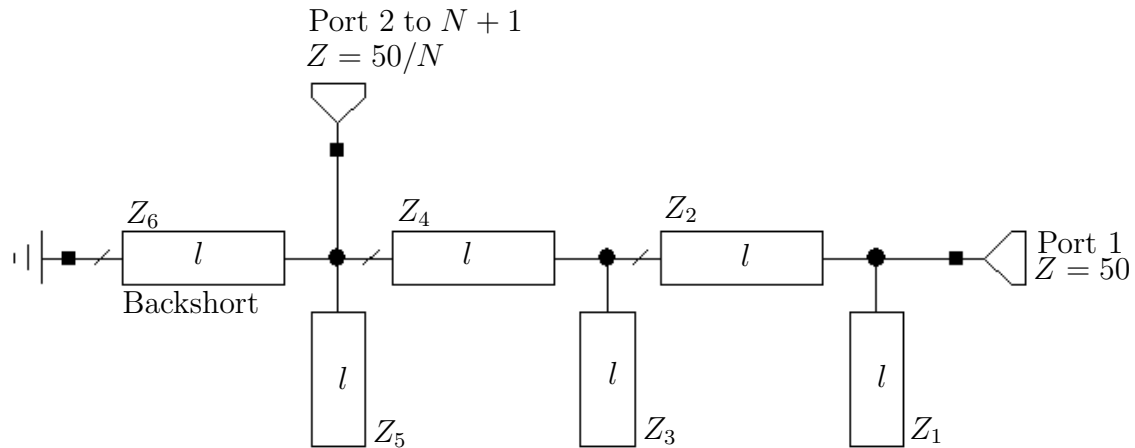
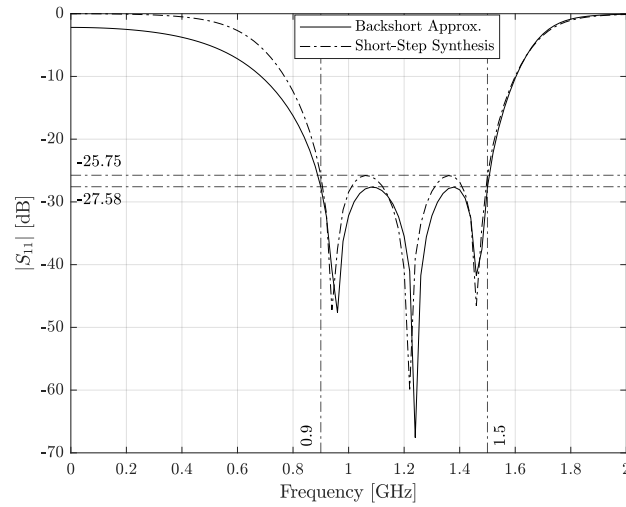
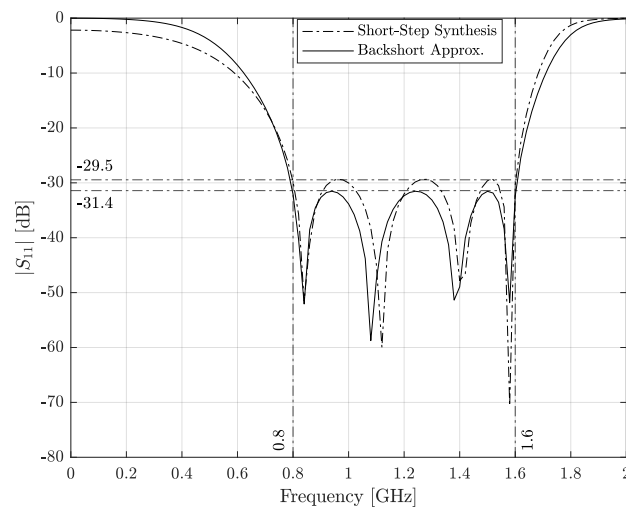


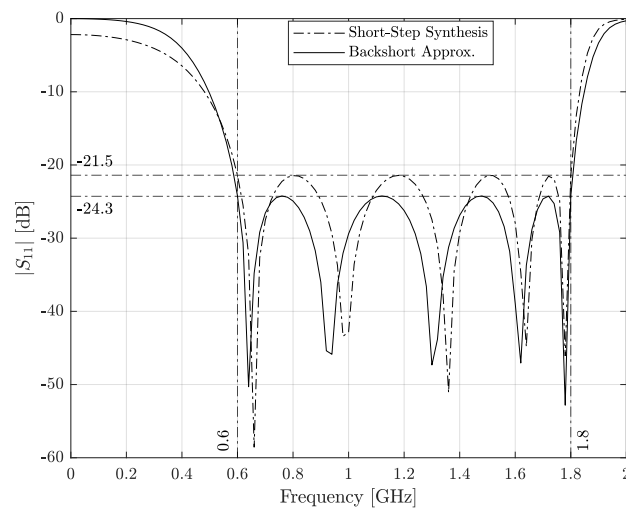
Figure 3.5: A basic configuration of the short-step transformer circuit with a back-short. The circuit is simulated in AWR MWO with coaxial transmission line elements. The element extractions are performed using the dual circuit parameters.



(a) Comparison: 6th order short-step transformer.



(b) Comparison: 8th order short-step transformer.



(c) Comparison: 10th order short-step transformer.

Figure 3.6: N-th order Chebyshev short-step impedance transformer comparison between analytical synthesis without a back-short and numerically approximated synthesis that include a back-short.



A performance comparison between the analytically synthesised short-step transformers without a back-short and numerically approximated short-step synthesis that includes a back-short is summarised in Table 3.1. The circuit responses for a 6th, 8th, and 10th order short-step transformer for each of the above mentioned circuit synthesis are shown for comparison in Fig. 3.6. Improvement in the  $S_{11}$  parameters of the circuits including a

Synthesis	order N	Relative Bandwidth	$ S_{11} $ dB	Total length
Short-step	6	0.5	-25.75	$0.1875\lambda$
Back-short	6	0.5	-27.58	$0.1875\lambda$
Short-step	8	0.67	-29.5	$0.25\lambda$
Back-short	8	0.67	-31.4	$0.25\lambda$
Short-step	10	1.0	-21.5	$0.3125\lambda$
Back-short	10	1.0	-24.3	$0.3125\lambda$

Table 3.1: Passband performance comparison of short-step synthesised filters, and filter synthesis with a numerical approximation for the inclusion of a back-short with a given transformer ratio.

back-short while retaining the specified bandwidth is demonstrated in Fig 3.6 and Table 3.1. Compared to the synthesized filters without the back-short the improvement in the reflection coefficient in the passband is an added bonus and serves to demonstrate that no compromises are made in the numerical synthesis with the back-short approximation.

### 3.2.2 Higher Order Modes

In coaxial waveguides, the fundamental mode of propagation is the TEM mode. TEM mode propagation is desirable in axially symmetrical waveguide structures, since it has a constant characteristic impedance with radial distance. This property is desirable and makes coaxial transmission lines ideally suited for incorporating the short step filters from Chapter 2. Coaxial lines can also support transverse electric (TE) and transverse magnetic (TM) waveguide modes. These modes are usually evanescent and excited at discontinuities or unsymmetrical features [27]. To gain a higher degree of insight into such behaviour, full wave simulations are necessary as the effects are mainly reactive and in close proximity to the discontinuity [28]. In practise these effects are generally undesirable but may be useful in certain aspects of the designs of this chapter. Whether or not reactive effects are required, it remains important to be aware of the cut off frequency of the lowest order modes in order to avoid propagation thereof. Some unwanted effects can occur when two or more modes propagate with different propagation constants. In designing a structure that avoids the propagation of higher order modes, an upper limit is set on the physical size of the coaxial waveguide, or seen differently, a limit on the operating frequency of the waveguide. The upper-limit on the size of the structure also imposes limits on the power handling capabilities of the coaxial combiner. Power handling is discussed in Section 3.2.3.

### Cut-Off Frequencies

The presence of higher-order wave propagation modes makes it difficult to find accurate circuit model representations for waveguide structures when the circuit is not driven symmetrically, and especially with the difference in the physical separation of the peripheral ports. It is important to know the cut-off frequency of the dominant higher order mode in the initial design consideration as it will place limitations on the maximum amount of peripheral ports that can be placed on the combining structure. In coaxial lines the dominant waveguide mode is the  $TE_{11}$  mode and is of primary importance in a coaxial combiner design that avoids higher order modes. From [18] Maxwell's equations are applied together with the boundary conditions of a coaxial waveguide that results in a transcendental equation which must be solved numerically for the cut-off wave number to find an approximated solution of

$$k_c = \frac{2}{a+b} \quad (3.2)$$

where  $k_c$  is the cut-off wave number, and  $a$  and  $b$  is, as shown in Fig. 3.2, the respective inner and outer radii of the coaxial line. Fig 3.7 displays the numerically approximated cut-off wave number for various ratios of  $b/a$  and may be used to estimate the cut-off frequency of the dominating  $TE_{11}$  mode for a given coaxial line by using the formula

$$f_c = \frac{k_c}{2\pi\sqrt{\mu\epsilon}} \quad (3.3)$$

where  $\mu$  is the magnetic permeability and  $\epsilon$  is the electric permittivity of the insulating medium.

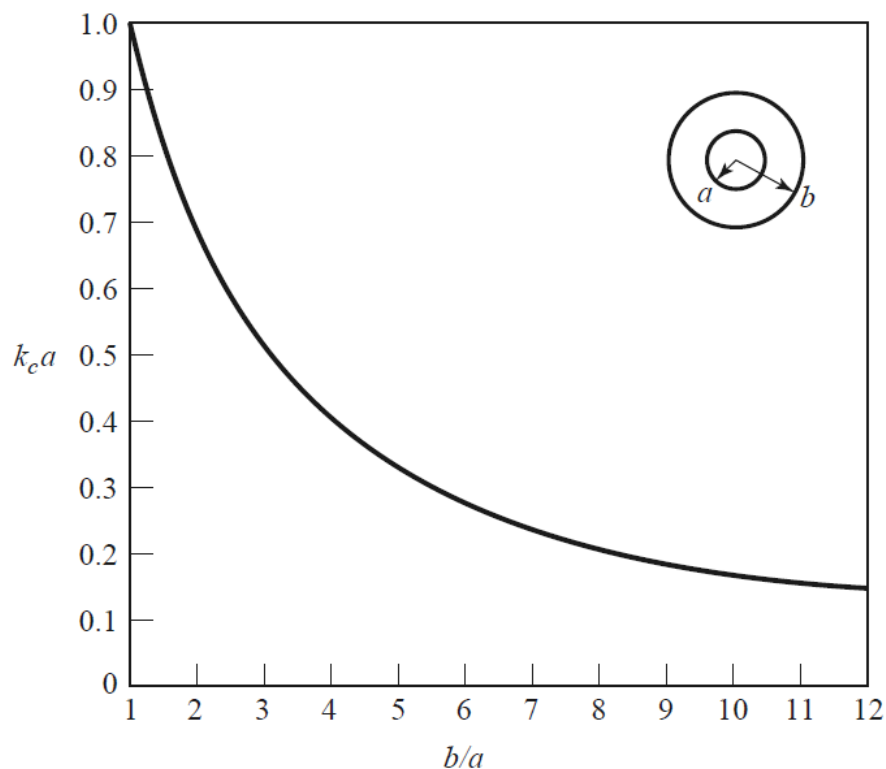


Figure 3.7: Normalized cut-off frequency of the dominant  $TE_{11}$  waveguide mode for a coaxial line. Image reproduced from [18].

In practise it is recommended to use a 5% safety margin with this approximation —  $0.95f_c$  [18].

### 3.2.3 Power Handling Capabilities

The power handling capabilities for waveguides is determined by the voltage breakdown of the dielectric medium inside the guide. Throughout this chapter the power combiner designs will be based on air-filled coaxial lines. Voltage breakdown occurs at electric field strength of  $E_d = 3 \text{ MV m}^{-1}$  for standard room temperature at sea level pressure. Thermal effects and reflections on the line may further decrease the power capacity of the structure. Given a coaxial structure with parameter dimensions as shown in Fig 3.2 the field strength of coaxial lines vary according to

$$E_\rho = \frac{V_0}{\rho \ln b/a} \quad (3.4)$$

which has a maximum at the inner conductor  $\rho = a$ . The maximum peak-to-peak voltage before breakdown occurs is then given by

$$V_{ppmax} = E_d a \ln(b/a), \quad (3.5)$$

which gives a maximum power of

$$P_{ppmax} = \frac{V_{ppmax}^2}{2Z_0} = \frac{a^2 \pi E_d^2}{\eta_0} \quad (3.6)$$

where  $\eta_0 = \sqrt{\mu_0/\epsilon}$  is the intrinsic impedance of the dielectric medium. Voltage breakdown and arcing are transient effects that occur at high-speed and therefore the given power and voltage limits are peak values and the average power capacities will be lower. The power capacity can be increased by using dielectric materials other than air, that typically have higher electric breakdown strengths, but these may be more susceptible to ohmic losses and thermal effects [29].

A minimum power handling capability places restrictions on the minimum size of the coaxial combiner, but it is not necessarily the primary factor imposing the lower-limit on the radial size of the combiner. Depending on the number of peripheral ports needed and the type selected from the standard connectors available, as well as the isolation requirements and spacing between connectors, the combiner may require a larger diameter than needed for the prescribed power handling. Most of the standard connectors for coaxial lines use a  $50 \Omega$  characteristic impedance, with some exceptions such as  $75 \Omega$  in television cables. Historically these choices of standard line impedances are due to the fact that air-filled coaxial lines have a minimum attenuation at a characteristic line impedance of  $77 \Omega$  but a maximum power capacity is achieved at a line impedance of about  $30 \Omega$ . The  $50 \Omega$  standard for coaxial line connectors, thus stems from a compromise between minimum attenuation and maximum power handling capability [18].

### Connector Types

As mentioned before the choice of connector type is an important consideration which entail compromises that have to be taken into account when specifying the design goals. The power combiner designs within this chapter utilizes two different types of connectors

for the central combining port and for the peripheral ports which deliver the signals that are combined. The central combining port requires the highest power handling capacity as the combined signal power is transmitted from this connector. The peripheral port connectors does not need as much power capacity as the power from the central port is equally divided between the  $N$  peripheral ports. For the reasons given, the central combiner will need a larger connector type with more power handling capacity whereas the peripheral connectors may be smaller in order to fit more ports on a device with a given radial size, or to minimize the radial size of a devices with a specified number of peripheral ports.

The central port is designed with a N-type, high performance RF coaxial connector. It is particularly suited where high power and performance is needed. Although it is physically larger than other types of connectors such as the BNC or TNC type connectors, the N-type connector is more suited to use with larger, low-loss cables and is able to withstand relatively high power. The connectors is specified to function to up to 18 GHz. The peak power capability of an N connector is determined by voltage breakdown in the region near the centre pin. The average power rating is affected by the level of heating that occurs due to resistance on the centre contact, at the points of the contact in particular because of the skin effect that is frequency dependent. Some N-type connector data sheet report that with a perfect load  $VSWR = 1 : 1.0$  a power rating up to 5 kW at 18 GHz.

The peripheral ports are designed to use Sub-Miniature A (SMA) connectors which are small compared to N-type connectors and have less spacial requirements. The SMA connectors can also function at 18 GHz but figures for power handling of SMA connectors vary widely between manufacturers with some data sheets indicating power handling capacity of 500 W at 1 GHz to power ratings just below 200 W at 10 GHz.

### 3.2.4 Bode-Fano Criterion

An important trade-off to keep in mind when designing impedance transformers is the Bode-Fano criterion. It presents the theoretical limits that constrain the performance of an impedance matching network. The criterion provides the compromise between the maximum allowable reflection in the passband for a given bandwidth. The full scope of this criterion will not be discussed here, but a summary thereof may prove useful in benchmarking designs with certain load impedances [30]. In summary the conclusions from Fano's theoretical limitations on arbitrary impedance matching is given:

- For a particular load, the bandwidth of the matching circuit can only be improved at the cost of a higher reflection coefficient.
- A perfect match is only possible with a zero bandwidth, i.e. the reflection coefficient can only be zero at a finite number of discrete frequencies.
- As the impedance ratio  $R$  increases, the performance of the matching circuit, in either bandwidth, passband reflection coefficient or both, must decrease.

This means that a matching network has to be optimized so that the return loss curve in the passband is as small as possible for the given bandwidth requirement. An ideal response would look like a square wave, but would require a matching circuit with infinite elements. Instead the ideal response may best approximated with a Chebyshev response

when the maximum of the passband ripple is made equal to the desired reflection coefficient.

### 3.2.5 Summary

This section has highlighted important considerations to take into account at the initial design stage. Not only have general compromises in designing coaxial power combiner been pointed out, but also some specific constraints when integrating a Chebyshev short-step impedance transformer within a coaxial combiner. The trade-off between choices in design parameters are summarised as:

- Waveguide implementation of short-step filters requires a back-short. A purely analytical synthesis is substituted for a synthesis procedure that incorporates a numerical approach that includes a back-short for a specified transformer ratio and bandwidth.
- Higher order modes of propagation bring about undesired effects and the cut-off frequencies of these modes have to be taken into account at the cost of power handling capability.
- Power handling capacity has to be optimized within the constraints imposed by the dominant higher order mode cut-off frequency and the number of peripheral ports required.
- Coaxial connector types is important to consider given the number of ports, isolation and maximum combiner size requirements.
- For the impedance transformer ratio dictated by the number of peripheral ports, there is an theoretical upper-limit on the bandwidth and passband return loss performance of the matching network as presented by the Bode-Fano criterion.

### 3.3 Coaxial Combiner with an Integrated Short-Step Impedance Transformer

The discussions leading up to this point has provided some of the minimum theoretical and practical requirements that enable the design of a coaxial power combiner with an integrated short-step Chebyshev impedance transformer. The goal is to reduce the physical size of the power combiner by exploiting the benefits of the short-step filter as presented in Chapter 2.3, whilst retaining acceptable performance. This section presents the methodology used in the design of a wideband, axially symmetric power combiner. The different facets of the design is broken down into subsections that describe each design stage individually. A simple design example demonstrates how every stage in the design process is tied together into the final result. Finally the simulated results of a few higher order designs are analysed and compared to literature.

#### 3.3.1 Coaxial Line Impedance and Step-Discontinuities

Literature provides useful formulas in the design and analysis of pure TEM transmission lines. Among others [18] shows how to calculate the characteristic impedance of a coaxial line section. This is a simple method for implementing the unit element sections from a synthesised short-step filter. The characteristic impedance of a coaxial line is calculated using standard transmission line theory by

$$Z_c = \frac{\eta}{2\pi} \ln \frac{b}{a} \quad (3.7)$$

where  $b$  is the outer conductor radius and  $a$  is the inner conductor radius as shown in Fig. 3.2, and  $\eta$  is again the intrinsic impedance  $\eta = \sqrt{\mu_0/\epsilon}$  as in (3.6). When a step-discontinuity occurs within a coaxial line, such as where line sections of different radii are joined, as seen in Fig. 3.3 between B and C, a shunt capacitor may be used to represent the effect. Solmo [31] provides the approximate formula for computing the step capacitance at the discontinuity. Many other useful approximations and circuit representations of complex electromagnetic discontinuities within waveguides are presented in [32] that may be incorporated in waveguide designs to achieve specific goals.

#### 3.3.2 Stub Line Implementation within Coaxial Waveguide

There are numerous ways with which to implement an approximate shunt stub line as that of a synthesised short-step filter within an over-sized coaxial waveguide. Cylindrical dielectric resonators is one of the topics from literature that has found application in microwave circuits for some time [33, 34]. Since cylindrical dielectric resonators can be designed to operate with performance similar to waveguide cavity but with a much smaller size, they offer a very attractive alternative for applications where the size of microwave circuits are of concern. The successful implementations dielectric sections, such as in [35] show how the purely dielectric resonators still make a significant contribution to the length of the structure. An alternative design approach is proposed and implemented in this section. The open-circuited shunt stub lines in Section 2.3.4 are presented as sections of coaxial line with a given characteristic impedance and electrical length and shown in Fig. 2.12. The same line sections may be represented with an equivalent circuit model consisting of a shunt resonance branch with a capacitor and inductor as shown previously in Fig. 2.7 and illustrated again in Fig. 3.11b.

An alternative implementation to pure dielectric resonators or coaxial shunt lines for realising the shunt stub lines is presented in Fig. 3.8 showing the design parameters. Fig. 3.9 displays the 3D bisection views of the implemented discs. The dielectric discs of thickness  $d_i$ , where the subscript  $i$  distinguish between the individual discs, consists of a substrate suitable for high frequency circuits with a dielectric constant  $\epsilon$ . The line characteristic impedance and electrical length, or equivalent capacitance and inductance is approximated by etched microstrip like lines which is known to have quasi-TEM characteristics. The lines are etched on the face of the disc and configured like the spokes of a wheel, symmetrically around the center conductor. The spoke-like etched conductive lines have two parts: Each spoke-line has a positive section on one face of the disc that connects to the inner conductor and stretches radially outwards towards the outer conductor but does not physically connect to the outer conductor. The other section of the conducting spoke-line is positioned on the opposite face of the disc and connects to the outer conductor and stretches inward towards the inner conductor. In the most simplistic case the line ends overlap each other at a radius  $c = r_m + \frac{r_0 - r_m}{2}$ , the center radius between the inner- and outer conductors of the coaxial waveguide with radii  $r_m$  and  $r_0$  respectively. This overlap, with a dielectric material of thickness  $d$  between the etched lines, resembles the configuration of a parallel-plate capacitor and capacitively couples the inner conductor of the coaxial waveguide to the outer conductor.

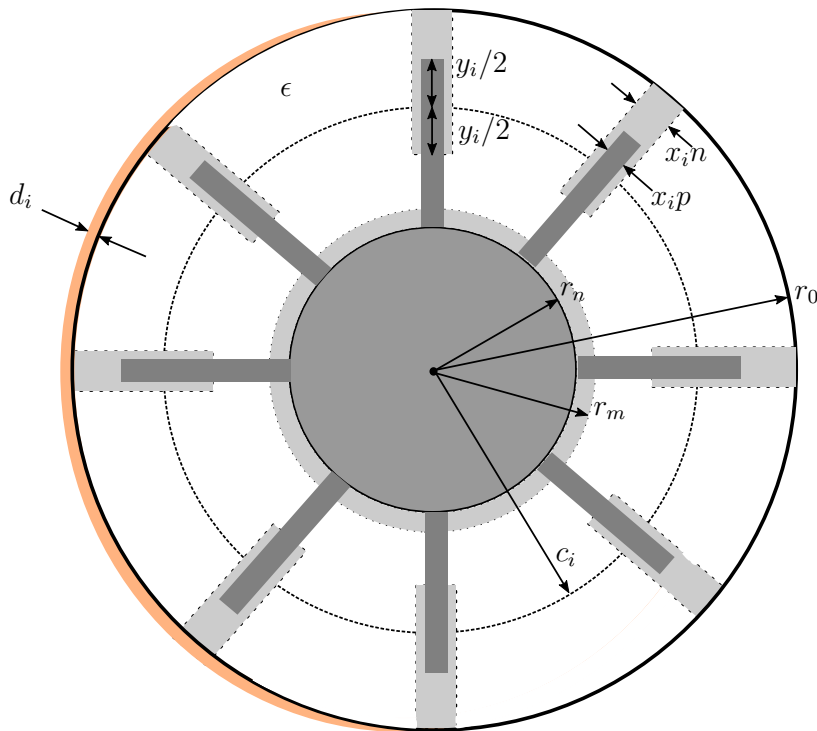


Figure 3.8: Configuration of shunt stub-line implementation within a coaxial waveguide using microstrip lines etched on a PCB substrate.

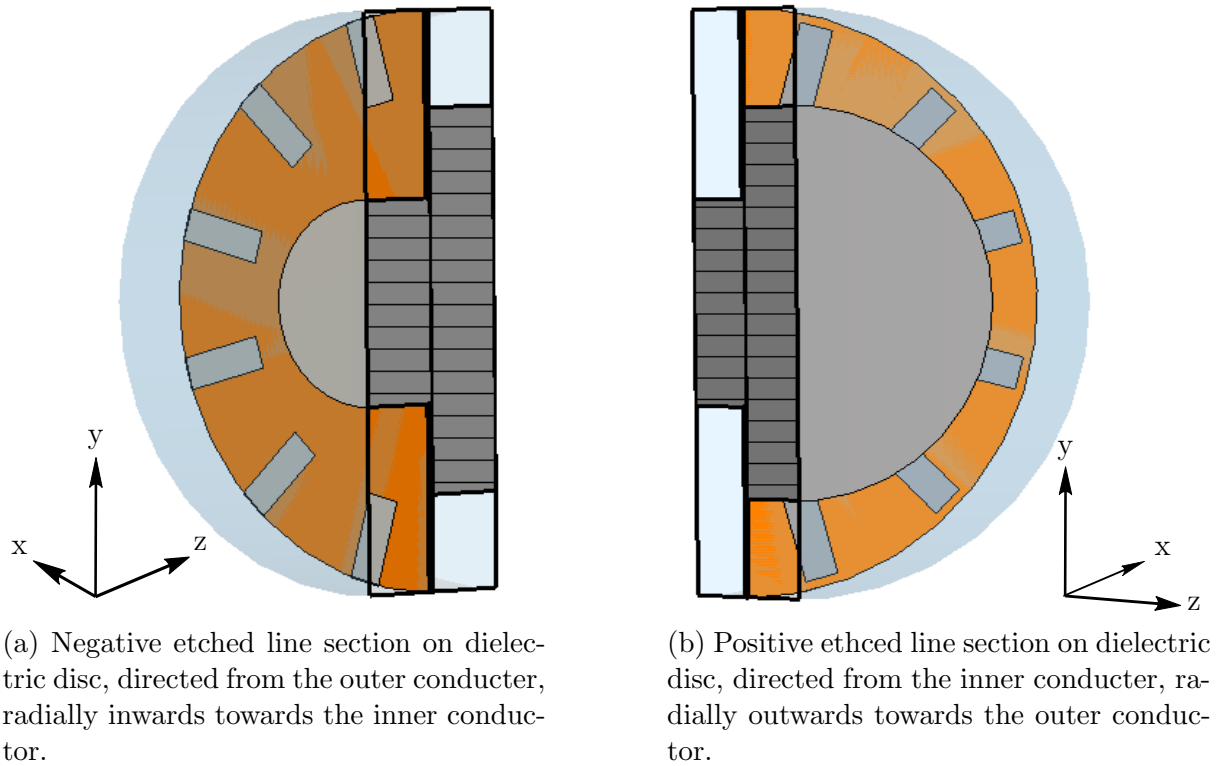


Figure 3.9: X-plane bisection views of the a dielectric disc at a step discontinuity in the oversized coaxial inner conductor. a) Displays the face of the disc with the negative etched line sections (spokes), where b) shows the opposite face of the disc with the positive spokes. The spokes overlap in the radial direction to form a quasi-TEM transmission line.

Alternatively the configuration may be thought of as a flattened coaxial line as demonstrated in Fig. 3.10 of which the distance between the outer- and inner radius is  $d = r_0 - r_m$ , and the ratio  $r_0/r_m$  of the is determined by the desired line impedance, which from (3.7) can be written as

$$\frac{r_0}{r_m} = \exp\left(\frac{2\pi Z}{\eta}\right). \quad (3.8)$$

When the conductors of a coaxial line is flattened into a micro strip format, the width of each conductor is given by the circumference of the initial coaxial conductors  $x_n = 2\pi r_0$  and  $x_p = 2\pi r_m$ .

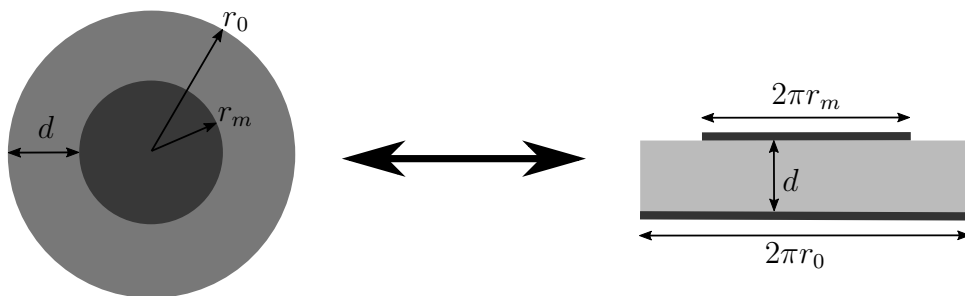


Figure 3.10: Coaxial line parameters when flattened out into a micro strip line configuration.



The line widths  $x_n$  and  $x_p$  for the negative line and positive respectively, together with the length of the line partly determines how much inductance the spoke-line has. The larger the overlapping area of the lines the higher the capacitance and the thinner and longer the lines become the higher the inductance become. The disc is effectively a resonant structure used to realise the shunt stub lines from the filter synthesis. The simple configuration can be tuned to approximate the synthesised  $L$  and  $C$  equivalent values for a given shunt element, by tuning the thickness of each line together with how much the lines overlap. Other parameters of importance is the central radius of the overlap — in the simple case above the overlap line was fixed at the centre between the coaxial conductors but  $c$  may be chosen at any radius  $c$  where  $r_m < c < r_0$ . Another parameter is added when choosing the number of spoke-lines, bearing in mind that the structure has to maintain its symmetry to avoid undesired effects from higher-order modes. With the number of spoke-line equal to  $N_s$ , they are arranged symmetrically at  $360^\circ/N_s$  from each other. Electrically the spoke-lines are in parallel and their combined capacitance, with all spoke-lines identical, is approximated with simple circuit theory given by

$$C_{||} = N_s \times C \quad (3.9)$$

and the parallel inductance is

$$\frac{1}{L_{||}} = \frac{N_s}{L} \quad (3.10)$$

Adjusting the  $L$  and  $C$  values independently from each other is not entirely possible with the given configuration. The adjustable parameters for the disc is summarised in the table below.

Disc parameter	$L - adjusted$	$C - adjusted$	$Z - adjusted$	electrical length
$x_p$	Y	Y	Y	Y
$x_n$	Y	Y	Y	Y
$y$	Y	Y	Y	Y
$N_s$	Y	Y	Y	N
$c$	Y	Y	Y	Y
$d$	Y	Y	Y	Y
$\epsilon$	Y	Y	Y	Y

Table 3.2: A summary of the disc parameters and the elements values affected with changes in the given parameters.

The discs are placed at the step-discontinuities within the combiner as shown in Fig. 3.3 and Fig. 3.11a. The dielectric by itself may be modelled as a shunt capacitor between the coaxial conductors. As the step discontinuity is also modelled as a shunt capacitor, which is effectively in parallel with the disc, the circuit model for the disc at the step discontinuity is a shunt capacitor that combines the capacitance of each. The etched line sections contribute further to the total capacitance and also adds inductance in series with the shunt capacitance. The etched disc placed at a step-discontinuity within the combiner and the circuit model approximation thereof is illustrated in Fig. 3.11.

The positive etched line section on the disc is on the face orientated towards the centre conductor with the larger radius  $r_m$  so that when the disc is pressed against the conductor the etched conductor can make good electrical contact with the centre conductor of radius  $r_m$ . The negative etched section is placed on the opposite face of the disc, orientated in the direction of the smaller centre conductor with radius  $r_n$ , and can be electrically connected to the outer coaxial conductor by practical means, which is discussed later.

Each shunt stub from a synthesised filter of order  $N$  is realised with a disc as described above. Every disc will have its own parameters which is identified by the subscript  $i$ , where  $i = 1, \dots, N/2$ .

Exact circuit models for the given physical parameters are often not sufficiently accurate and the relationship between the disc parameters and the circuit element values have to be extracted with optimization and full wave simulations discussed in Section 3.3.5.

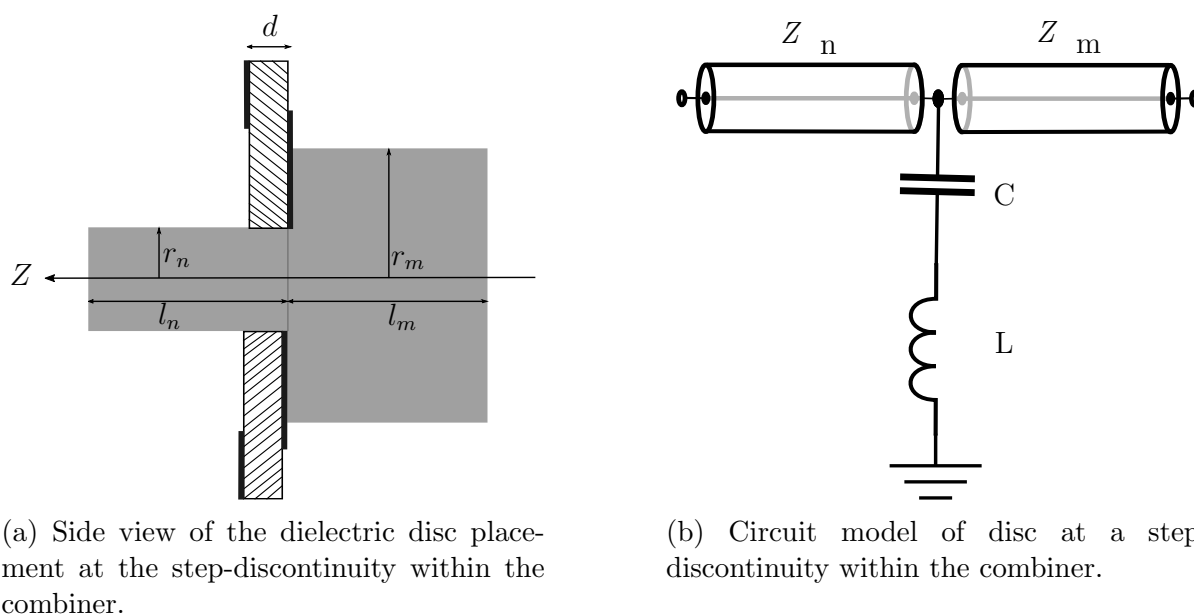


Figure 3.11: Disc placement at the step-discontinuity within a combiner and the circuit model representation thereof.

### 3.3.3 Peripheral Coaxial Line Transition

The filter synthesis from Section 3.2.1 for the short-step impedance transformer with a back-short requires a shunt stub line at the same node as the peripheral ports. This implementation proves to be a difficult task as a shunt stub line has to be realised in parallel to the shorted coaxial feeding network. In Fig. 3.3 the dielectric disc with the peripheral ports is shown between sections C and D with the back-short to one side and a transmission line section to the other. Fig. 3.12 illustrates how a disc is used to accommodate the centre feeding pins of the SMA connectors that have to connect to the centre coaxial conductor, whilst also approximating the shunt stub element between the outer- and inner conductors of the combiner. The two central coaxial conductors on either side of the peripheral ports, the back-short and the transmission line element, are shown with the darker inner radii  $r_n$  and  $r_m$ . The centre  $c$  of the gap between the

outer conductor and the larger of the two inner conductors of the combiner is again used as an central overlapping line. From (3.8) it can be seen that the more ports that are combined, the smaller the equivalent impedance becomes at the combining section. With smaller line impedances the gap between the outer- and inner conductors of the coaxial combiner become smaller and increase the difficulty with which sufficient capacitance can be realised, especially as the shunt capacitance requirement is typically the largest at the peripheral ports section. Here the inductance requirement is usually small. In this case the etched spoke-line configuration used in the previous section is no longer capable of realizing enough capacitance. One way to work around this problem is to adjust the dielectric disc so that the spokes-lines from Fig. 3.4 is widened to the point where the etched lines joins and become circular. This configuration has considerable higher realisable capacitance which is tuned by changing the amount of overlap i.e. by adjusting  $r_+$  and  $r_-$  as shown in Fig. 3.12. This method also reduces the shunt inductance which is advantageous as an extended inner-conductive ring is usually required to reduce the inductance of the longer SMA inner connector feeding pins that is required to make contact with centre conductor of the combiner [15, 36–38].

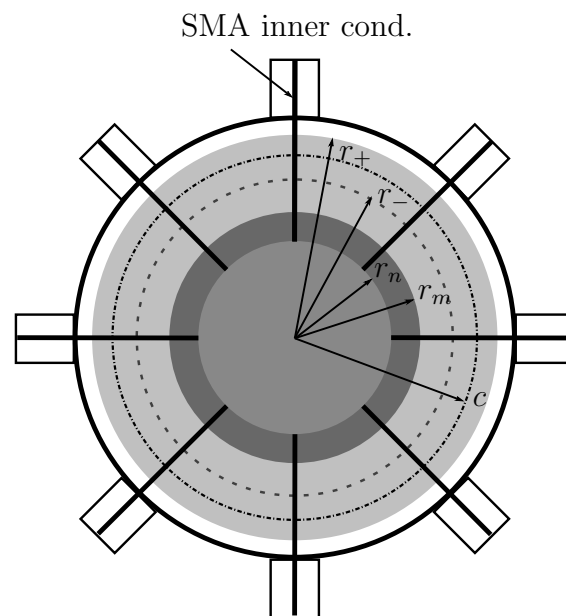


Figure 3.12: Dielectric disc configuration with overlapping ring conductors used to accommodate the peripheral port connections as well as providing the shunt line from the synthesised filter.

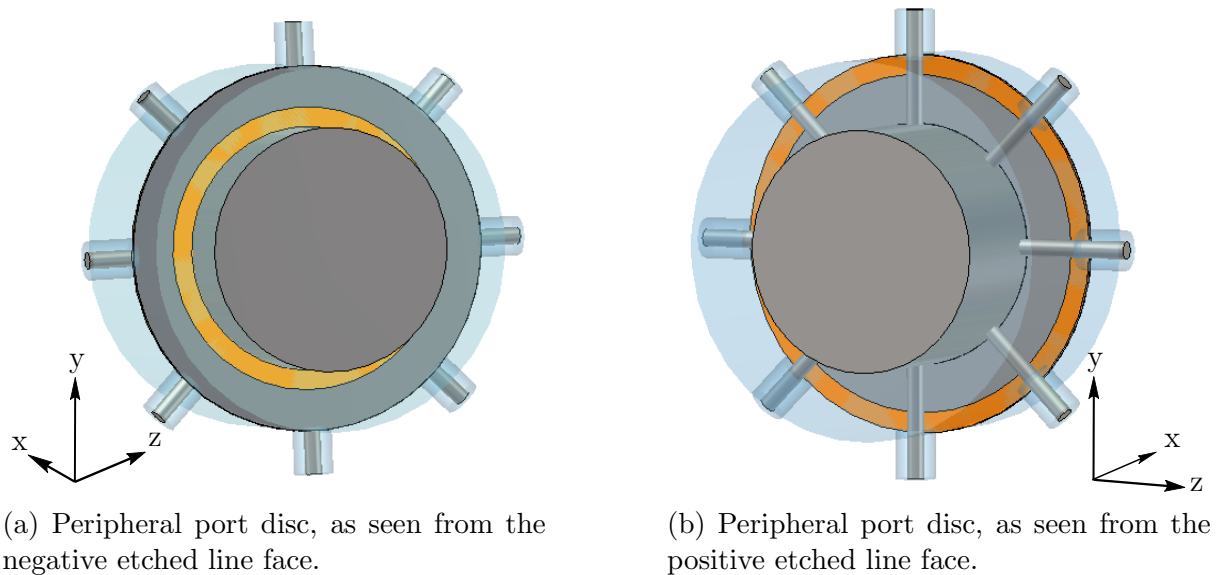


Figure 3.13: A three-dimensional view of the a dielectric disc at the peripheral input ports. a) Displays the face of the disc with the negative etched annular ring, where b) shows the opposite face of the disc with the positive etched ring, making contact with the oversized coaxial inner conductor and also the centre conductors of the peripheral input ports. The positive and negative rings overlap in the radial direction. This serves to approximate the synthesised shunt element, whilst also reducing the inductance of the input port central conductors.

A typical problem when dealing with the peripheral port matching is that the inner conductor of the peripheral connector is directly connected to the central oversized coaxial waveguide. In this case the ports are matched over only small bandwidths as small as 10% [15].

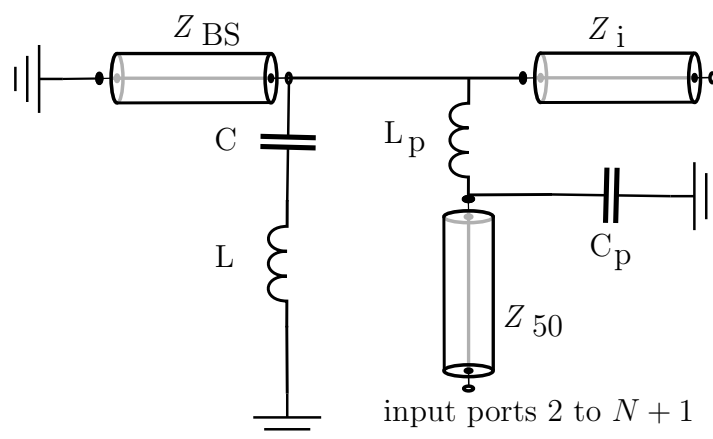


Figure 3.14: Circuit model representation of section D-C of Fig. 3.3.

With reference to Fig. 3.14 showing an equivalent circuit model representation of section D-C from Fig. 3.3 the reason for the typical narrow band match is revealed. The inductor  $L_p$  represents the inductive effect that occurs with the extended length of inner conductor of the peripheral port connected directly to the central coaxial conductor passing through the air-filled gap in the radial direction between the inner- and outer conductors of the

combiner. In this case the effect of  $C_p$  is negligible with  $L_p$  having considerable value, thus a wideband match cannot be achieved. A proven solution to this problem [36–38] is to have a conducting ring placed transversally around the central conductor to decrease the air-filled gap between the outer- and inner conductors of the combiners. Another approach is to use the dielectric disc configuration proposed in Fig. 3.12 with a etched ring connecting the feeding pin from the peripheral connector to the centre conductor of the combiner. This significantly reduces the inductive effect of  $L_p$ , by effectively shortening the electrical length of the peripheral centre conductor, but have to also approximate the synthesised values for  $L$  and  $C$ . Full wave circuit simulations using Computer Simulation Technology's Microwave Studio (CST-MWS) and Application Wave Research (AWR) Microwave Office is used to model the peripheral coaxial ports transitions into the oversized coaxial waveguide. Further optimization and circuit model extractions are done using space-mapping techniques.

### 3.3.4 Central Impedance Tapered Line Transition

It is often the case with axially symmetric power combiners that the dimensions of the oversized waveguide structure at the combining central port is not compatible with the dimensions of standard connector types used with power combiners. A tapered line section, as shown in section B-A in Fig. 3.3 usually solves this problem by matching the oversized waveguide to the central port connector in both impedance and size. Usually these sections are referred to as tapered coaxial line, but it more closely resembles a conical line [32], and can more precisely be modelled as such. In the simplest case, the tapered transition is designed for geometric simplicity as shown by Fig. 3.15 and Fig. 3.16 and has a constant impedance. A smooth conical to coaxial transition with a constant characteristic impedance is presented in [39] that has higher peak power handling compared to simple geometric transitions that typically has sharp corners at the junctions between the coaxial and tapered sections illustrated by A and B in Fig 3.15. Due to the constant characteristic impedance of the transition it is mainly used to match sections of identical impedance. A design and analysis of conical to coaxial impedance taper is presented in [40] which allows for matching between a conical and coaxial line with different impedance levels. Both [39,40] transitions are formed with a single pair of constant radius arcs that transition the conical inner- and outer conductors to that of a coaxial line. More recent designs [41, 42] allow for more degrees of freedom within the design of an conical to coaxial line transition with an arbitrary smooth impedance profile. These have shown significant improvement in bandwidth performances compared to [15] and have circuit models which are in good agreement with full-wave simulations and measurements.

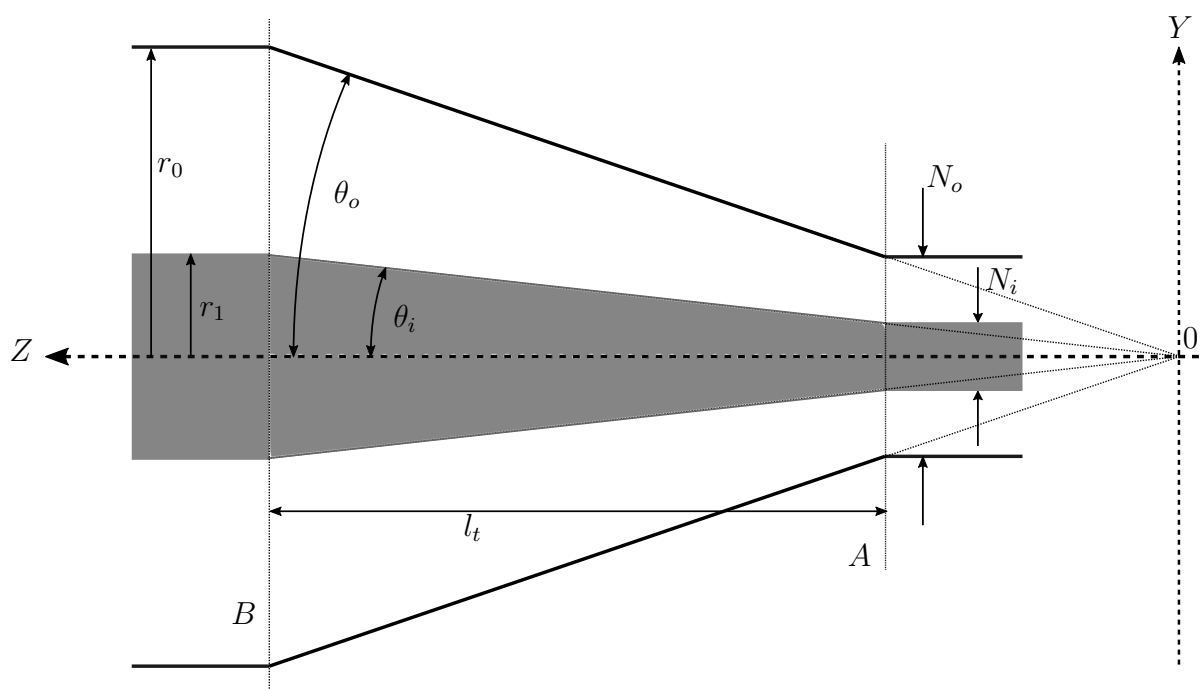


Figure 3.15: Tapered line section B-A of Fig. 3.3.

Although more advanced design methods are available from [40–42], it should suffice to use a geometrical design for demonstration purposes. In [15], where a geometric design is used for the taper, the length  $l_t$  is optimised in a full-wave simulation parameter sweep in order to obtain the optimal reflection coefficient. This results in a considerable length as the taper length is dependent on the ratio  $2r_1/N_i$ . The smaller  $l_t$  becomes, the larger the angles  $\theta_o$  and  $\theta_i$  become and the sharper the corners at junctions A and B become resulting in high field strength near the sharp edges which limits the peak power handling capability. Simply rounding the corners will increase the reflections from the junctions as the radius of the fillet is increased. Instead a step-by-step design [39] may be used to create a smoothly curved, well-matched transition. The matching and the taper length may be optimally designed using the more recently published techniques from [1, 40–42].

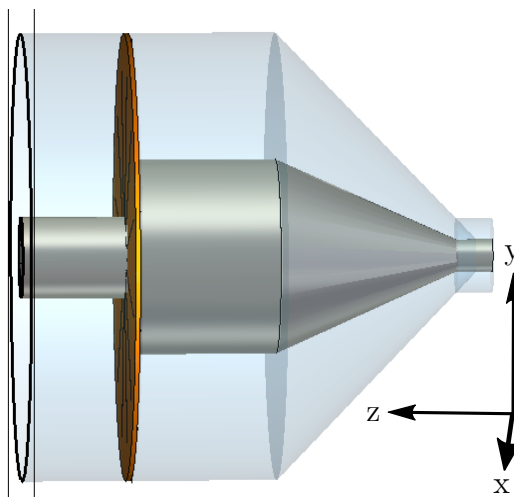


Figure 3.16: 3D view of a central port taper implementation.

### 3.3.5 Space Mapping Optimization

The design of the individual sections above, as well as the axially symmetric combiner as a whole is usually optimized with full-wave simulations which is often computationally expensive. The computational cost can be reduced by using circuit models, but it does not eliminate the need for full-wave parameter sweeps. Space mapping [43, 44] is a surrogate based optimization that employs circuit models to effectively reduce the computational cost by alignment of the circuit models to full-wave models. This optimization technique requires fewer full-wave simulations. Presented here is such a surrogate based optimization technique for the design and optimization of axially symmetric power combiners.

Computer-aided design (CAD) electromagnetic (EM) software has been crucial in full-wave simulation designs such as in [13, 15, 26, 40–42]. However, the relatively high computational cost of full-wave simulations is a limiting factor on the time and amount in which the parameter space can be searched. These place constraints on the attainable performance, and can be mitigated with circuit modelling which can accelerate the optimization process. As an example, circuit models may be used for sections within the combiner that have well established equivalent circuit models, such TEM coaxial line impedance [18, 32] or the capacitance of a stepped coaxial line [31] and the rest of the structure can be modelled with full-wave simulation, thereby reducing the size of the full-wave simulation problem. Dividing the problem into the appropriate parts may not be as simple, therefore to find optimal values full-wave optimization may still be a requirement.

An alternative is to construct circuit models for the entire combiner. This will also require full-wave parameter sweeps and optimization to find connections between the circuit element values and physical dimensions. With this approach, empirical data is used to extract regression models for relating circuit element values to dimensions of the combiner parts. Space Mapping takes advantage of the equivalent circuit models (coarse model), which have the underlying physical characteristics, shared by the full-wave (fine model) by shifting the load from the full-wave simulation to the circuit model, which is not as accurate, but evaluates faster. Stated formally, fine models, also known as high-fidelity models, are typically precise with excellent results when compared with practical measurements. On the contrary, low-fidelity models, commonly referred to as coarse models, does not provide the same degree of accuracy, but is used to alleviate computational cost of optimization.

If the design parameters of a given fine model is contained in a  $N_n$  dimensional vector, denoted  $\mathbf{x}_f$ , where

$$\mathbf{x}_f \in \mathbb{R}^{N_n \times 1}, \quad (3.11)$$

then the response of the model is stored in an  $N_m$  dimensional vector  $\mathbf{R}_f$ , with

$$\mathbf{R}_f \in \mathbb{R}^{N_m \times 1} \quad (3.12)$$

The subscript  $f$  indicates that the link to the fine model. The response of a model is typically  $S$ -parameters or a power quantity. When optimizing the fine model, the optimal response criteria is set in a objective or error function  $U$ , where a single value, such as the  $S_{11}$  parameter is given. An optimisation routine minimises the error function to get  $\mathbf{x}_f^*$ , the optimal point, and is written

$$\mathbf{x}_f^* = \arg \min_{\mathbf{x}_f} U(\mathbf{R}_f(\mathbf{x}_f)). \quad (3.13)$$

With circuit models that are accurate, similar results can be expected as there is normally a one-to-one mapping between the parameters of the fine model and the coarse model. This means that the input parameter vector for the coarse model may similarly be written as

$$\mathbf{x}_c \in \mathbb{R}^{N_n \times 1}, \quad (3.14)$$

with  $N_n$  the same as in (3.11). The response vector for the coarse model is then expected to be of the same size  $N_m$ , as that of the fine model and is expressed as

$$\mathbf{R}_c \in \mathbb{R}^{N_m \times 1}. \quad (3.15)$$

Usually there are discrepancies between the coarse and fine models, which are compensated for by a parameter extraction phase. During this phase the differences between the models are reduced by changing  $\mathbf{x}_c$ , the input parameters of the coarse model so that its response  $\mathbf{R}_c$  closely resembles that of the fine model  $\mathbf{R}_f$ . The way in which the  $\mathbf{x}_c$  parameters are changed is extracted and used to build a mathematical representation to reduce the error of the coarse model response relative to the fine model. The updated coarse model is known as the surrogate model with its response denoted by  $\mathbf{R}_s$ . The process of finding the surrogate model is known as alignment. It minimises the error between responses of the coarse and the fine model written as

$$\epsilon = \|\mathbf{R}_s(\mathbf{x}_c) - \mathbf{R}_f(\mathbf{x}_f)\|, \quad (3.16)$$

where in this case  $\epsilon$  represents the norm such as  $L_1$ ,  $L_2$  or Huber [45]. The design parameter  $\mathbf{x}_c$  and  $\mathbf{x}_f$  represents the respective coarse model and fine model design spaces and usually have the same values as they share the same underlying physical representation. When this is the case the subscripts are left out and the input parameter vector is simply written as  $\mathbf{x}$ . After the alignment is completed, the surrogate model is optimised to find the optimal point  $\mathbf{x}_c^*$  in the coarse model space. This point is then used to evaluate the next fine model. The new fine model response is compared against its goal as in (3.13) and the optimization process will terminate when the model meets the goal criteria. A classic space-mapping algorithm can be summarised step-wise as follows:

- Evaluate the fine model at an initial point,  $\mathbf{R}_f(\mathbf{x}_f^{(i)})$ .
- Extract a regression model for the surrogate model,  $\mathbf{R}_s$ .
- Update the surrogate model or mapping functions to align with the fine model.
- Optimise the surrogate model.

The space-mapping optimisation routine procedure is shown in a flow diagram in Fig. 3.17. It displays the different stages and how it is linked together. The probability that the optimisation routine will succeed depends on the agreement between surrogate and fine models. Having a strong agreement between the models can significantly improve the convergence and performance of the space-mapping routine, but even with a decent correlation between the models convergence is not guaranteed and therefore a reduction in the error between models at each iteration is not guaranteed. Throughout this thesis, an automated space-mapping framework [46] is used, which incorporates a trust-region (TR) to the algorithm to address convergence and robustness issues. The framework consists of links between numerical software solution utilising MATLAB which is linked via an application program interface (API) to some low-fidelity solvers, in this case AWR-MWS



is used to evaluate the coarse models, and for the high-fidelity solver CST EM simulation software is used. An in depth discussion on the optimisation techniques is beyond the scope of this thesis, but examples of how space-mapping is applied during the design process is given in the next section to demonstrate how essential the optimisation is to the design process.

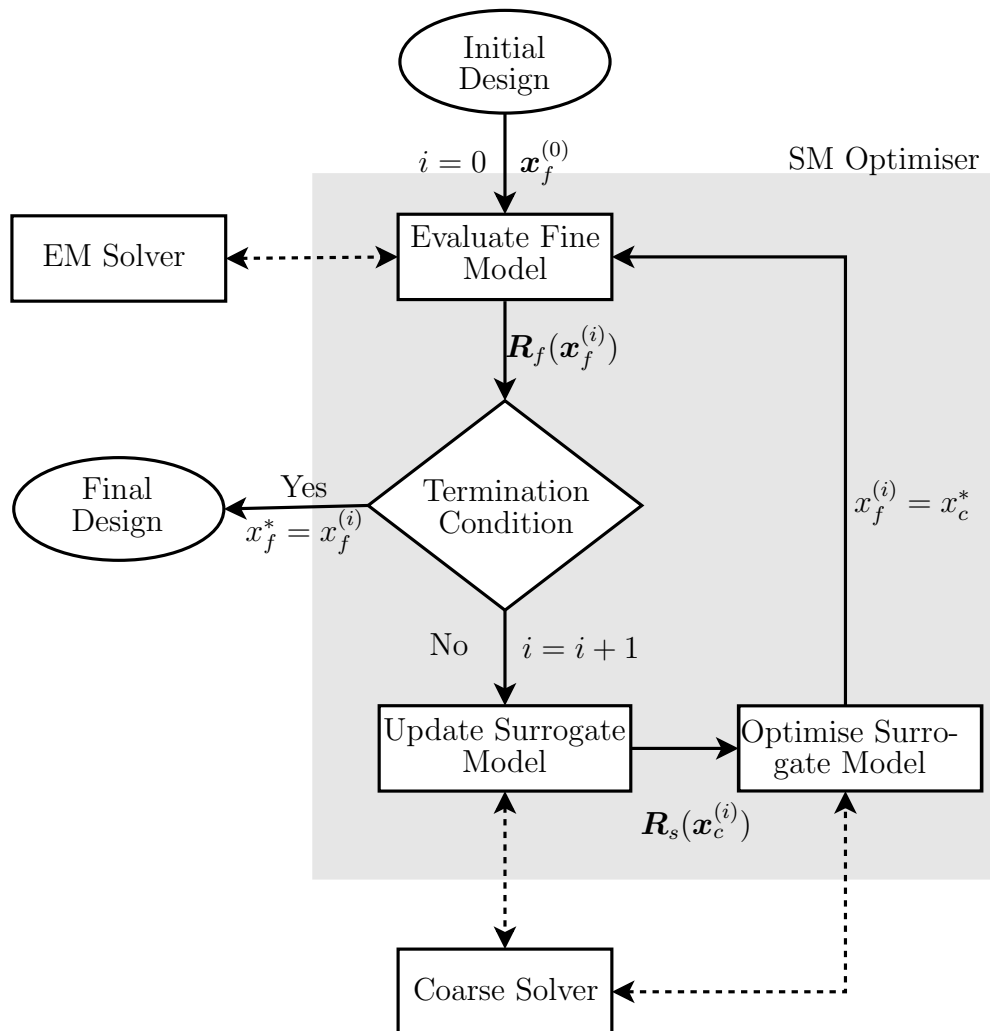


Figure 3.17: Flow diagram of a space-mapping optimisation routine. Adopted from [46]

### 3.3.6 Summary

This section has delivered the precluding design methodology that is used in the design example in the following section. The different sections of the combiner were discussed individually with a focus on the function and implementation thereof. Fundamental design equations are given and design configurations are presented and justified. The subsections presented physical configurations of the combiner parts and, where necessary, were accompanied by equivalent circuit models. A general discussion on the space-mapping optimisation routine is given, and how it is used to extract mathematical models that describe the relationship between the physical dimensions of the combiner parts and the circuit element values. The section in unison describe the inclusion of a short-step Chebyshev impedance transformer within a coaxial combiner that enables the compact size and small dimensions of the structure.

In summary the focus points of this section are:

- A discussion on coaxial line impedance and stepped discontinuity, how to calculate the values and how these are may be used in the design.
- The design configuration and implementation of the resonant open-circuit shunt elements from the filter synthesis.
- A method for realising the synthesised shunt element at the  $N$  peripheral input ports, where it is generally also required to reduce the inductance from the extended centre pins of the connectors.
- A general matching section design for accommodating the central, high-power combining output connector to the oversized coaxial structure.
- A general discussion on Space-Mapping optimisation algorithm and its importance in extracting mathematical relationships with which to optimise a high-fidelity structure at reduced computational costs, without which the design performance would be severely limited.

## 3.4 Design Example

This section presents a design example for an 8-way compact power combiner, integrating a 6-th order short-step Chebyshev impedance transformer for significant reduction in the overall size, particularly the length, of the structure. The theory, formulas and general discussions from the previous sections are used in unison to accomplish a simple design that serves to demonstrate the methodology used to realise arbitrary  $N$ -way combiners with higher order filters which may improve performance in bandwidth, reflection coefficient, or both. The design starts with initial requirements and design consideration. The general combiner configuration as shown in Fig. 3.3 is applicable. A short-step impedance transformer is synthesised using an appropriate order filter circuit to meet the bandwidth and reflection coefficient performance requirements. The element values for the synthesised circuit is numerically extracted with a MATLAB script and the coarse circuit model is constructed with AWR MWO. The 3D combining circuit is simulated within the CST 3D design space. Mathematical models, relating the physical waveguide parameters to circuit element values are extracted using a space-mapping framework to optimise the alignment between the coarse, AWR circuit elements, and the CST fine model 3D parameters. The alignment and model extraction of each dielectric disc is done individually then cascaded to form the full-wave 3D circuit model in CST. Finally the model is optimised using a space-mapping optimisation and the results are compared to the synthesised circuit.

### 3.4.1 Initial Design Specifications

For demonstration purposes, simple circuit specifications are chosen in order to highlight the essential steps in the design procedure. As mentioned before, the advantages of axially symmetric power combiners over corporate or chain-combiners are significant with large number of combining ports ( $N \geq 8$ ). Therefore the number of combining ports are chosen as  $N = 8$ . For this example the synthesis and design of a 6-th order Chebyshev impedance transformer synthesis, shown previously in Section 3.2.1 in Fig. 3.6a is presented step-by-step. The circuit has a bandwidth of 50% at an operating centre frequency  $f_o = 1.2$  GHz with a reflection coefficient of  $S_{11} \leq -27.5$  dB.

Table 3.1 list the total length of the circuit as  $0.1875\lambda = 46.875$  mm, not taking into account a tapered line section necessary for accommodating a practical central port connector. The specification for power handling capacity of the circuit is not given for now, instead it may rather be given as a result of the completed circuit. The design specifications are summarised as:

- The number of combining ports required  $N = 8$ .
- A passband bandwidth of  $\leq 50\%$ , symmetrically around the centre operating frequency  $f_o = 1.2$  GHz, from 0.9 GHz to 1.5 GHz.
- A passband ripple of  $S_{11} \leq -27.5$  dB.
- A total circuit length of  $\geq 0.1875\lambda$  (46.875 mm).

The goal is to keep the overall length of the circuit as small as possible, however, as discussed in 3.2.3, for maximum power handling capability the radius of the circuit has to large as possible without allowing the higher order modes of 3.2.2 to propagate within the structure. The cut-off frequency  $f_c$  as given in (3.3) is dependent on the outer- to inner

conductor radii  $b/a$ . From Fig. 3.7 it is seen that the larger the ratio  $b/a$  the smaller the number  $k_c a$  becomes and from (3.3) it follows that the cut-off frequency becomes smaller. The ratio  $b/a$  is also present in (3.7), the formula for impedance of a coaxial transmission line. As the  $b/a$  increase so does the characteristic line impedance. The combiner configuration has different transmission line sections with different impedances which is a result of the filter synthesis. Therefore the cut-off frequency can only be determined once the largest impedance for the transmission line sections are known.

A design choice is made by fixing the outer conductor radius for the oversized coaxial line. The radius  $r_0$  is chosen to accommodate eight SMA panel-mount type connectors for the peripheral input ports. The connectors are arranged symmetrically around the axis of the centre conductor of the combiner. Enough spacing is provided between the ports for the connector flanges and mounting screws to not interfere with each other. The dimensions used for the panel mount SMA connectors were obtained from [47]. The outer conductor radius chosen is  $r_0 = 21$  mm.

The final design parameter, which must be chosen initially, is the substrate and dielectric constant  $\epsilon_r$  of the discs. With a thinner substrate thickness  $d$  and higher value for  $\epsilon_r$  it is possible to realise higher shunt capacitance values. For the design example that follows an industry standard substrate thickness  $d = 0.508$  mm is used for all discs. A high frequency substrate, Rogers RO3003 is chosen which has a uniform dielectric constant of  $\epsilon = 3.0$  which is crucial for the symmetrical requirements of the design.

### 3.4.2 Synthesis

The necessary initial input parameters for a circuit synthesis have been established. An 8-way combiner has a normalised impedance transformer ratio of eight to one.  $N = 8$  and from (2.92) to (2.97) the commensurate stub line have a  $\lambda/16$  length at the operating frequency  $f_o$ . The bandwidth requirement is 0.5 from  $0.75f_o$  to  $1.25f_o$ . The polynomial  $P(z)$  is constructed using (3.1), where  $n = 6$ , the order of the short-step filter, and  $r = \frac{n}{2} = 3$ . From (2.102) to (2.107) the following design parameters are calculated,  $K_0^2 = 114.3143$ ,  $k^2 = 0.0134$ ,  $L_m = 0.0115$ , and  $VSWR = 1.1083$ . Six elements are extracted which correspond to the order of the filter.

Element extraction is done numerically as described in Section 2.3.3 and the normalised element values as well as the element values scaled to a  $50\ \Omega$  central output port is listed in Table 3.3.

	$Z_1$	$Z_2$	$Z_3$	$Z_4$	$Z_5$	$Z_6$
Normalised Elements	0.3562	1.6625	0.0967	0.5878	0.0445	0.3215
Scaled Elements	17.8086	83.1250	4.8359	29.3890	2.2261	16.0733

Table 3.3: The normalised and  $50\ \Omega$  scaled element values extracted during the synthesis procedure of a 6-th order short-step stub Chebyshev Filter with an impedance transformer ratio of 8.

As already mentioned the cut-off frequency  $f_c$  is dependant on the largest line impedance. From the above table that is  $Z_2 = 83.125\ \Omega$ . Using (3.7) and  $r_0 = 21$  mm the inner

conductor radius may be calculated as

$$\begin{aligned} a &= b/e^{Z_c \frac{\eta}{2\pi}} \\ &= 5.25 \text{ mm.} \end{aligned} \quad (3.1)$$

With the ratio  $b/a = 21/5.25 = 4.0$  and from Fig. 3.7 the estimated value for  $k_c a = 0.4$ . This means  $k_c \approx 76.19 \text{ m}^{-1}$  and can be substituted into (3.3) to find the cut-off frequency

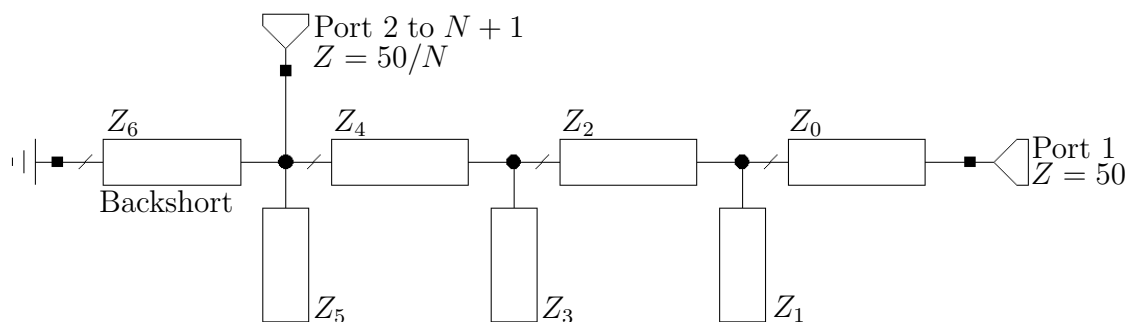
$$\begin{aligned} f_c &= \frac{kc}{2\pi\sqrt{\mu\epsilon}} \\ &= 3.637 \text{ GHz.} \end{aligned} \quad (3.2)$$

Applying a 5% safety margin still has the cut-off frequency  $f_c = 3.45 \text{ GHz}$  far above the upper frequency of the passband  $f_2 = 1.5 \text{ GHz}$  which means that the maximum power handling will most likely not be achieved.

For the sake of conformity, Fig. 3.18 show the element values are numbered starting at the combining central port, designated port 1.

The numbering of the element values conveniently have all shunt stub-lines, which will be implemented with the etched discs, as odd elements  $Z_{2i+1}$ , where  $i = 0, 1, \dots, n$ . All unit elements, which will form the sections of coaxial transmission line have even subscripts  $Z_{2i}$ .

This is a consequence of the fact that a bandpass filter has to be of even order. The synthesised circuit is shown in Fig. 3.18 The circuit differs from the one in Fig. 3.5 in that it includes an extra  $50 \Omega$  element at port 1. This is for practical reasons as it would be difficult to construct the circuit from Fig. 3.5 as it will require the implementation of a etched disc right at the central port. Instead a short  $Z_0 = 50 \Omega$  line is inserted which provides spacing between the disc and the central port connector. As the inserted line section impedance matches the port impedance exactly, the only implication from this addition is a phase shift, which may be compensated for during the model alignment phase of the design process.



(a) Circuit with shunt stub-line elements as synthesised.

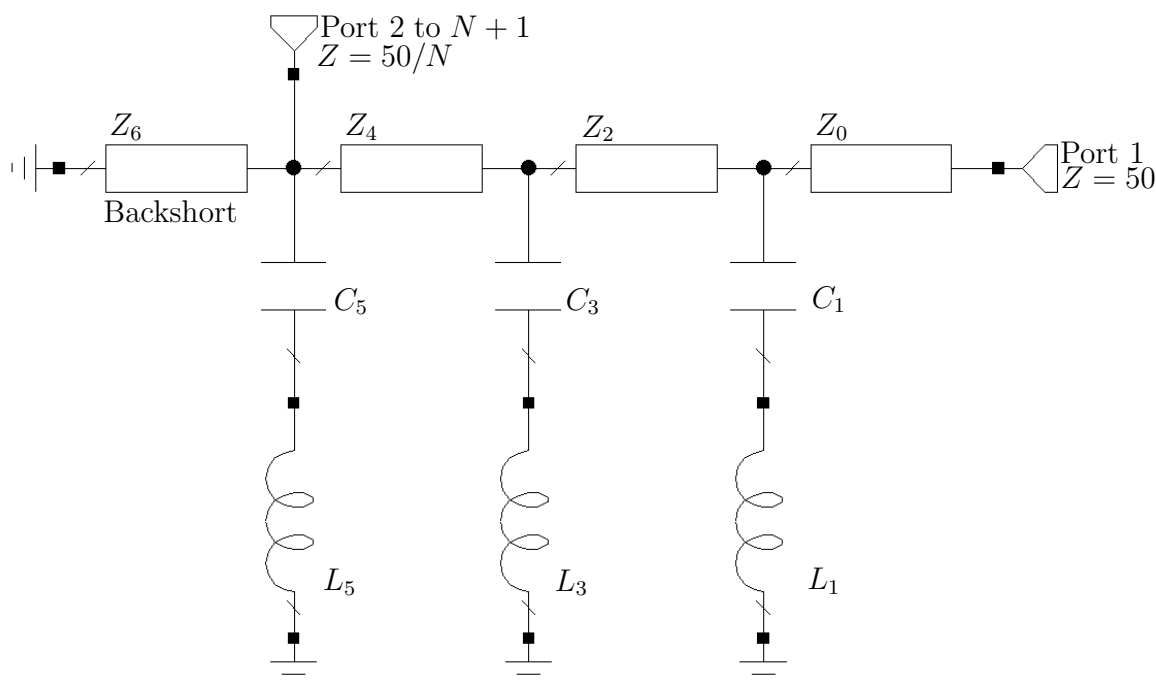
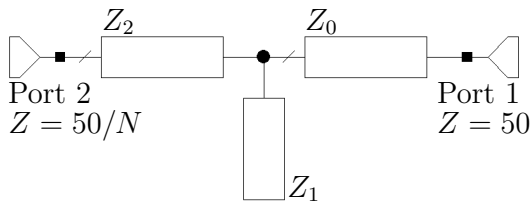
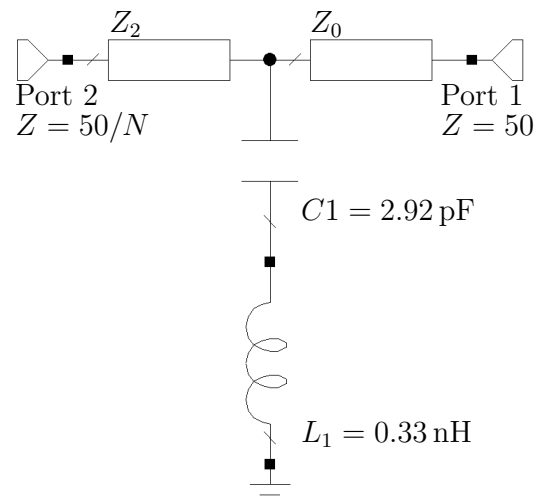
(b) Circuit with shunt stub-lines replaced with equivalent  $LC$  branches as also shown in Fig. 2.8b.

Figure 3.18: The synthesised circuit of the 6-th order short-step stub filter. The circuit element numbering is demonstrated and show the addition of element  $Z_0$  for practical construction. a) Displays the circuit with open circuit shunt stub lines as synthesised and b) shows the same circuit with the shunt elements replaced with equivalent  $LC$  branches. This is useful for approximating an etched disc implementation of the shunt stub lines.

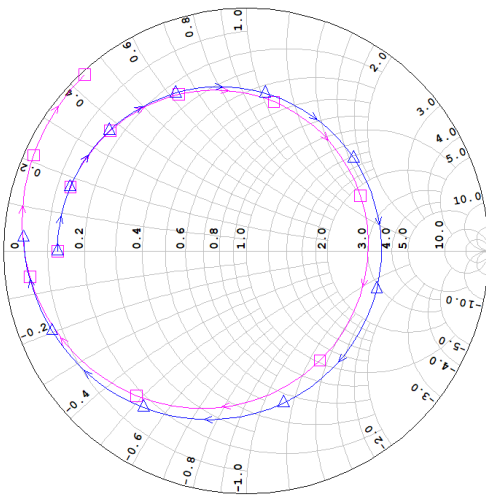
The phase length of each element is as before equal to  $\lambda/16$  which is equivalent to a phase of  $22.5^\circ$ . The values are numerically approximated with a Richard's transformation. The complex valued response is used to then fine tune the  $LC$  values in AWR MWO to match to each stub-line response. A complex valued response gives the best result because the phase of each response is also considered. Fig. 3.19 illustrate how the equivalent  $LC$  branch for the stub of  $Z_1$  is approximated and then fined tuned to match the stub-line response over the simulation frequency range.



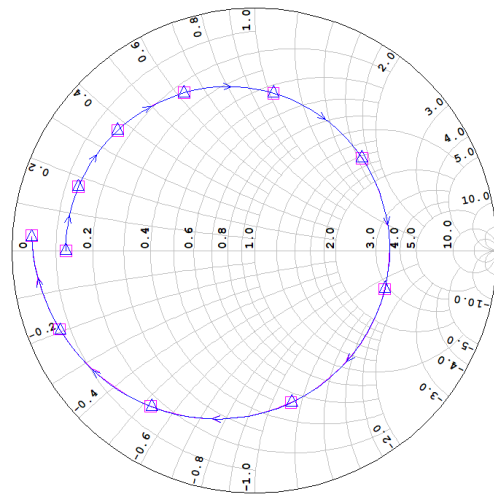
(a) The stub-line circuit of  $Z_1$  with the adjacent coaxial line sections.



(b) The approximate equivalent  $LC$  branch circuit of  $Z_1$  with the adjacent coaxial line sections.



(c) A smith chart of the  $S_{11}$  parameters of circuits in a) and b) with the approximated,  $LC$  values equivalent to match the stub-line element.



(d) A smith chart of the  $S_{11}$  parameters of circuits in a) and b) with the tuned  $LC$  values equivalent to the stub-line element.

Figure 3.19: The process for approximating equivalent  $LC$  branches for the different stub-lines is shown. The circuit from Fig. 3.18a is separated into individual circuit for each stub-line with its adjacent transmission line sections, demonstrated in a). Each stub-line is approximated as an  $LC$  branch as in b). The complexed valued response of the stub-line and approximate  $LC$  branch is shown in c) before fine tuning and in d) after fine tuning the  $LC$  values.

The values of the equivalent  $LC$  branches are given in Table 3.4. The alternative representation of the circuit offer additional equivalent parameters that may be used during the optimisation phase of the circuit that proves to be advantageous.

$C_1$	$L_1$	$C_3$	$L_3$	$C_5$	$L_5$
2.92	0.33	10.64	0.11	23.80	0.032

Table 3.4: The  $LC$  values approximation of each stub-line as numbered in Fig. 3.18b. The units of measure for capacitance is pF and nH for inductance.

The synthesised circuit response of Fig. 3.18a, shown in Fig. 3.20, may be considered as the ideal response with the given design constraints.

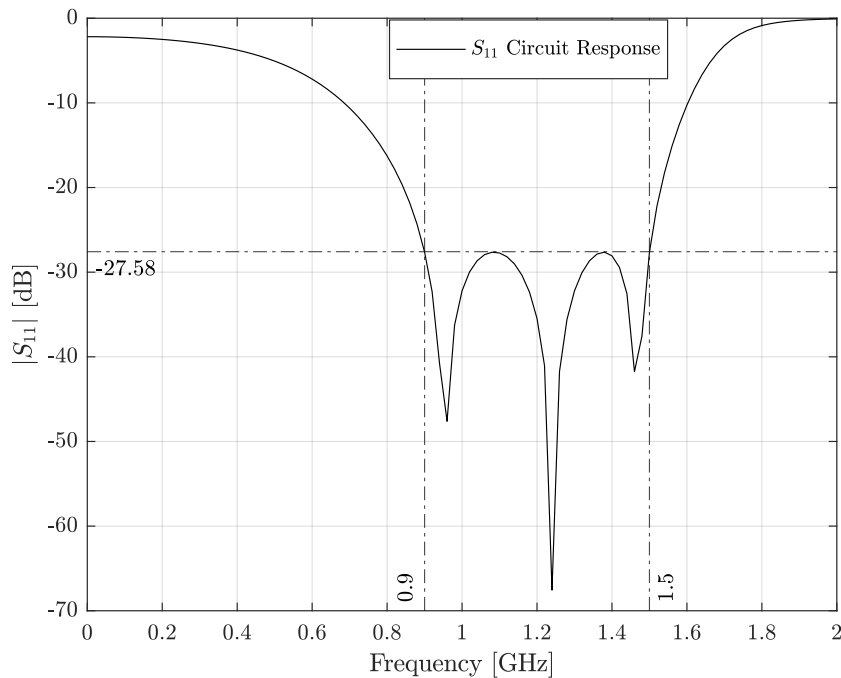


Figure 3.20:  $S_{11}$  response of the synthesised filter circuit from Fig. 3.18a.

The synthesised circuit gives the ideal performance that may be expected from the combining circuit. The maximum of the passband ripple can be seen to be  $\leq -27.6$  dB over a bandwidth of 50% at operating frequency  $f_o = 1.2$  GHz. The circuit performance and dimensions are summarised below and may be used as a baseline for evaluating the performance of the compact combiner to be constructed.

- A 6-th order filter response implemented with  $\lambda/16$  commensurate transmission lines.
- The circuit response has a the specified bandwidth of 50%, from 0.9 GHz to 1.5 GHz at an operating frequency of 1.2 GHz.
- The simulated passband ripple is measured to be  $|S_{11}| \leq -27.5$  dB.
- The total length of the synthesised circuit is  $\frac{4}{16}\lambda$  which is equal to 62.5 mm. This is excluding a central tapered line section.



### 3.4.3 Model Construction

The desired circuit response has been synthesised and a circuit has been simulated in the previous section. The task of integrating the circuit into an oversized coaxial combiner may begin. Some physical parameters and considerations are available from the discussions of Sections 3.4.1 and 3.4.2. These may immediately be utilised to start building the model for the combiner. The coaxial transmission line dimensions can be calculated from the initial design choice of  $r_0$ . The outer radius of the coaxial line is to be kept constant so only the inner radii of the individual coaxial line sections have to be calculated to realise the line impedances from the synthesis.

In the previous section the circuit was divided into separate sections. With each section including a stub-line with a corresponding adjacent transmission line. The sections are used to fine-tune an  $LC$  branch which serves as an equivalent circuit model for the open circuit stub-line. In a similar fashion the combiner can be divided into different parts, where each part represents a stub-line section with its adjacent coaxial transmission line sections. A dielectric disc with etched conductive lines, as described in Sections 3.3.2 and 3.3.3, is then used to approximate the open circuit stub-lines.

To accommodate the central port connector, a tapered line is included which provides a smooth transition between the physical dimensions of the N-type connector at the central port and the first section of coaxial transmission line. The complete structure is then finally pieced together from the individual circuits and then optimised with a space-mapping framework as discussed in Section 3.3.5.

The even numbered elements, with characteristic line impedances  $Z_0$ ,  $Z_2$ ,  $Z_4$  and  $Z_6$  are implemented as coaxial transmission lines. Each line section's characteristic impedance is calculated using  $r_0 = 21$  mm and (3.7). The inner radii for the even numbered sections are listed in Table 3.5.

Section	$Z_0$	$Z_2$	$Z_4$	$Z_6$
Impedance	$50 \Omega$	$83.125 \Omega$	$29.389 \Omega$	$16.073 \Omega$
Inner Radius	$r_1$	$r_2$	$r_3$	$r_4$
Dimension	9.1218 mm	5.2501 mm	12.8636 mm	16.0622 mm

Table 3.5: The inner radii dimensions for coaxial line sections with the corresponding characteristic impedances.

The odd numbered elements  $Z_1$ ,  $Z_3$  and  $Z_5$  are implemented with etched dielectric discs. Each disc is constructed in CSTs 3D design environment as shown in Fig. 3.21. The length  $l_1$  is as synthesised, but  $l_2$  is halved as the  $Z_2$  section is also present in the construction of the next disc. With this method of construction the idea is to ultimately construct the full structure by piecing together the individual parts. This works as the parts are chained together by effectively multiplying the ABCD matrices of each section. For an accurate chain matrix the transmission lines, which are present in two different simulations, have its length halved in each of the fine model simulations. This means the transmission line section between consecutive discs, is halved in each simulation. The halving takes place as far as possible from the shunt disc, so as to accurately simulate the near-field effects.

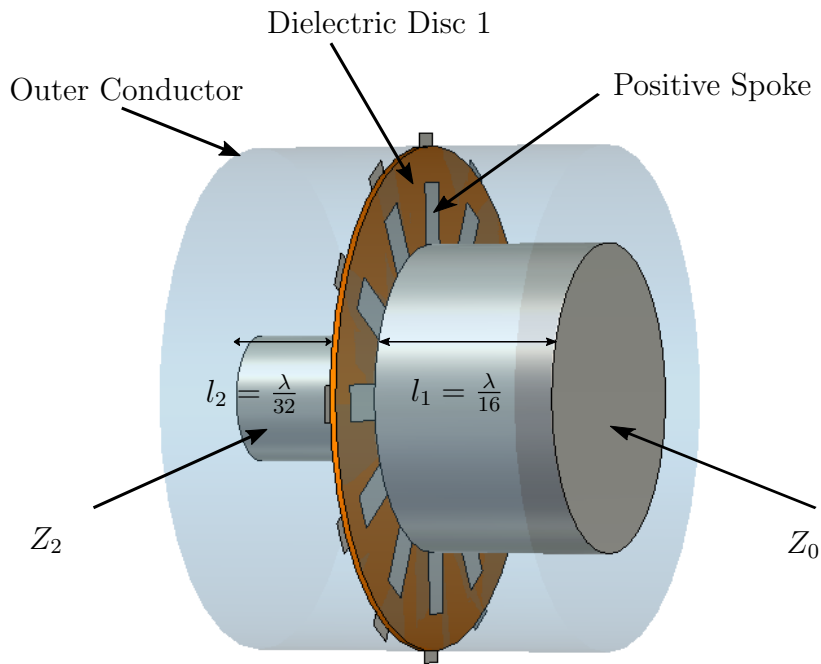


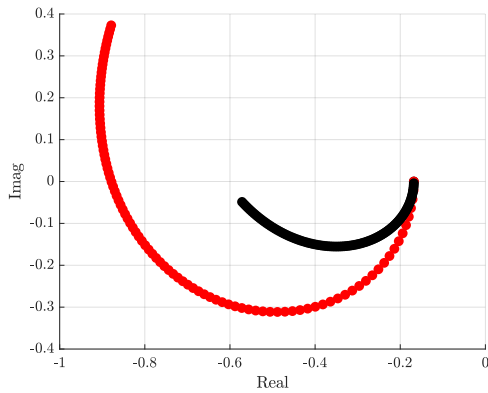
Figure 3.21: Dielectric disc 1, with its adjacent coaxial line sections  $Z_0 = 50 \Omega$  and  $Z_2 = 83 \Omega$ . The disc is used to approximate  $Z_1$  as seen in Fig. 3.19a and 3.19b.

A mathematical model, relating the disc parameters to circuit element values, such as impedance and electrical line length or approximately capacitance and inductance, have to be extracted. In order to simplify the process it is important to limit the amount of variables. For this reason the coaxial transmission line parameters are kept fixed, as these were calculated using well established formulas such as (3.7). Other parameters that may be fixed during the procedure is the thickness  $d$  of the dielectric disc and the dielectric constant  $\epsilon$  of the material used. Initially the number of symmetrical spoke lines is also kept fixed, as this accounts for larger steps in realisable capacitance and inductance. Also the centre of the overlap between the positive and negative spoke lines should be fixed.

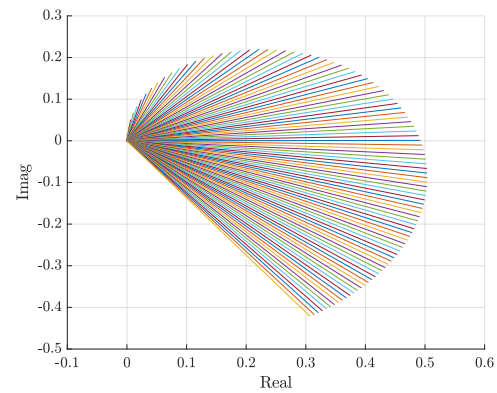
By choosing the widths of the positive and negative etched spoke lines, from Fig. 3.8, as equal  $x_p = x_n = x$  the number of variables is reduced to two. The width  $x$  and the overlap  $y$  are the only two remaining variables for the dielectric disc parameters.

A mathematical model is extracted by aligning a coarse model circuit response to the response of the fine model from Fig. 3.21 over the practical realisable range of  $x$  and  $y$  value combinations. The alignment stage from the space mapping framework discussed in Section 3.3.5 is of particular use here. The fine model simulations are done with CST and evaluate very fast due to the symmetry of the structure and because an individual disc model has low computational cost in comparison to more complex structures. The coarse models can be implemented by either circuit (a) or (b) from Fig. 3.19. Fig. 3.22 illustrates the alignment process. When the stub-line circuit from Fig. 3.19a is used, the alignment is carried out by tuning the impedance and electrical line length of the stub-line until the error between the fine model response and the coarse model response is minimised. The vector difference before and after alignment is shown in Fig. 3.22b and 3.22d. For the  $LC$  circuit of Fig. 3.19b the  $L$  and  $C$  parameters are tuned until alignment is achieved. This

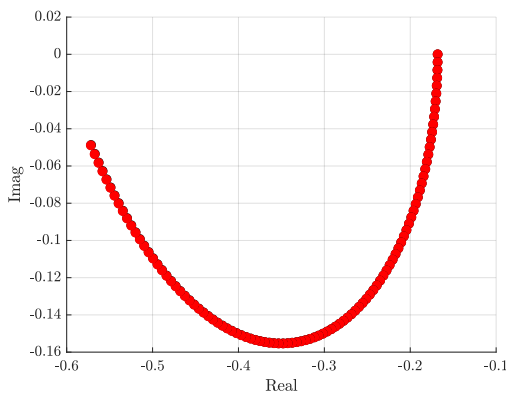
process is automated and repeated over a specified range of  $x$  and  $y$  values. The fine model variable parameters are constraint by what is physically realisable. The widths  $x_i$ , where  $i$  denotes the disc number, is constrained by the thickness of the coaxial conductor. If  $x$  is increased too much it will become larger than the outer conductor diameter  $2r_0$ . Except for the physical constraint,  $x$  needs to be limited so that adjacent positive spoke lines do not get too close to each other in order to avoid large coupling between these etched lines. The overlap  $y$  must also be limited to less than the gap size between the outer conductor and the larger adjacent coaxial inner conductor. If the overlap exceeds the gap size, the outer and inner conductor will be short-circuited. The coarse model parameters are not necessarily physical parameters, but they do need bounds. An impedance for example cannot be negative as this is not practically realisable as was discussed in 2.2. The coarse model parameters are varied within specified limits and extracted when they align the circuit responses at each  $x$  and  $y$  value combination.



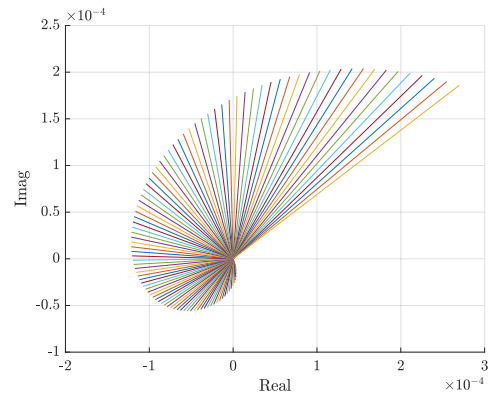
(a) The complex valued response of the coarse (red) and fine (black) models before alignment.



(b) The vector difference between the coarse and fine model responses before alignment.



(c) The complex valued response of the coarse (red) and fine (black) models after alignment.



(d) The vector difference between the coarse and fine model responses after alignment.

Figure 3.22: The alignment step for a single  $x$  and  $y$  parameter value combination. a) Display the imaginary and real parts of the  $S_{11}$  responses for the coarse and fine model before alignment. b) The vector difference between the response in a). The  $L_1$  norm = 42.1664 and the  $L_2$  norm = 4.4526, which is the combined normalised error. In c) the responses are barely distinguishable from each other after alignment. In d) it should be noted that the scale of the vector difference between the model response has been reduced significantly. After alignment the improved error values are  $L_1$  norm = 0.012893, and the final error using norm  $L_2 = 0.0014903$  demonstrates the accuracy of the alignment process.

A mathematical regression model for each coarse model parameter is constructed by fitting a polynomial function through the extracted values. This is visualised in Fig. 3.23

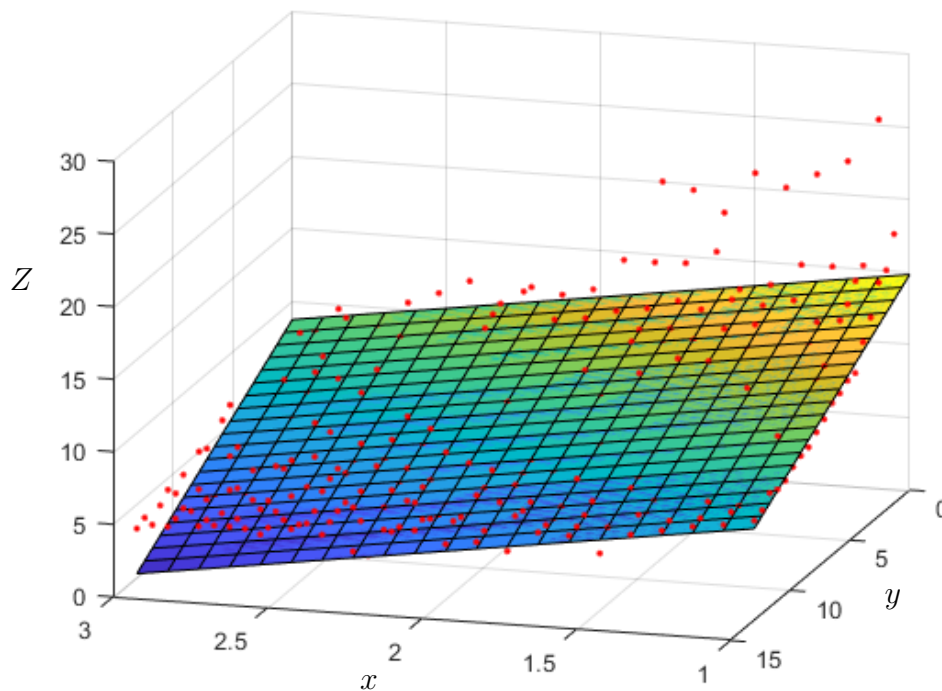


Figure 3.23: A surface fit used to demonstrate how a mathematical function may be used to extract a model for relating peripheral disc parameters to circuit element values. Impedance of a stub-line in this case.

Each disc requires at least two model extractions for either  $Z$  and electrical length or  $L$  and  $C$  values. The models serve as a mere approximation and it may not always be possible to realise the desired values as the current dielectric disc model parameters cannot be varied in a way that allows for tuning each circuit parameter independently.

Typically it is best to use the circuit of Fig. 3.19a as the coarse model, as this is how the circuit is synthesised. The error is generally smaller than when using the alternative approximation of Fig. 3.19b. That being said, the different models lead to different sets of extracted values. In some cases a particular set of extracted values will be more desirable than the other because it would be better suited to the mathematical function fitted to the data. This is the case when aligning the response from the disc at the peripheral port junction. The extracted values from the alignment when using  $LC$  equivalent circuit from Fig. 3.19b yields a data set which is changing unidirectionally, whereas the data from the stub-line circuit tend to be sporadic when used to approximate the disc at the peripheral ports. Fig. 3.24 shows the disc section which accommodates the peripheral port interface. It differs from the other disc implementations in that it does not use spoke-like etched lines. From Table 3.4 it is noted that the required capacitance at this section is much larger than the other section. Also the required inductance is considerably lower than with the other sections. Adding to the demand in low inductance is the extended centre pin of the peripheral SMA connectors. For all of these reasons etched rings are used instead of spoke lines, in order to maximise the realisable capacitance and minimise the inductance at the node.

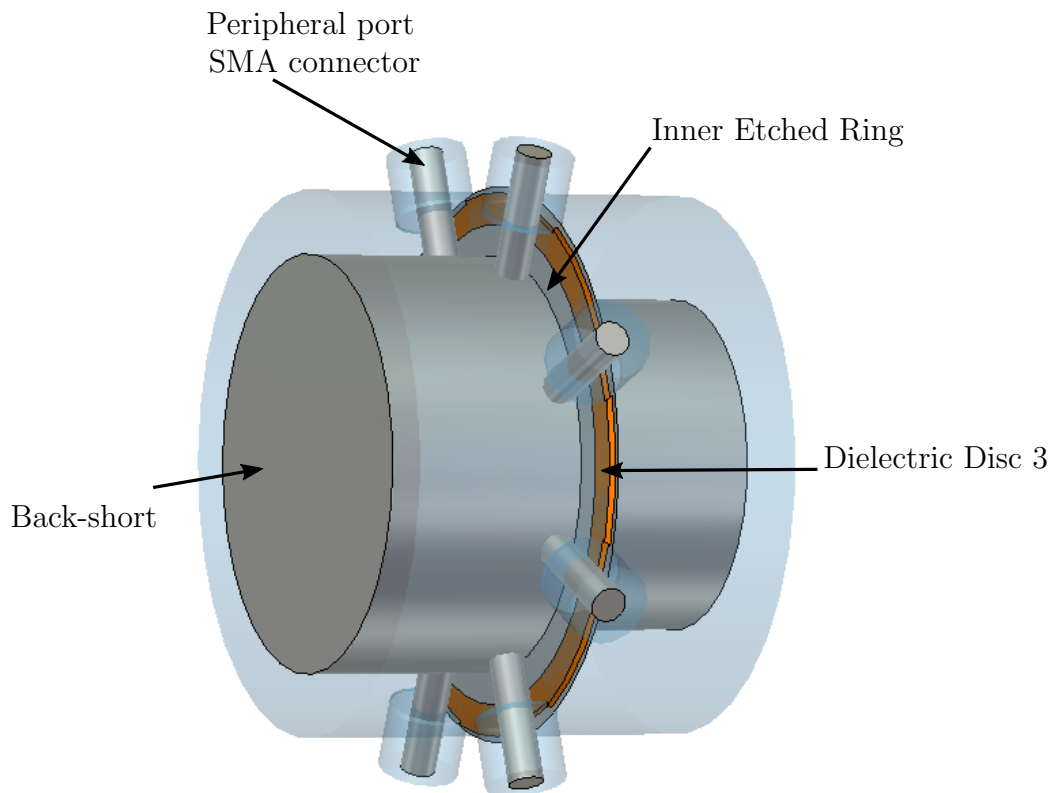


Figure 3.24: Dielectric disc 3 with  $Z_6$ , the back-short joining to its left and  $Z_4$  to its right and SMA connectors on its periphery. The disc at the peripheral has a different configuration to the other discs implemented. Because of this it is often advantageous to use an alternative coarse model that is better suited to mathematical curve fitting.

For extracting the models that relate the disc parameters to circuit elements, simple first order polynomials are used to fit a surface through the extracted values. The equations for impedance  $Z$  and electrical line length  $EL$  are then the linear surface equations given by

$$Z(x, y) = p_{00} + p_{10}x + p_{01}y, \quad (3.3)$$

and

$$EL(x, y) = q_{00} + q_{10}x + q_{01}y. \quad (3.4)$$

The coefficients  $p$  and  $q$  is found by a least squares estimation [48] of the model parameters which is suitable for matrix calculations and therefore easily solved with a MATLAB script. The extracted mathematical models and coefficients approximating the relationship between  $LC$  equivalent branches for each section and the physical parameter is given in Table 3.6. Note the subscripts in the table correspond to the section numbering as before. The extracted polynomials are used in the space mapping optimization of the complete structure. The coarse model input parameters, become the same  $x$  and  $y$  physical parameters used in the fine model. The element values are then evaluated according to the extracted polynomials and used during the alignment and optimisation stages of the space mapping optimisation.

	constant	$x$ -coefficient	$y$ -coefficient
$C_1(x_1, y_1)$	-22.3166	24.3893	6.2875
$L_1(x_1, y_1)$	0.3492	0.0217	-0.1261
$C_3(x_3, y_3)$	-2.9099	2.9792	1.4592
$L_3(x_3, y_3)$	0.2475	-0.0627	-0.0012
$C_5(x_5, y_5)$	0.8909	0.5672	1.7054
$L_5(x_5, y_5)$	0.3885	0.00096	-0.1733

Table 3.6: The extracted polynomials approximating the relationship between the physical parameters of the fine model etched dielectric discs and the equivalent  $LC$  element values of the circuit from Fig. 3.18b.

Each section has two equations in  $x$  and  $y$ . This makes it possible to solve the polynomials simultaneously in terms of  $x$  and  $y$  given the desired  $Z$  and  $EL$  from the synthesis, or equivalently  $L$  and  $C$ . In this way the physical width  $x$  and the dimension for the etched line overlap  $y$  that realise the synthesised element values is approximated. At the very least it provides a relatively good starting point for the space mapping optimisation.

Now that all sections have been modelled they are chained to form the combiner structure shown in Fig. 3.25. A taper can be added and the structure can be optimised to complete the design.

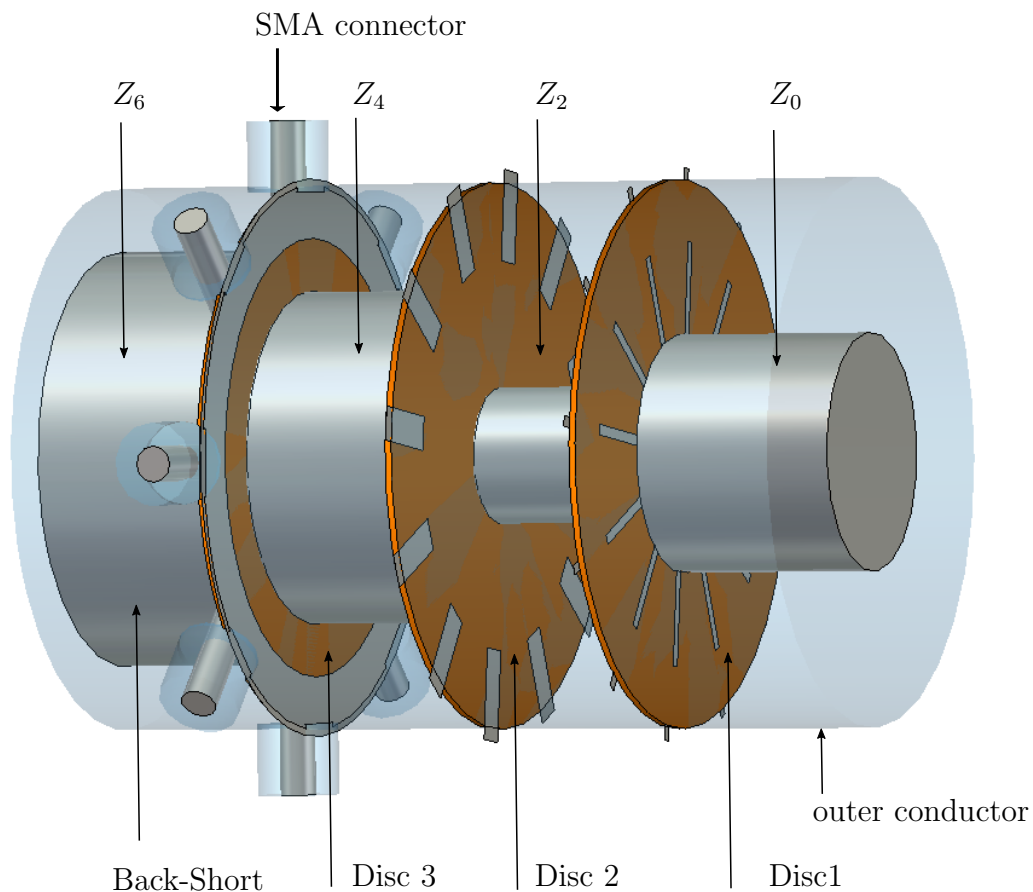


Figure 3.25: The combiner structure form by cascading the individual sections.

### 3.4.4 Central Impedance Tapered Line Transition

The tapered conical line section is done using a simple geometric design that provides a  $50\ \Omega$  constant impedance taper between a  $50\ \Omega$  N-type connector and  $50\ \Omega$  section of the oversized coaxial line. As mentioned in Section 3.3.4, more sophisticated methods of design exist, but for the purpose of the design example the simple geometric design approach will suffice. Fig. 3.26 is used as reference for the calculation of the approximate taper dimensions. The taper length  $l_t$  in the  $z$ -direction from Fig. 3.15 is valid only when section A-B and section A-C in Fig. 3.26 is the same distance, i.e. the start and end of the outer conductor taper coincides in the  $z$ -plane with the start and end of the inner conductor taper. However this is not the case and this scenario. There is an offset between the end of the outer conductor taper at B, and the end of the inner conductor taper at C. The taper length of the inner conductor is denoted  $l_{ti}$  and that the outer conductor as  $l_{to}$ . The  $50\ \Omega$  coaxial line section that is to transition to the N-type connector has an inner conductor radius  $r_1$  and an outer conductor with radius  $r_0$ . The N-type connector dimensions are shown in the figure with  $N_o$  the outer conductor diameter,  $N_i$  the inner conductor diameter and  $N_z$  the length of the conductor. The inner taper angle is numbered  $\theta_i$ , with the outer taper angle given as  $\theta_o$ .

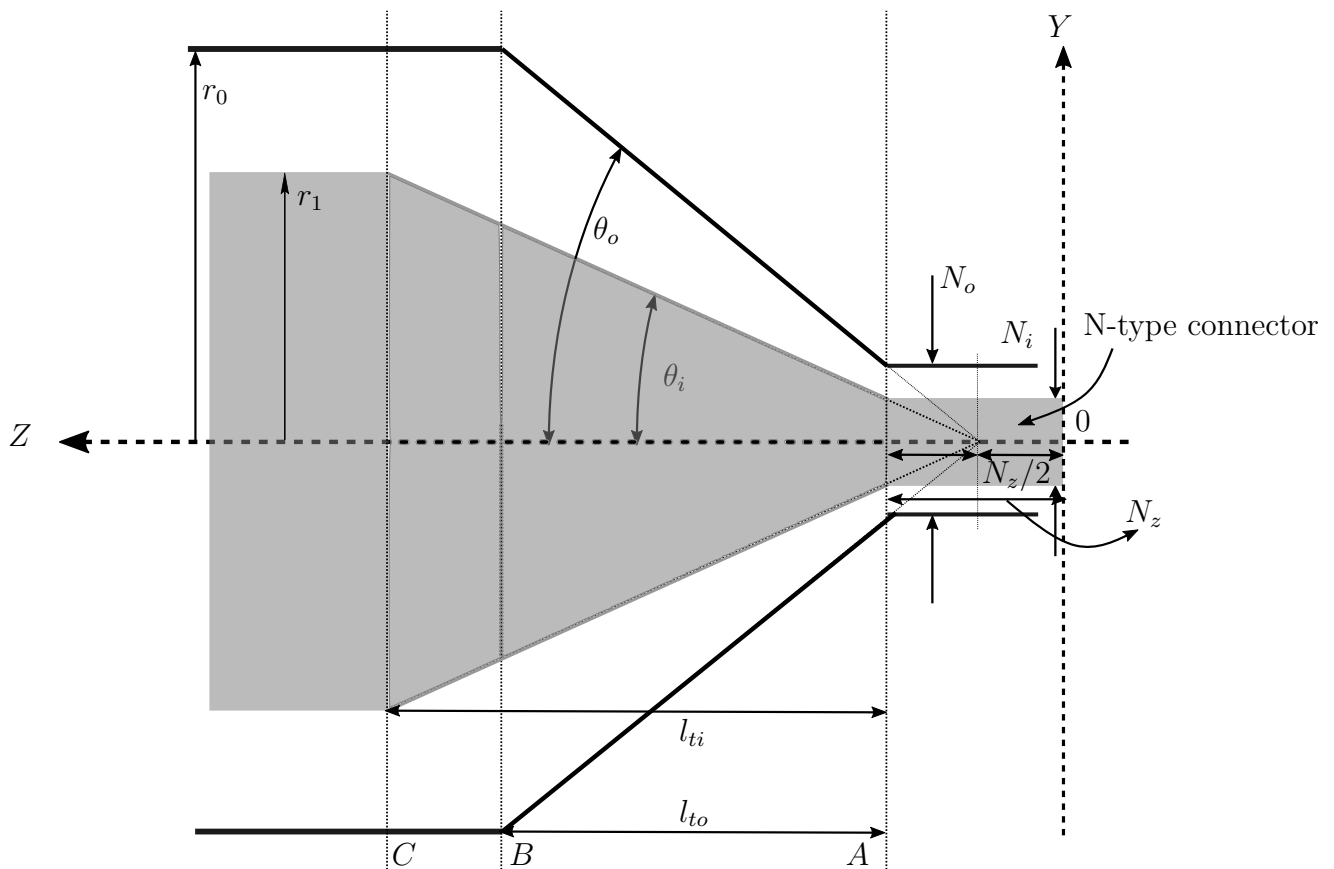


Figure 3.26: A demonstration of a tapered line transition between a coaxial line section and a N-type connector. The figure is not drawn to scale, for the purpose of demonstration.

The taper is symmetrical around the  $z$ -axis. A constant impedance conical line has a point on the  $z$ -axis where the outer conductor and inner conductor would meet if the lines were extended. Placing the face of the N-type connector at the origin choosing this point of



intersection at a distance  $N_z/2$  from the origin, in the centre of the N-type connector the taper outer and inner lines are drawn through the edge of the respective inner and outer conductors of the connector as shown in Fig. 3.26. The inner angle between the  $z$ -axis of symmetry and the inner taper is  $\theta_i$  and  $\theta_o$  is the angle between the axis and the outer taper line. The angles are calculated using simple geometry, with

$$\theta_i = \tan^{-1} \frac{N_i}{N_z} \quad (3.5)$$

and

$$\theta_o = \tan^{-1} \frac{N_o}{N_z}. \quad (3.6)$$

Once the angles are known the taper line lengths,  $l_{ti}$  for the inner conductor taper and  $l_{to}$  for the outer conductor taper can be calculated using

$$l_{ti} = \frac{r_1}{\tan \theta_i} - \frac{N_z}{2} \quad (3.7)$$

and

$$l_{to} = \frac{r_0}{\tan \theta_o} - \frac{N_z}{2}. \quad (3.8)$$

The calculated parameters are listed in Table 3.7 and Fig. 3.27 shows an image of the full combining structure. It is the same structure of Fig. 3.25 with the tapered line transition added to accommodate an N-type connector. With all the combiner parameters calculated the structure is finally optimised using the space mapping framework discussed in Section 3.3.5.

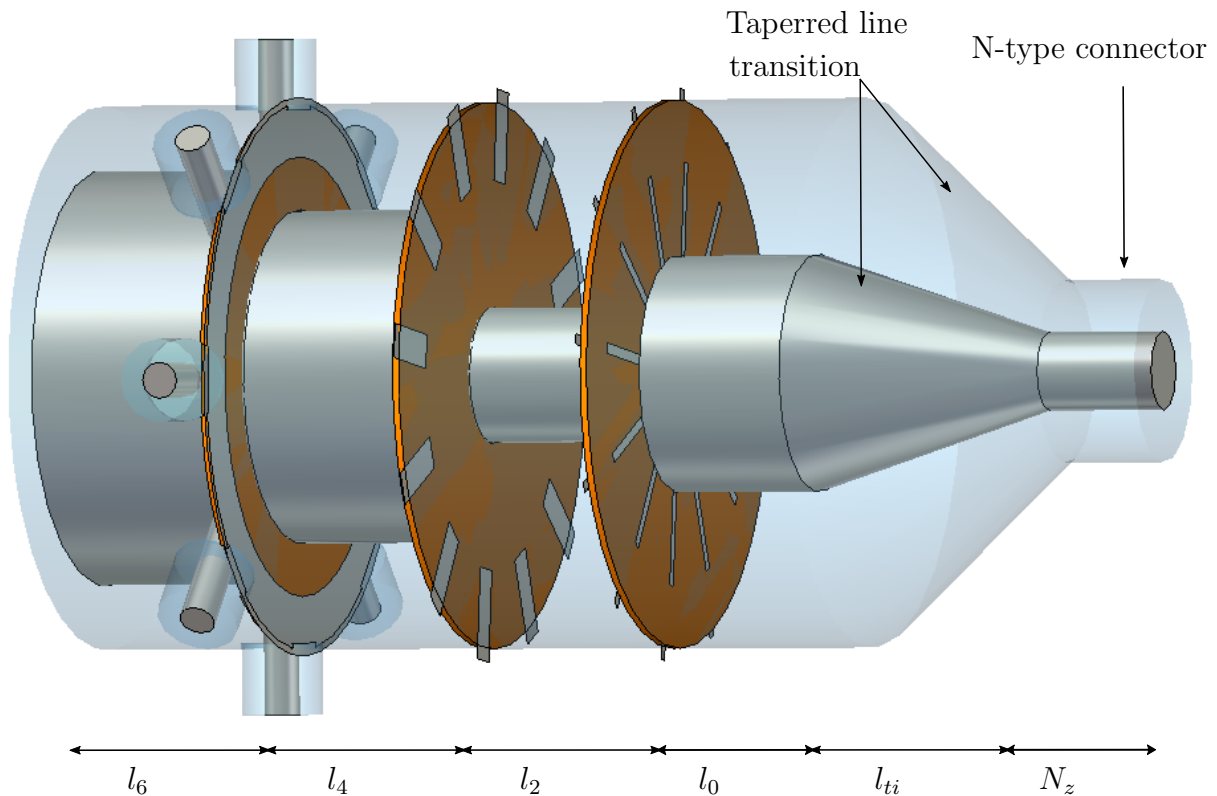


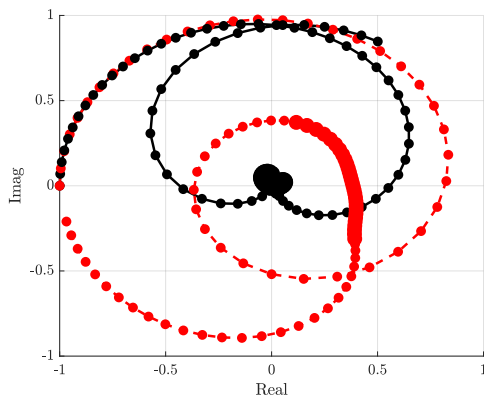
Figure 3.27: The same combiner structure of Fig. 3.25 with a tapered line section to fit an N-type connector. The structure is simulated in CST and optimised using space-mapping.

Parameter	$r_0$	$r_1$	$N_o$	$N_i$	$N_z$	$\theta_o$	$\theta_i$	$l_{to}$	$l_{ti}$
Value	21	9.12	8.03	3.15	9.19	18.92	41.15	19.438	22.017

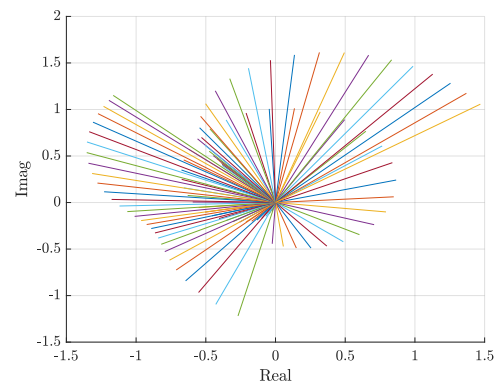
Table 3.7: Calculated parameter values for the tapered line of Fig. 3.26. The dimensions are in millimetres and degrees where appropriate.

### 3.4.5 Space-Mapping Optimisation

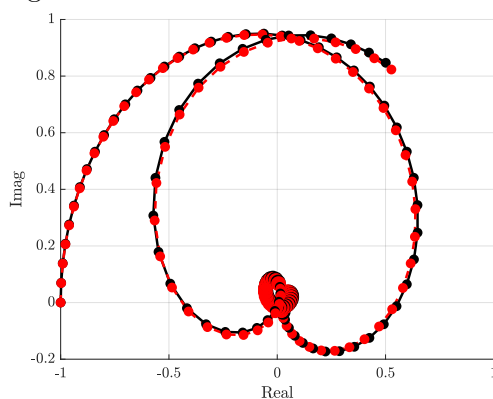
With the full structure assembled, the combiner is ready for optimisation. The individual circuit sections from the model construction are connected together in cascade to form the complete combining structure. As is, with the parameters from the individual sections, typically the combiner response does not compare well with the coarse model response. However the parameters values from each section provide a good initial starting point for the space-mapping framework. The coarse model in this example is the circuit in Fig. 3.18b. The fine model is evaluated and the complex valued response is plotted, together with the coarse model in Fig. 3.28a before the alignment phase occurs.



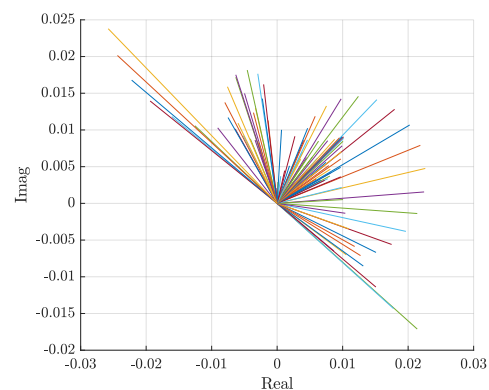
(a) The complex valued response of the coarse (red) and fine (black) models before alignment.



(b) The vector difference between the coarse and fine model responses before alignment.



(c) The complex valued response of the coarse (red) and fine (black) models after alignment.



(d) The vector difference between the coarse and fine model responses after alignment.

Figure 3.28: The  $S_{11}$  complex valued responses and vector differences for the complete combiner structure fine model (black) and the coarse model (red). Plots a) and b) are plotted before alignment. Plots c) and d) are plotted after alignment.

The vector differences between the fine model and coarse model responses are shown in Fig. 3.28b. The  $L_1$  norm is 95.1269 and the  $L_2$  norm is 10.5588. Fig. 3.28c and Fig. 3.28d show the response and vector difference plots after alignment has taken place. Again the complex-valued responses are used as phase is considered it gives the best alignment results. The  $L_1$  norm is reduced to 1.3037 and  $L_2 = 0.14483$ . The reduction in misalignment between the two models demonstrate how essential the space mapping optimisation routine is to the accuracy of the design process.

Once the aligned surrogate model is obtained, it is optimised. The optimisation algorithm is restricted to change the model's circuit element values according to the extracted mathematical relationships within a specified range of the physical parameters. The parameters to be optimised may include any of the dielectric disc parameters or physical dimensions of the coaxial combiners. The boundaries for the optimisation parameters need to be carefully considered. When values are inserted into the mathematical models it is possible that negative valued results are obtained for impedances. The coarse model solver will immediately terminate in an error and the optimisation will not complete. Limiting the allowable range for the input parameters to the range of values over which each disc model was extracted will help to avoid such errors from occurring.

Table 3.8 list the simplest optimisation parameters for a 6th order filter. The table displays the lower bound, the starting value, the upper bound and the optimised values for the combiner design. All eleven parameters need to be optimised at the same time during full wave simulation, demonstrating the complexity of the optimisation problem. This demonstrates how essential the space-mapping framework is to the optimisation of the design.

Parameter	$x_1$	$y_1$	$x_2$	$y_2$	$x_3$	$y_3$	$l_0$	$l_2$	$l_4$	$l_6$	$l_{ti}$
Lower	0.0	0.0	0.0	0.0	0.0	0.0	12.5	12.5	12.5	10	15.63
Start	1.0	3.25	2.6	4.0	0.8	2.5	15.63	15.63	15.63	15.63	23.44
Upper	4.0	4.5	4.0	7.5	4.0	11.0	18.75	18.75	18.75	25	0
Optimised	0.8	2.6	2.6	4.1	0	3.35	11.29	15.63	15.63	15.63	18.64

Table 3.8: Parameters to be optimised simultaneously. The lower bound, starting value, upper bound and optimised value for each parameter is given. The range of values demonstrate the complexity of the optimisation problem at hand.

After the surrogate has been optimised, the fine model is evaluated at the same point. If the termination condition is not met, the surrogate model is updated and again aligned. The process flow follows that shown in Fig. 3.17 until the termination condition is met. The optimiser goal specified in this example is a minimum  $S_{11}$  response over the specified bandwidth from 0.9 GHz to 1.5 GHz. Fig. 3.29 show the  $S_{11}$  responses for the different models.

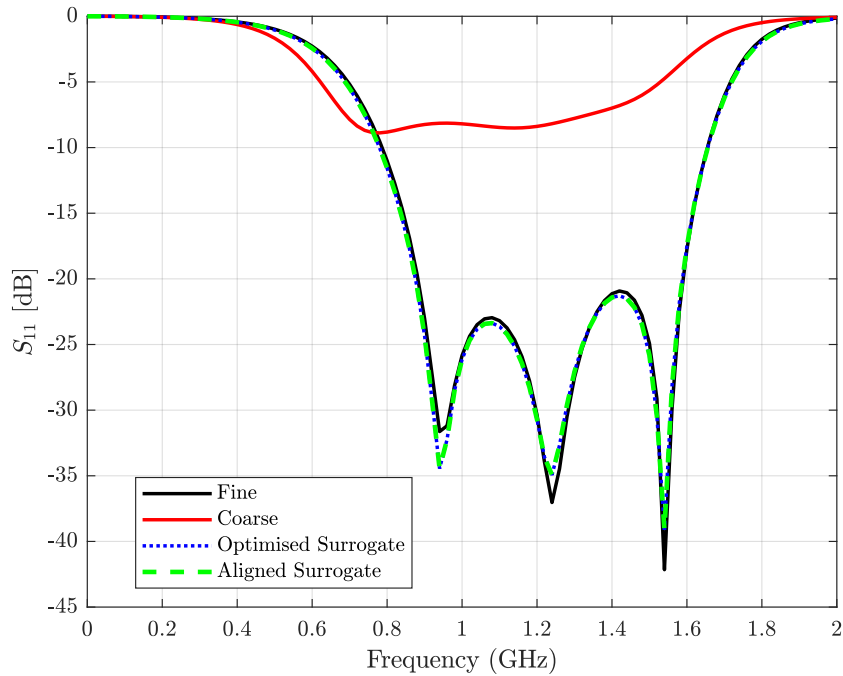


Figure 3.29: The  $S_{11}$  responses from the different models in the space mapping optimisation routine. The optimised response in this example was found with two iterations.

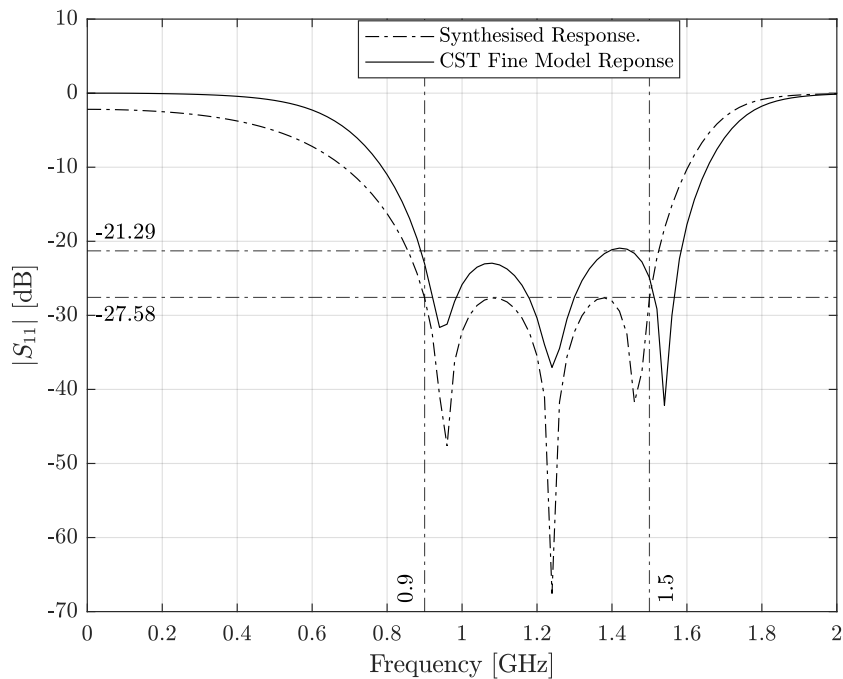


Figure 3.30: The  $S_{11}$  responses from the different models in the space mapping optimisation routine.

In this example the fine model response meet the specified optimisation goal after one iteration and the optimisation is finished. This is not always the case. Often a few iter-

ations and fine model evaluations are required before the termination criteria is reached. Fig. 3.30 show for comparison the synthesised circuit response and the optimised fine model response. The fine model response has a 58% bandwidth from 0.9 GHz to 1.6 GHz with a  $S_{11} \leq 21.2$  dB across the passband.

The total length  $l_T$  of the combiner, after optimisation, is 85.94 mm. That is approximately  $0.344\lambda$  at the operating frequency of 1.2 GHz or  $0.258\lambda$  at the lowest passband frequency of 900 MHz. If all line section were to be constructed using classic quarter-wave line sections, the structure length would be at least  $0.75\lambda$  at the lowest passband. This design has demonstrated how the integration of a short-step filter is capable of significantly reducing the length of power combiners.

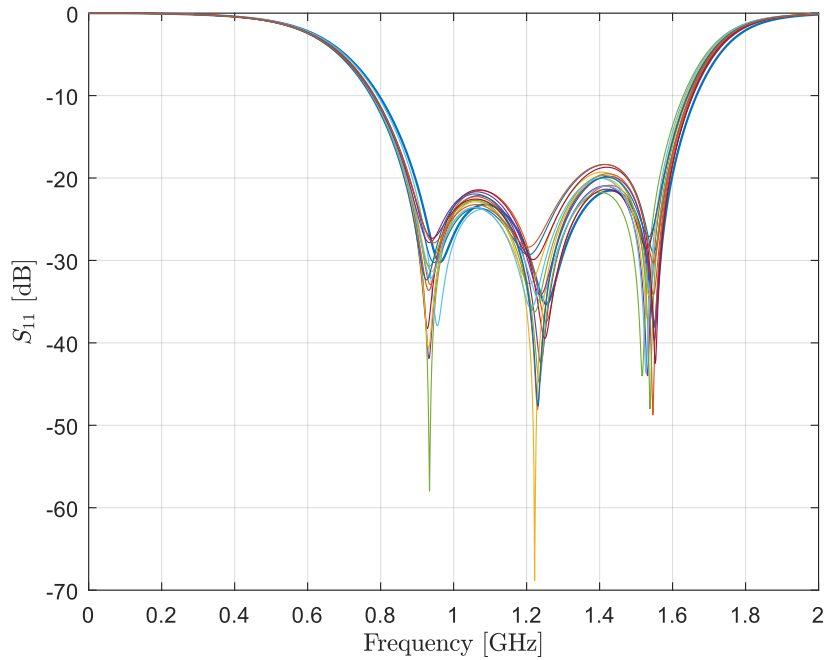
The design steps are summarised as follows:

1. Start by specifying bandwidth, operating frequency and the number of peripheral ports.
2. Choose the connector types for the central port and the peripheral ports.
3. Synthesise a short-step filter with the given specifications and find the equivalent  $LC$  branches.
4. From (1) choose  $r_0$  to accommodate  $N$  ports taking into account cut-off frequency of higher-order modes for operating frequency.
5. From  $r_0$  calculate all  $r_i$
6. Choose a substrate for the discs:
  - Higher  $\epsilon$  can realise more capacitance.
  - Choose fixed thickness  $d$  for all discs to limit the optimisation parameters.
  - Choose the thickness  $d$  to be an industry standard. Choose small  $d$  to realize more capacitance.
7. Construct the individual 3D models and extract the mathematical models for each. Individual parts can be cascaded to form the completed structure by essentially multiplying ABCD matrices.
8. Construct the full combiner structure by connecting the individual section in cascade.
9. Add a tapered line section to transition from the coaxial line to a standard type connector.
10. Optimise the structure using a space-mapping framework.

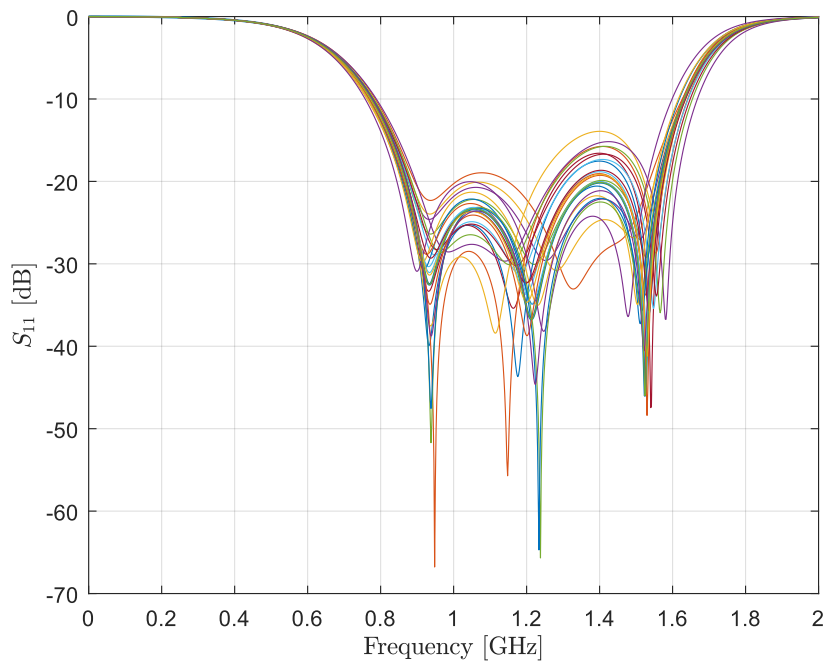
### 3.4.6 Physical Construction

Before the simulated results are discussed, it may be a suitable point for a brief discussion on the possible physical construction of the device and the process tolerances involved. Recent power combiners from literature mostly make use of computer numerical control (CNC)-lathes to machine the transmission lines of the combining structure with high precision. Typical materials used are Aluminium or Brass for which a typical modern lathes have tolerances as small as 0.13 mm [49]. Higher precision is possible with sophisticated machinery, but will cost more.

Printed circuit board (PCB) manufacturing processes are reporting etching tolerance standards of 100  $\mu\text{m}$  and experimental tolerances of 75  $\mu\text{m}$ , with the same dimensions listed for inter line spacings [50]. Using the maximum tolerance values, the each of the optimised design parameters are offset and simulated again. Fig 3.31 shows the effect of manufacturing tolerances, with worst case scenario offsets on all parameters, on the fine model circuit  $S_{11}$  response. From the spread in the  $S_{11}$  response plots, it is evident that, even with the given manufacturing tolerances it should be possible to build a circuit with a response reasonably close to the simulated results.



(a)  $S_{11}$  circuit response for optimised transmission line dimensions offset by CNC tolerances.



(b)  $S_{11}$  circuit response for disc parameter dimensions offset by PCB etching tolerances.

Figure 3.31: The optimised  $S_{11}$  response of the circuit from the design example, with the disc and transmission line parameters offset with manufacturing tolerances. a) The effect of CNC machining tolerances. b) The effect of PCB etching process tolerances.

### 3.5 Higher Order Example Designs

The example of the previous section demonstrated a compact power combiner design with 50% bandwidth, with an integrated 6th order short-step filter. Using the same design approach the bandwidth could possibly be increased by synthesising higher order filters that may be integrated into the combining structure. This will increase the bandwidth, as was shown in Fig. 3.18, at the cost of the reflection coefficient performance as well as added length to the combining structure. By using higher order filters there is also added complexity to the design. An extra transmission line section and dielectric disc is added with every step in the even-ordered filter. This section provides the summarised results of the 8-way combiner with an 6th order Chebyshev short-step impedance transformer from the previous example, and also three additional 8-way combiners. One with an 8th order short-step filter and another with a 10th order short-step impedance transformer integrated into the combining structure. A 12th order filter synthesis is also shown but not included in a power combiner design.

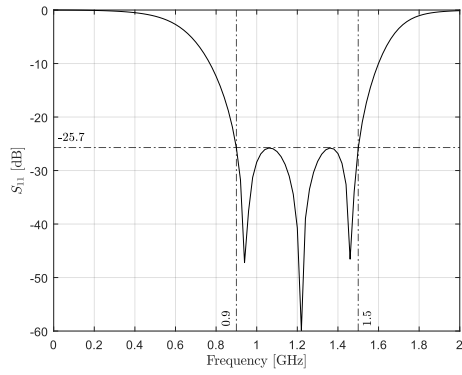
The initial design parameters are very similar or exactly the same in each case as all designs are for 8-way combiners. The central port connector is a  $50\ \Omega$  N-type female. The peripheral port connectors are  $50\ \Omega$  SMA connectors. The equivalent impedance of the peripheral ports are  $6.25\ \Omega$ . All dielectric discs are simulated with Rogers R03003 substrate with thickness  $d = 0.508\ \text{mm}$  and dielectric constant  $\epsilon = 3.0$ . The synthesised bandwidths, reflection coefficients and circuit elements are summarised for the additional designs. Note all line lengths are again synthesised with  $\lambda/16$  sections. Some of the results for the 6th order filter are reproduced for the sake of convenience.

#### Synthesised Parameters

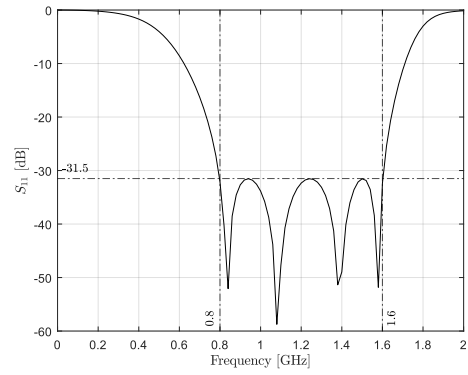
Filter	Synthesised Parameters [ $\Omega$ ]											
Order	$Z_1$	$Z_2$	$Z_3$	$Z_4$	$Z_5$	$Z_6$	$Z_7$	$Z_8$	$Z_9$	$Z_{10}$	$Z_{11}$	$Z_{12}$
6	17.81	83.13	4.84	29.39	2.23	16.07						
8	26.55	102.4	9.34	62.24	4.22	24.35	3.32	27.00				
10	28.79	101.4	11.86	75.73	6.78	42.51	3.74	20.13	3.60	34.25		
12	29.88	99.47	13.47	81.98	8.56	54.84	5.55	32.90	3.46	17.83	3.74	40.99

Table 3.9: Synthesised results for different orders of short-step filters. The element values shown are scaled to a  $50\ \Omega$  central port impedance.

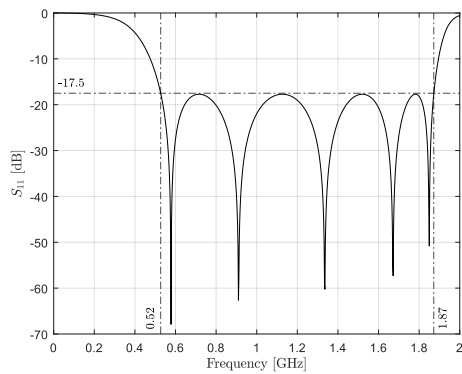




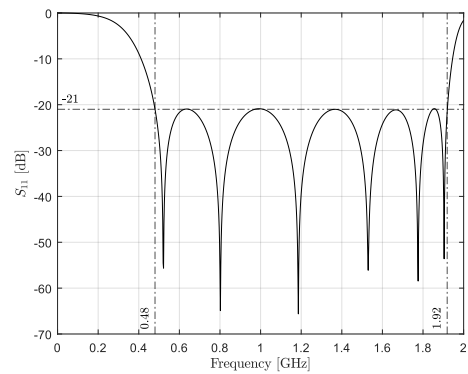
(a) 6th Order short-step transformer with a bandwidth of 50%



(b) 8th Order short-step transformer with a bandwidth of 67%.



(c) 10th Order short-step transformer with a bandwidth of 112%.



(d) 12th Order short-step transformer with a bandwidth of 120%.

Figure 3.32: The  $S_{11}$  response of a) a 6th order filter, b) a 8th order filter, c) a 10th order filter and d) a 12th order filter.

### Physical Parameters

The calculated and optimised physical parameters for the different combiners are listed in the tables below. The coaxial line segments radii and physical lengths are summarised in Table 3.10 and Table 3.11 respectively. Table 3.12 contains the physical dimensions of the etched lines on the dielectric discs.

Combiner	Radii of coaxial line segments [mm]						
Order	$r_0$	$r_1$	$r_2$	$r_3$	$r_4$	$r_5$	$r_6$
6	21.0	9.12	5.25	12.86	16.06		
8	21.0	9.12	3.80	7.44	13.99	13.39	
10	21.0	9.12	4.49	6.99	11.25	15.40	12.60

Table 3.10: Calculated radii of the coaxial line segments for the different combiners with impedances from Table 3.9.

Combiner	Optimised lengths of coaxial line segments [mm]								
Order	$l_0$	$l_2$	$l_4$	$l_6$	$l_8$	$l_{10}$	$l_{ti}$	$l_{to}$	$l_T$
6	11.29	15.625	15.625	15.625			18.636	15.625	85.94
8	15.72	15.74	15.71	15.78	15.62		27.77	23.44	106.34
10	12.14	16.04	15.07	15.49	14.99	19.06	23.14	19.53	125.07

Table 3.11: Lengths of the coaxial line segments and tapered line and also the total combiner length of the different combiners, after optimisation.

Combiner	Optimised disc parameters [mm]									
Order	$x_1$	$y_1$	$x_3$	$y_3$	$x_5$	$y_5$	$x_7$	$y_7$	$x_9$	$y_9$
6	0.8	2.60	2.60	4.10		3.35				
8	0.71	5.53	1.88	2.71	2.27	5.48		2.42		
10	0.19	3.99	1.95	2.05	2.56	3.17	3.95	4.85		1.00

Table 3.12: The optimised physical parameters of the dielectric discs with etched lines.

### Response Parameters

The optimised response parameters are summarised for the 8th and 10th order combiners. The mathematical models for the discs of the 8th order combiner are listed in Table 3.13 and for the 10th order in Table 3.14. Fig. 3.33 displays the responses of the different models within the space-mapping routine at each iteration of the optimisation for the 8th order combiner. Similarly Fig. 3.35 shows the responses of the 10th order combiner at each iteration during the optimisation.

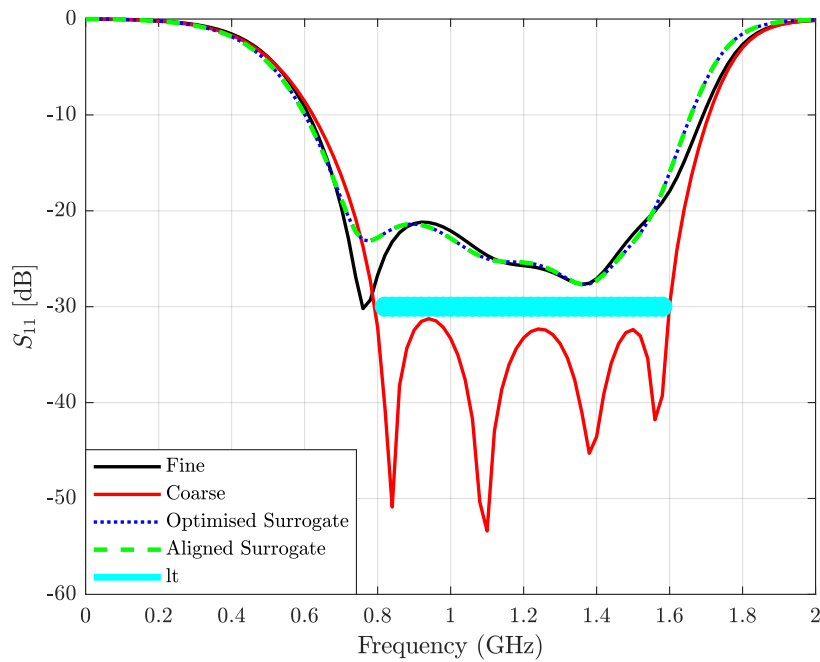
8th Order	constant	$x$ -coefficient	$y$ -coefficient
$Z_1(x_1, y_1)$	35.3791	-26.7090	-1.2775
$EL_1(x_1, y_1)$	11.6832	105677	1.7733
$Z_3(x_3, y_3)$	16.2511	-0.1190	-2.5167
$EL_3(x_3, y_3)$	4.7763	8.9490	0.3270
$Z_5(x_5, y_5)$	12.1450	-1.8699	-0.6196
$EL_5(x_5, y_5)$	15.2844	-0.0439	1.3039
$C_7(x_7, y_7)$	3.506	0	5.133
$L_7(x_7, y_7)$	0.0953	0	-0.02

Table 3.13: The extracted polynomials approximating the relationship between the physical parameters of the fine model etched dielectric discs and the element values of the 8th order filter.

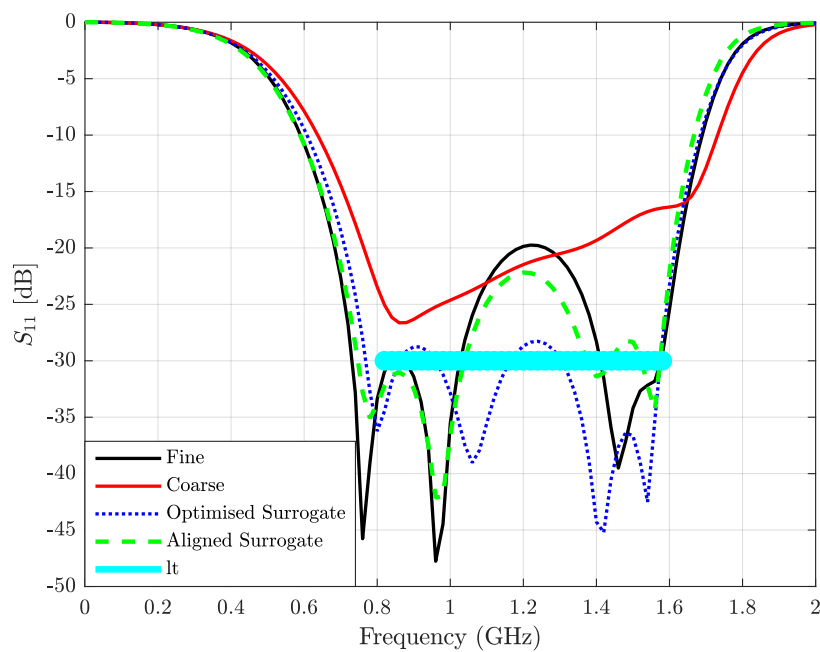
10th Order	constant	$x$ -coefficient	$y$ -coefficient
$Z_1(x_1, y_1)$	39.5781	-29.6349	-1.7885
$EL_1(x_1, y_1)$	11.3449	9.4209	1.8879
$Z_3(x_3, y_3)$	26.0009	-5.5288	-2.2269
$EL_3(x_3, y_3)$	19.7286	-1.3775	2.2239
$Z_5(x_3, y_3)$	12.7355	-2.3210	-0.3728
$EL_5(x_5, y_5)$	11.1936	0.1242	2.9306
$Z_7(x_7, y_7)$	10.4316	-0.7836	-0.6345
$EL_7(x_7, y_7)$	20.2826	-0.8026	1.1313
$C_9(x_9, y_9)$	5.229	0	5.736
$L_9(x_9, y_9)$	0.02607	0	0.001224

Table 3.14: The extracted polynomials approximating the relationship between the physical parameters of the fine model etched dielectric discs and the element values of the 10th order filter.

## 8th Order, 8-way Combiner



(a) 1st iteration of the space-mapping optimisation.



(b) 2nd and final iteration of the optimisation.

Figure 3.33: The different model responses at the a) 1st iteration and b) final iteration of the space-mapping optimisation. The optimised responses are for the 8th order combiner.

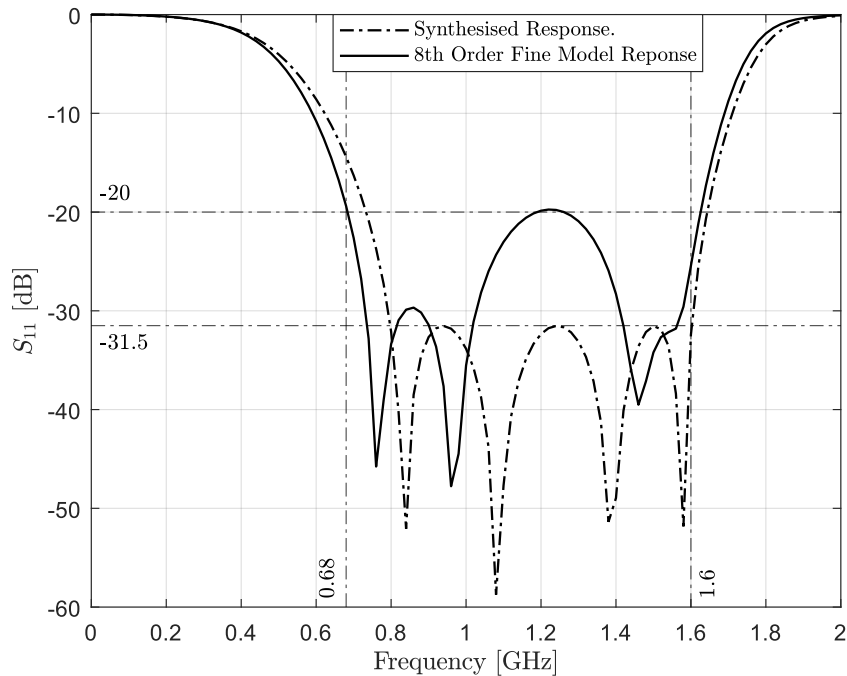
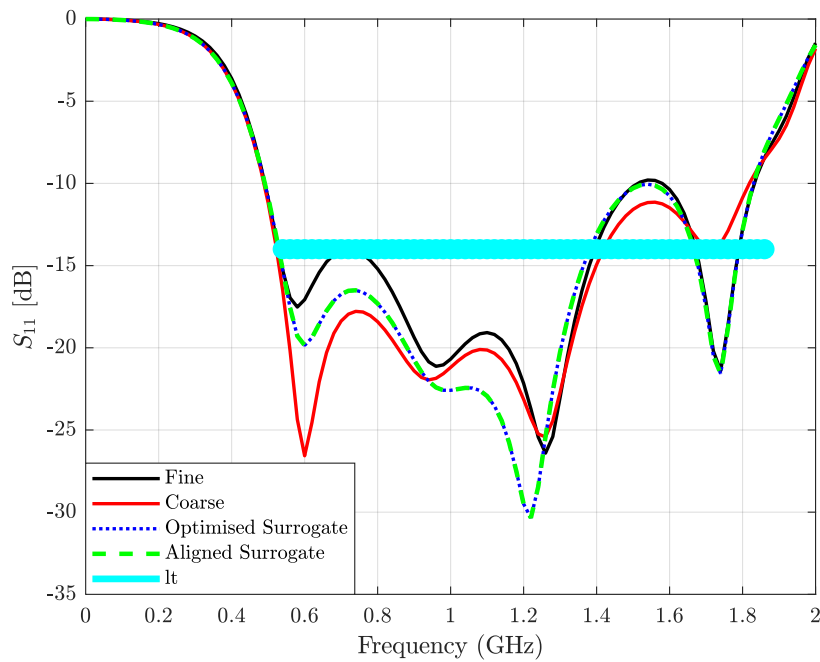


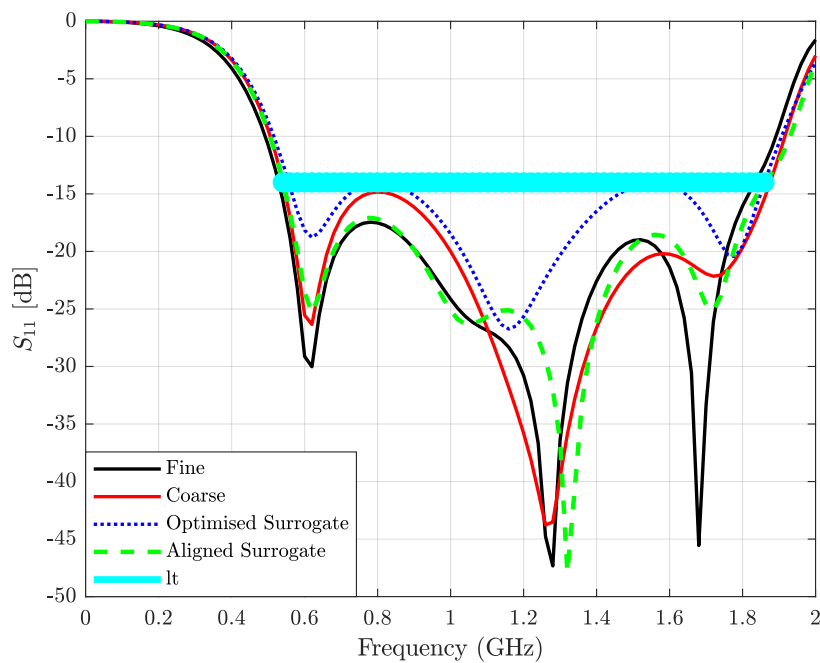
Figure 3.34: The  $S_{11}$  response of the synthesised 8th order filter compared with the optimised response of the compact 8-way combiner incorporating the filter. The optimised fine model response displays  $S_{11} \leq -20$  dB over a bandwidth of 76%.

From Fig. 3.34 above it is observed that the 8th order, 8-way combiner has a reflection coefficient better than  $-20$  dB over a 76% bandwidth. The bandwidth is slightly larger than designed for and the maximum passband ripple is much larger than that of the synthesised circuit response. The discrepancies in the synthesised circuit response and that of the optimised fine model is expected. As mentioned earlier, the synthesised response may be considered as an ideal, as it is simulated using ideal circuit elements and have less complexity compared the CST 3D combiner model. Even though the reflection coefficient of the combiner circuit has a worse performance than the synthesised circuit, it would still be sufficient to use as  $-20$  dB equates to a very small reflected signal. The main advantage of combiner is its compact size. With a total length of 106.34 mm the circuit measures in wavelength approximately  $0.425\lambda$  at the operating frequency. The overall reduction in size is significant compared to combiner utilising classic quarter-wave transformers, and is especially useful at microwave frequencies as low as 1.2 GHz.

## 10th Order, 8-way Combiner



(a) 1st iteration of the space-mapping optimisation.



(b) 2nd and final iteration of the optimisation.

Figure 3.35: The different model responses at the a) 1st iteration and b) final iteration of the space-mapping optimisation. The optimised responses are for the 10th order combiner.

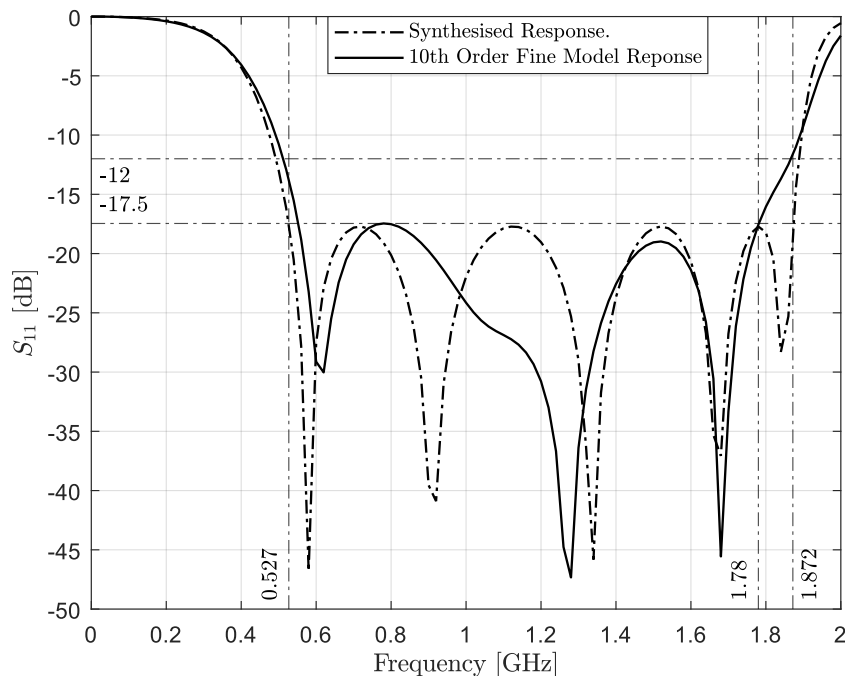


Figure 3.36: The  $S_{11}$  response of the synthesised 10th order filter compared with the optimised response of the compact 8-way combiner incorporating the filter. The optimised fine model response displays a  $S_{11} \leq -17.5$  dB over an approximate bandwidth of 104%. The figure also shows the circuit response has a bandwidth of 112% for  $S_{11} \leq -12$  dB for comparison with [15].

The optimised response of a combiner incorporating a 10th order short-step impedance transformer is shown in Fig. 3.36 above. For comparison the synthesised circuit response is also shown. The combiner response has a maximum passband ripple of  $-17.5$  dB over a bandwidth of 104%. This is in good comparison with the synthesised circuit although the bandwidth is about 8% less.

The 8-way combiner from [15], operates at a centre frequency of 1.2 GHz and reports a return loss of greater than 12 dB over a total bandwidth of 112% from 0.52 GHz to 1.86 GHz. It has a total size of  $0.75\lambda \times 0.25\lambda \times 0.25\lambda$  at the lower edge of the passband. The combiners total length, not taking into account the central 7/16 connector is 436 mm. The comparison between the 10th order compact combiner from this report and the combiner from [15] is a suitable one as both are coaxial combiners designed to operate at a centre frequency of 1.2 GHz. The optimised 10th order combiner shows excellent comparison in terms of bandwidth and reflection coefficient performance. Fig. 3.36 shows that the compact combiner also has a 112% bandwidth when measured at a return loss of greater than or equal to 12 dB but the size of the combiner is significantly smaller than that of [15]. With a total length of 125.07 mm the combiner is only  $0.5\lambda$  of the centre frequency of operation and approximately  $0.22\lambda$  at the lower passband frequency, compared to  $0.75\lambda$  from literature.

Combiner	$S_{11}$ [dB]	Bandwidth	$f_c$ [GHz]	Rel. Length	Abs. Length [mm]
10th Order Simulated	-12	112%	1.2	$0.5\lambda$	126 mm
Combiner from [15]	-12	112%	1.2	$1.7\lambda$	436 mm

Table 3.15: Comparison between the 10th Order simulated compact combiner and the combiner from [15].

This section has provided the simulated design results of three different 8-way coaxial combiners, each incorporating a synthesised short-step Chebyshev impedance transformer, with increasing even order. These results have demonstrated how the combiners are reduced in size while maintaining performance characteristics which compare well with similar combiner designs from literature.



# Chapter 4

## Conclusion

The length of coaxial combiners is significantly reduced by integrating a short-step-stub Chebyshev impedance transformer into the design. The advantages for combiners operating at lower microwave frequencies are demonstrated. Complete designs for three different reactive 8-way compact coaxial power combiners are presented. A compact combiner, incorporating a short-step Chebyshev impedance transformer is compared to a similar design from literature and displays excellent passband performance characteristics. The main goal of reducing the size of the combiner is achieved and demonstrated several times within the report, through design examples and with a comparison to literature.

A comprehensive discussion on the theory required for network synthesis, and short-step stub Chebyshev impedance transformers is presented in Chapter 2. Starting with the theory of network analysis, the different sets of parameters used to describe passive, reactive circuits are given. The realisability conditions in terms of the circuit parameters is discussed and the canonical as well as non-canonical circuit implementations are given. The short-step-stub Chebyshev impedance transformer and its design methodology is thoroughly discussed. A MATLAB script for synthesising even-order bandpass filter circuits for a specified bandwidth and for extracting elements values is developed and used to demonstrate the design of such circuits.

In Chapter 3 the initial design considerations for power combiners utilising short-step filters are presented. The geometry of coaxial combiners and a method for implementing a shunt-stub line within a coaxial transmission line is introduced. A method for extracting and mathematically relating equivalent circuit models to the physical combiner parameters is given and demonstrated after a discussion on surrogate modelling using a space-mapping optimisation framework. The comprehensive design example at the end of the chapter serves as a demonstration for designing any  $N$ -way compact coaxial combiner.

The results for a 6th order, an 8th order and a 10th order coaxial 8-way combiner operating at a centre frequency of 1.2 GHz are presented. The combiner incorporating a 10th order short-step impedance transformer displays a 112% bandwidth simulated at a return loss of greater than 12 dB. The main advantage of the combiner is the overall small size, with a total length, including the central port N-type connector, of 125.07 mm at a centre operating frequency of 1.2 GHz. These results are compared with a combiner from literature with a similar configuration and operating specifications. The design displays a return loss of greater than 12 dB over a bandwidth of 112%. The total length of the combiner, without the 7/16 central port connector, is 436 mm. The significant advantage

in size for the combiner of this report, incorporating a short-step impedance transformer, is demonstrated via the comparison above. The comparison however, does not include power handling capabilities and is only valid for the simulated results in this report as no circuit was constructed there are no measured values to compare.

The apparent discrepancies between the response of synthesised circuits and optimised high-fidelity CST models leads to several recommendations for possible future considerations:

- The optimisation results may be improved by improving the the mathematical relationship between circuit element values and physical parameters. This could be achieved in several ways:
  - By finding a configuration for the dielectric disc that better approximates the synthesised shunt elements.
  - By finding a disc configuration that, to a larger extent, is capable of tuning the circuit parameters, such as  $L$  and  $C$  values, independently.
  - By extracting mathematical models that more accurately describe the behaviour the the high-fidelity model. This could be done by increasing the order of polynomials used to fit the data, once the configuration is updated to more closely resemble the element models.
- Prototypes of the dielectric disc with etched lines could be constructed, measured and compared with the simulation results in order to ascertain whether there is anything that disqualifies the disc as a feasible realisation of the shunt elements.
- The power handling capability should be investigated to see whether the dielectric disc implementation impose any restrictions on the peak power handling before breakdown occurs.
- By designing more sophisticated central port to coaxial combiner transitions, like those from [40–42], the tapered line section could possibly be shortened, or designed to increase the operating bandwidth and maximum power handling.
- The peripheral port transition could be improved by redesigning the disc configuration to a better approximation of the circuit model. This could lead to improved model alignment, optimisation and circuit performance in terms of bandwidth and return loss. Isolation between the peripheral ports could also be taken into account, and using a multi-layer PCB, an isolation circuit could possibly be incorporated, given electric breakdown does not become a problem.

# Bibliography

- [1] R. D. Beyers and D. I. L. De Villiers, "Design of axially symmetric power combiners using surrogate based optimization," in *VII European Congress on Computational Methods in Applied Sciences and Engineering (ECCOMAS)*, 2016, pp. 4339–4350.
- [2] P. W. van der Walt, "Short-step-stub Chebyshev impedance transformers," *IEEE Transactions on Microwave Theory and Techniques*, vol. 34, no. 8, pp. 863–868, 1986.
- [3] K. Kanto, A. Satomi, Y. Asahi, Y. Kashiwabara, K. Matsushita, and K. Takagi, "An X-band 250W solid-state power amplifier using GaN power HEMTs," *2008 IEEE Radio and Wireless Symposium, RWS*, pp. 77–80, 2008.
- [4] K. Takagi, Y. Kashiwabara, K. Masuda, K. Matsushita, H. Sakurai, K. Onodera, H. Kawasaki, Y. Takada, and K. Tsuda, "Ku-band AlGaIn/GaN HEMT with over 30W," in *2007 European Microwave Integrated Circuit Conference*, 2007, pp. 169–172.
- [5] H. Shigematsu, Y. Inoue, A. Akasegawa, M. Yamada, S. Masuda, Y. Kamada, A. Yamada, M. Kanamura, T. Ohki, K. Makiyama, N. Okamoto, K. Imanishi, T. Kikkawa, K. Joshin, and N. Hara, "C-band 340-W and X-band 100-W GaN power amplifiers with over 50-% PAE," *IEEE MTT-S International Microwave Symposium Digest*, pp. 1265–1268, 2009.
- [6] M. Nishihara, T. Yamamoto, S. Mizuno, S. Sano, and Y. Hasegawa, "X-band 200W AlGaIn/GaN HEMT for high power application," *European Microwave Week 2011: "Wave to the Future", EuMW 2011, Conference Proceedings - 6th European Microwave Integrated Circuit Conference, EuMIC 2011*, no. October, pp. 65–68, 2011.
- [7] H. Ashoka, J. Ness, A. Robinson, M. Gourlay, J. Logan, P. Woodhead, and D. Reuther, "X-band 2 kW CW GaAs FET power amplifier for continuous wave illuminator application," *IEEE MTT-S International Microwave Symposium Digest*, vol. 2, pp. 1149–1152, 1998.
- [8] R. A. York, "Some considerations for optimal efficiency and low noise in large power combiners," *IEEE Transactions on Microwave Theory and Techniques*, vol. 49, no. 8, pp. 1477–1482, 2001.
- [9] K. J. Russell, "Microwave power combining techniques," *IEEE Transactions on Microwave Theory and Techniques*, vol. 27, no. 5, pp. 472–478, 1979.
- [10] R. A. York, "Some considerations for optimal efficiency and low noise in large power combiners," *IEEE Transactions on Microwave Theory and Techniques*, vol. 49, no. 8, pp. 1477–1482, 2001.

- [11] M. E. Bialkowski and V. P. Waris, "Electromagnetic model of a planar radial-waveguide divider/combiner incorporating probes," *IEEE Transactions on Microwave Theory and Techniques*, vol. 41, no. 6, pp. 1126–1134, 1993.
- [12] T. Hsu and M. D. Simonutti, "A wideband 60 GHz 16-way power divider/combiner network," in *1984 IEEE MTT-S International Microwave Symposium Digest*, 1984, pp. 175–177.
- [13] Q. Xue, K. Song, and C. H. Chan, "China: Power combiners/dividers," *IEEE Microwave Magazine*, vol. 12, no. 3, pp. 96–106, 2011.
- [14] R. Lehmensiek and P. W. van der Walt, "A compact, high-power, low-loss, L-band coaxial 18-way power divider/combiner," *Microwave and Optical Technology Letters*, vol. 16, no. 4, pp. 241–243, 1997.
- [15] M. Amjadi and E. Jafari, "Design of a broadband eight-way coaxial waveguide power combiner," *IEEE Transactions on Microwave Theory and Techniques*, vol. 60, no. 1, pp. 39–45, 2012.
- [16] J. W. Gabor C. Temes, *Introduction to Circuit Synthesis and Design*, 1st ed. McGraw-Hill Book Company, 1977.
- [17] D. C. Giancoli, *Physics - Principles with Applications*, 6th ed., 2005.
- [18] D. M. Pozar, *Microwave Engineering*, 4th ed. Wiley, 2012.
- [19] O. Brune, "Synthesis of a finite two-terminal network whose driving-point impedance is a prescribed function of frequency," *MIT Journal of Mathematics and Physics*, vol. 10, pp. 191–236, 1931.
- [20] D. Richard and R. Bott, "Impedance synthesis without the use of transformers," *Journal of Applied Physics*, no. 20, p. 816.
- [21] M. Tyaglov, "Generalized Hurwitz polynomials," *Arxiv preprint arXiv:1005.3032*, pp. 1–59, 2010. [Online]. Available: <http://arxiv.org/abs/1005.3032>
- [22] R. Levy, "A new class of distributed prototype filters with applications to mixed lumped/distributed component design," *IEEE Transactions on Microwave Theory and Techniques*, vol. 18, no. 12, pp. 1064–1071, 1970.
- [23] G. C. Temes and S. K. Mitra, *Modern Filter Theory and Design*. Wiley & Sons, 1973.
- [24] D. S. Humpherys, *The Analysis, Design, and Synthesis of Electrical Filters*, 2nd ed. Prentice-Hall, Inc., Englewood Cliffs, N.J., 1970.
- [25] L. Lind, "Accurate cascade synthesis," *IEEE Transactions on Circuits and Systems*, vol. 25, no. 12, pp. 1012–1014, December 1978.
- [26] D. I. L. De Villiers, "Analysis and design of conical transmission line power combiners," Ph.D. dissertation, University of Stellenbosch, 2007.
- [27] J. R. Whinnery, H. W. Jamieson, and T. E. Robbins, "Coaxial-line discontinuities," *Proceedings of the IRE*, vol. 32, no. 11, pp. 695–709, Nov 1944.

- [28] D. I. L. De Villiers, "Higher order modal interactions in conical power combiners," in *2012 International Conference on Electromagnetics in Advanced Applications*, 2012, pp. 345–348.
- [29] P. Rizzi, *Microwave Engineering - Passive Circuits*. Prentice-Hall, Inc., Englewood Cliffs, N.J., 1988.
- [30] R. M. Fano, "Theoretical limitations on the broadband matching of arbitrary impedances," *Journal of the Franklin Institute*, vol. 249, no. February 1950, pp. 57–83, 1950.
- [31] P. I. Somlo, "The computation of coaxial line step capacitances," *IEEE Transactions on Microwave Theory and Techniques*, vol. 15, no. 1, pp. 48–53, 1967.
- [32] N. Marcuvitz, *Waveguide Handbook*. Dover, 1986.
- [33] P. Guillon, "Dielectric resonators," in *Proceedings of the 42nd Annual Frequency Control Symposium, 1988.*, 1988, pp. 259–262.
- [34] M. Pospiezalski, "Cylindrical dielectric resonators and their applications in TEM line microwave circuits," *IEEE Transactions on Microwave Theory and Techniques*, vol. 3, no. MTT-27, 1979.
- [35] R. Levy, "Synthesis of mixed lumped and distributed impedance-transforming filters," *IEEE Transactions on Microwave Theory and Techniques*, vol. 20, no. 3, pp. 223–233, 1972.
- [36] D. I. L. de Villiers, P. W. van der Walt, and P. Meyer, "Design of a ten-way conical transmission line power combiner," *IEEE Transactions on Microwave Theory and Techniques*, vol. 55, no. 2, pp. 302–308, 2007.
- [37] D. I. De Villiers, P. W. van der Walt, and P. Meyer, "Design of conical transmission line power combiners using tapered line matching sections," *IEEE Transactions on Microwave Theory and Techniques*, vol. 56, no. 6, pp. 1478–1484, 2008.
- [38] R. D. Beyers and D. I. De Villiers, "Compact conical-line power combiner design using circuit models," *IEEE Transactions on Microwave Theory and Techniques*, vol. 62, no. 11, pp. 2650–2658, 2014.
- [39] P. W. van der Walt, "Novel matched conical line to coaxial line transition," *Proceedings of the South African Symposium on Communications and Signal Processing, COMSIG*, pp. 431–434, 1998.
- [40] R. D. Beyers and D. I. L. de Villiers, "A general conical to coaxial line transition," in *2016 IEEE MTT-S International Microwave Symposium (IMS)*, 2016, pp. 1–4.
- [41] —, "A general impedance tapered transition for  $N$ -way conical and coaxial combiners," *IEEE Transactions on Microwave Theory and Techniques*, vol. 64, no. 12, pp. 4482–4490, 2016.
- [42] —, "Design and analysis of an impedance tapered conical to coaxial transmission line transition," in *2014 44th European Microwave Conference*, 2014, pp. 307–310.

- [43] S. Koziel, Q. S. Cheng, and J. W. Bandler, "Space mapping," *IEEE Microwave Magazine*, vol. 9, no. 6, pp. 105–122, 2008.
- [44] S. Koziel, J. W. Bandler, and K. Madsen, "A space-mapping framework for engineering optimization - Theory and implementation," *IEEE Transactions on Microwave Theory and Techniques*, vol. 54, no. 10, pp. 3721–3730, 2006.
- [45] J. W. Bandler, R. M. Biemacki, S. Member, S. H. Chen, S. Member, R. H. Hemmers, S. Member, and K. Madsen, "Electromagnetic optimization exploiting aggressive space mapping," *IEEE Transactions on Microwave Theory and Techniques*, vol. 43, no. 12, pp. 2874–2882, 1995.
- [46] D. W. Wolsky, "Automated space-mapping framework for electromagnetic device optimisation," Master's thesis, University of Stellenbosch, 2019.
- [47] T. Electronics, "RF coax connectors SMA connectors and beyond available in various base metal options , including stainless steel , brass and zinc diecast White Bronze plating Meets all performance," pp. 52–55.
- [48] D. C. Montgomery and G. C. Runger, *Applied Statistics and Probalisty for Engineers*, 6th ed., 2014.
- [49] Protocase. (2019) CNC machining tolerances. [Online]. Available: <https://www.protocase.com/resources/tolerances/cnc-machining.php>
- [50] Trax. (2018) Capabilities. [Online]. Available: <https://www.trax.co.za/capabilities>